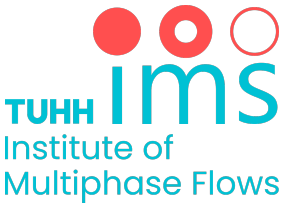

Master Thesis

Flow Characteristics of Differently Sized Lagrangian Sensor Particles in a 15,000 L Bioreactor

by Isabel Sophie Brouwers

1st Examiner: Prof. Dr.-Ing. Michael Schlüter

2nd Examiner: Prof. Dr.-Ing. Dr. h. c. Uwe Hampel

Supervisor IMS: Sebastian Hofmann, M.Sc.

Supervisor HZDR: Lukas Buntkiel, Dipl.-Ing.

01.08.2023 - 31.01.2024

Eidesstattliche Erklärung

Hiermit versichere ich, dass ich die vorliegende Arbeit selbstständig verfasst und keine anderen als die angegebenen Quellen und Hilfsmittel benutzt habe, dass alle Ausführungen, die anderen Schriften wörtlich oder sinngemäß entnommen wurden, kenntlich gemacht sind und dass die Arbeit in gleicher oder ähnlicher Fassung noch nicht Bestandteil einer Studien- oder Prüfungsleistung war.

Hamburg, den _____ Unterschrift: _____

Contents

Abbreviations, Symbols and Units

Table 1: List of applied and relevant dimensionless numbers

Symbol	Meaning
c_{D}	Drag coefficient
Ne	Newton number
P	Power input
Re_{p}	Particle Reynolds number
Re_{STR}	Reynolds number stirred tank reactor
St	Stokes number

Table 2: Latin symbols and respective units

Symbol	Meaning	Unit
d_*	Dimensionless particle diameter	-
d_1	Reactor diameter	m
d_2	Impeller diameter	m
d_{p}	Particle diameter	m
$\vec{F}_{\mathrm{A}}$	Static buoyancy force	kg m s^{-2}
$\vec{F}_{\mathrm{D}}$	Dynamic buoyancy force	kg m s^{-2}
$\vec{F}_{\mathrm{G}}$	Gravity force	kg m s^{-2}
$\vec{F}_{\mathrm{T}}$	Inertia force	kg m s^{-2}
$\vec{F}_{\mathrm{W}}$	Friction and drag force	kg m s^{-2}
$\vec{F}_{\mathrm{Z}}$	Centrifugal force	kg m s^{-2}

Symbol	**Meaning**	**Unit**
g	Gravity acceleration	m s^{-2}
h_{norm}	Normalized reactor height	-
$h(t)$	Height in fluid	m
H	Fluid level	m
n	Stirrer frequency	s^{-1}
M	Torque	kg m^2 s^{-2}
P	Power	kg m^2 s^{-3}
p_0	Atmospheric pressure	kg m^{-1} s^{-2}
p	Pressure	kg m^{-1} s^{-2}
p_{z}	Hydrostatic pressure	kg m^{-1} s^{-2}
p_{max}	Maximum pressure	kg m^{-1} s^{-2}
p_{min}	Minimum pressure	kg m^{-1} s^{-2}
p_{s}	Back pressure	kg m^{-1} s^{-2}
R_{bottom}	Reactor bottom	m
R_{top}	Reactor bottom	m
V	Volume	m^3
v_*	Dimensionless sinking velocity	-
v_{ax}	Axial velocity	m s^{-1}
$v_{\mathrm{ax,pos}}$	Axial positive velocity	m s^{-1}
$v_{\mathrm{ax,neg}}$	Axial negative velocity	m s^{-1}
$\bar{v}_{\mathrm{ax}}$	Average axial velocity	m s^{-1}
v_{f}	Fluid velocity	m s^{-1}
v_{p}	Particle velocity	m s^{-1}
v_{rel}	Slip velocity	m s^{-1}
v_{s}	Sinking velocity	m s^{-1}
t	Time	s
t_0	Start time	s
t_{c}	Circulation time	s
t_{e}	End time	s
$t_{\mathrm{mix,global,95}}$	Global mixing time	s
t_{res}	Residence time	s
$\bar{t}_{\mathrm{c}}$	Average circulation time	s
z	Axial immersed position	m

Table 3: Greek symbols and respective units

Symbol	Meaning	Unit
Λ	Macro-scale length	m
λ	Kolmogorov length	m
ϵ	Dissipated energy	$m^2\ s^{-3}$
η_f	Dynamic Viscosity of the Fluid	$kg\ m^{-1}\ s^{-1}$
ν	Kinematic viscosity	$m^2\ s^{-1}$
τ_f	Characteristic time of flow	s
τ_p	Characteristic time of particle	s
ρ_f	Fluid density	$kg\ m^{-3}$
ρ_p	Particle density	$kg\ m^{-3}$

Table 4: List of relevant abbreviations

Abbreviation	Definition
bPod	Bio-process online analytical device
CHO	Chinese Hamster Ovary
DO	Dissolved oxygen
EE	Elephant Ear
EPDM	Ethylene-propylene-diene-monomer
FDA	U.S. Food and Drug Administration
IMU	Internal measurement unit
LP	Lagrangian Particle
LSP	Lagrangian Sensor Particle
LSP_{40}	40 mm Lagrangian Sensor Particle
LSP_{60}	60 mm Lagrangian Sensor Particle
MC	Micro controller
NAND	Not-And
PB	Pitched blade
RT	Rushton Turbine
STR	Stirred tank reactor
XML	EXtensible Markup Language

Abstract

In the industry, process parameters are monitored using fixed sensors mounted at the reactor wall. However, this Eulerian approach provides barely detailed insights and information about the mixing performance, which is crucial for productivity in bioprocesses. In contrast, the Lagrangian approach focuses on Lagrangian Sensor Particles (LSPs) in the moving fluid exhibiting an appropriate flow-following behavior mimicking a cell. As demonstrated in previous studies, they can be equipped with multiple process parameter sensors such as temperature, pH, dissolved oxygen or pressure.

This thesis addresses three key aspects: the hydrodynamic characterization of a single-phase 15,000 L bioreactor with a pitched blade impeller and Rushton Turbine setup by means of LSPs, the comparison of two LSP sizes regarding their flow-following behavior, and the determination of differently mixed regimes within the reactor, known as compartments.

LSPs with two different diameters, 40 mm (LSP_{40}) and 60 mm (LSP_{60}), equipped with a pressure sensor, are investigated in this study. The experiments are carried out at five different impeller frequencies. Based on measured pressure data, the axial probability of presence over the reactor height, axial velocities, circulation times, and selected circulation time distributions are analyzed to further ascertain axial compartments and, consequently, conduct a Lagrangian regime analysis. Additionally, the overall circulation times of both LSPs are compared to global mixing times in the same setup.

The estimated Stokes number for the LSP_{40} and LSP_{60} are 0.21 and 0.32 for the meso-scale and 0.002 and 0.004 for the macro-scale, respectively. Hence, for the macro-scale a flow-following behavior is assumed, as it results in $St \ll 1$. The hypothesis of the LSP_{60}

having a bigger inertia than the LSP_{40} is experimentally shown in the probability of presence and the Lagrangian velocity analysis. Furthermore, the overall circulation times of LSP_{60} are up to 1.4 times lower than those of LSP_{40}. As LSP_{60} exhibit velocities in the same range as the LSP_{40}, this indicates that LSP_{60} follow shorter circulation loops.

Circulation time results reveal three compartments within the reactor, which boundaries are assumed above the pitched blade impeller and below the Rushton Turbine. According to these results, the Lagrangian regime analysis shows that the middle compartment exhibits a broad residence times distribution. In contrast, the top and bottom compartment show less probability for higher residence times.

At least three circulation loops within the reactor are estimated, as seen in the CTD displaying a trimodal distribution for the horizontal plane below the PB. Similarly to literature statements and confirming the latter, the ratio of the examined global mixing time to overall circulation time is between 3 and 4.

This thesis emphasizes the potential and broad applicability of LSPs to gain insights into mixing processes solely through pressure data. This research underscores that the used LSP_{40} are more likely to discover a flow-following behavior on the meso-scale, especially for higher impeller frequencies.

Zusammenfassung

In der Industrie werden Prozessparameter mithilfe fixierter Sensoren überwacht, welche in der Reaktorwand angebracht sind. Diese Eulersche Betrachtung liefert kaum detaillierte Einblicke und Informationen über die Mischleistung, welche maßgebend für die Produktivität in Bioprozessen ist. Hingegen fokussiert sich der Lagrange Ansatz auf Lagrange-Sensorpartikel (LSPs) im bewegten Fluid, welche ein geeignetes strömungsfolgendes Verhalten aufweisen und eine Zelle nachahmen. In vorherigen Studien wurde gezeigt, dass sie mit verschiedenen Prozessparametersensoren, welche Temperatur, pH-Wert, gelöstem Sauerstoff oder Druck aufnehmen, ausgestattet werden können.

Diese Arbeit behandelt drei zentrale Aspekte: Die hydrodynamische Charakterisierung eines einphasigen 15.000 L Bioreaktors mit einem Schrägblattrührer und einer Rushton-Turbine mithilfe von LSPs, den Vergleich von zwei LSP-Größen hinsichtlich ihres strömungsfolgenden Verhaltens und die Bestimmung verschiedener Mischregime innerhalb des Reaktors, bekannt als Kompartimente.

In dieser Arbeit werden LSPs, welche mit einem Drucksensor ausgestattet sind, mit den zwei Durchmessern 40 mm (LSP_{40}) und 60 mm (LSP_{60}) untersucht. Die Versuche werden bei fünf verschiedenen Rührgeschwindigkeiten druchgeführt. Anhand der Druckdaten lassen sich die Aufenhaltswahrscheinlichkeiten der LSPs über die Reaktorhöhe, axiale Geschwindigkeiten, Zirkulationszeiten und Zirkulationszeitverteilungen für ausgewählte Höhen analysieren. Basierend auf den Ergebnissen, werden die Kompartimente bestimmt, um folglich eine Lagrange Regime Analyse durchzuführen. Darüber hinaus werden die Gesamtzirkulationszeit beider LSPs mit den globalen Mischzeiten im gleichen Reaktoraufbau verglichen.

Die geschätzten Stokes-Zahlen für LSP_{40} und LSP_{60} betragen 0,21 und 0,32 für die Mesoskala und 0,002 und 0,004 für die Makroskala. Auf der Makroskala wird ein strömungsfolgendes Verhalten angenommen, da die $St \ll 1$ beträgt. Die Hypothese, dass die LSP_{60} eine größere Trägheit als die LSP_{40} aufweisen, wird experimentell durch die Aufenthaltswahrscheinlichkeit und die Lagrange-Geschwindigkeitsanalyse gezeigt. Darüber hinaus sind die Gesamtzirkulationszeiten der LSP_{60} bis zu 1,4-mal niedriger als die der LSP_{40}. Da die Geschwindigkeiten der LSP_{60} im gleichen Bereich wie die LSP_{40} liegen, deutet dies darauf hin, dass die LSP_{60} kürzere Zirkulationschleifen durchlaufen.

Die Ergebnisse der Zirkulationszeiten weisen drei Kompartimente innerhalb des Reaktors auf, mit der Unterteilung oberhalb des Schrägblattrührers und unterhalb der Rushton-Turbine. Die Lagrange-Regimeanalyse zeigt, dass das mittlere Kompartiment eine breite Verteilung der Verweilzeiten aufweist. Im Gegensatz dazu zeigen das obere und untere Kompartiment eine geringere Wahrscheinlichkeit für längere Verweilzeiten.

Mindestens drei Zirkulationsschleifen innerhalb des Reaktors werden angenommen, welche aus der CTD mit einer trimodalen Verteilung für die horizontale Ebene unterhalb des Schrägblattrühers resultieren. Ähnlich zu Literaturangaben liegt das Verhältnis der untersuchten globalen Mischzeit zur Gesamtumlaufzeit zwischen drei und vier.

Diese Arbeit unterstreicht das Potential und die umfassende Anwendbarkeit von LSPs, welche ermöglichen, ausschließlich anhand der Druckdaten einen Einblick in die Mischprozesse zu erhalten. Die verwendeten LSP_{40} neigen auf der mesoskaligen Ebene, insbesondere bei höheren Rührfrequenzen, zu einem strömungsfolgenden Verhalten.

1 Motivation

Biotechnology is characterized as a multidisciplinary field that plays a mayor role in the pharmaceutical, food and biofuel industries [Cur11]. In recent years, the knowledge about bio process has increased, and biotechnological processes have expanded [Mit23], dominating nearly 20 % of the global pharmaceutical industry [MY11]. In bioprocesses, living cells are utilized to produce a desired product by transforming substrates. It is considered a promising future technology, due to mild reaction conditions and the specific and efficient gen expressions. The source organism reacts to its environment, which, due to minor changes, leads to an increased or decreased productivity of the organism [Cos11]. For living organisms, yeast, fungal, or mammalian cell cultures are often considered. A common cell line of mammalian cells is the Chinese Hamster Ovary cell (CHO). CHO cells represent an ideal system for the expression of human autoantigens due to their posttranslational processing capacities and protein folding [Leu08]. In the past 25 years, the volumetric yields of recombinant cell lines have increased about 20-fold [dJ11]. CHO cells represent the manufacturing host system for over 70 % of pharmaceutical proteins [Kar07]. An issue observed with CHO cells contributes to the requirement of a stable cell line, which in production is expensive, and, furthermore, occasionally low expression levels are detected [Leu08].

Living cells are sensitive towards changes in the environment, and complex interactions between the living cell and the media are challenging to estimate [Mit23]. The product yield strongly depends on the process parameter such as the pH-value, temperature, dissolved oxygen, and pressure. Especially when scaling up, a yield gap between the laboratory-scale reactors and industry-scale reactors is observed, which is caused by heterogeneities within the reactor [Weh19]. The

largest industry reactor for producing CHO cells consists of a working volume of 20,000 L [dJ11]. For process control, sensors are implemented into the system to measure important process parameters. The commonly used sensor is installed at a fixed position within the reactor wall. Nevertheless, the measured data are only valid for this localization and cannot be considered as an overall condition in the reactor [Lid02]. The gradients formed within the reactor, caused by heterogeneities, may influence the produced yield of the living cells, leading to reduced economic efficiency [San16]. In stirred tank reactors (STR), agitators are used to achieve efficient mixing for homogenization purposes. For industrial-scale bioreactors, a combination of a Rushton turbine and a pitched blade impeller is recommended [Nie98]. The Rushton turbine is characterized by its efficient gas dispersion, as bubble break-up occurs. For this purpose, the Rushton turbine is considered a lower localized impeller. The pitched blade impeller is suggested as an upper impeller, which can be characterized by higher pumping capacities [Nie98]. When using an agitator in bioprocesses, caution needs to be paid towards the shear stress leading to cell damage, caused by the impeller itself, the fluid dynamics, and interactions with the bubbles [Nie98].

To achieve an increased yield in a bioprocess, the interactions between substrates, cells, and important process parameters are crucial. Therefore, understanding the mixing behavior within the reactor and detecting heterogeneities, especially in a large-scale bioreactor, is essential. As fixed sensors are not considered representative measurements for the entire reactor, a sensor integrated within the moving fluid demonstrates greater potential. These so-called sensor particles are equipped with a sensor and range in size from 7.9 mm to 90 mm. The Lagrange Sensor Particles (LSP) manufactured and tested by the Technical University of Hamburg-Harburg (TUHH) are implemented in 40 mm sizes and consist of a pressure sensor. The LSP demonstrated representative macro-mixing information and applicability.

For laboratory-scaled reactors, various publications on sensor particles can be found [Bis21, Rei14, Rau23]. On an industrial scale, pub-

lications on integrated sensor particles are hardly available [Hof24], and none are found for a single-phase bioreactor equipped with a Rushton turbine and a pitched blade impeller.

This underlines the urge to investigate mixing performances and compartments within a reactor on industrial scale with an impeller setup of a Rushton turbine and a pitched blade impeller. The reactor in this thesis consists of a volume of 15,000 L. For this purpose, these aspects will be investigated by using LSPs with a 40 mm and 60 mm diameter. The 60 mm LSP will be designed and compared with the 40 mm LSP. The LSPs will be examined, regarding their flow-following capabilities. By analyzing the pressure data, the mixing characterization of the bioreactor and compartments detection are investigated. Since large data sets will be available from the pressure sensor, a Python™ script is established for preprocessing the data and for further calculations. The thesis is conducted in cooperation with the TUHH and the Helmholtz Zentrum Dresden Rossendorf (HZDR).

2 Theoretical Fundamentals

This chapter provides the theoretical background for subsequent chapters in this thesis. Initially, the reactor is outlined, including its components and dimensionless numbers. Additionally, the Eulerian and Lagrangian approaches are explained, followed by a discussion of particle motion. Finally, examples and calculations for Lagrangian Sensor Particles (LSPs) are presented.

2.1 Biotechnological Processes

Bioreactors are considered as the most significant part in industrial biotechnical processes [Lid02]. Their primary function is to convert substrates into the desired end product while achieving high yields [Lid02]. As the bioreactor represents the final step in the upstream process, following purification restricts any further yield increments [Lid02].

The design and setup of the reactor can vary for different processes, ranging from laboratory scale to industrial scale, with a filling capacity of up to 20,000 L [Gre08b]. Common designs are the stirred tank reactor (STR), the bubble column reactor, the airlift reactor, the loop reactor, and the packed bed reactor. The stirred tank reactor is considered to be the dominant design due to its versatility, operability and its manufacturability [Man16].

Product titer and yield depend heavily on the process conditions and a homogeneity within the reactor, since finely distributed cells within the medium can only achieve high productivity when optimal culture conditions are provided [Lid02]. Therefore, maintaining ideal conditions and homogeneity is crucial. Besides the substrates,

key operating parameters include pH value, temperature, and aeration [Lid02]. The supply of oxygen is required for converting the substrates and for cell growth [Nie04]. Nevertheless, the focus is solely on a single-phase reactor without aeration. Thus, the impact of aeration is not considered.

To achieve high homogeneity, the vessels are equipped with stirrers [Gre11]. Additional baffles are installed to avoid vortexing. In bioprocesses, it is important to ensure that shear forces generated by the agitator do not damage the microorganisms. The advantage of using a stirrer, with the disadvantage of the potentially resulting damage to microorganisms, highlights the challenge in achieving optimal homogeneity.

Insufficient mixing can lead to gradients forming within a reactor [Lid02], which are also referred to as compartments. In general, compartments are characterized as regions within the reactor exhibiting distinct mixing behavior, as seen in Figure 2.1. The compartments model characterizes the macromixing area in the form of convection [Guh06]. According to previous publications and studies [Har17, Hof24, Ros18], the distribution of these compartments depends on the reactor and stirrer setup. In the publication of Hofmann et al. [Hof24], compartments within a 15,000 L reactor equipped with three Elephant Ear impellers (EE) were investigated. The results showed a total of three compartments, which were located below the bottom impeller, between the bottom and top impeller, and above the top impeller. The compartments exhibited different mixing behavior, observed through parameters such as mixing time, probability over height, and velocities within the reactor [Hof24]. Compartmentalization is detected during the scale-up from the laboratory to industrial scale, as a yield gap is observed [Weh19]. During a bioprocess, substrates for cell cultivation and fluids for pH adjustments are added [War85], and in regions with poor mixing behavior, concentration gradients are formed, affecting the overall process performance [Har17].

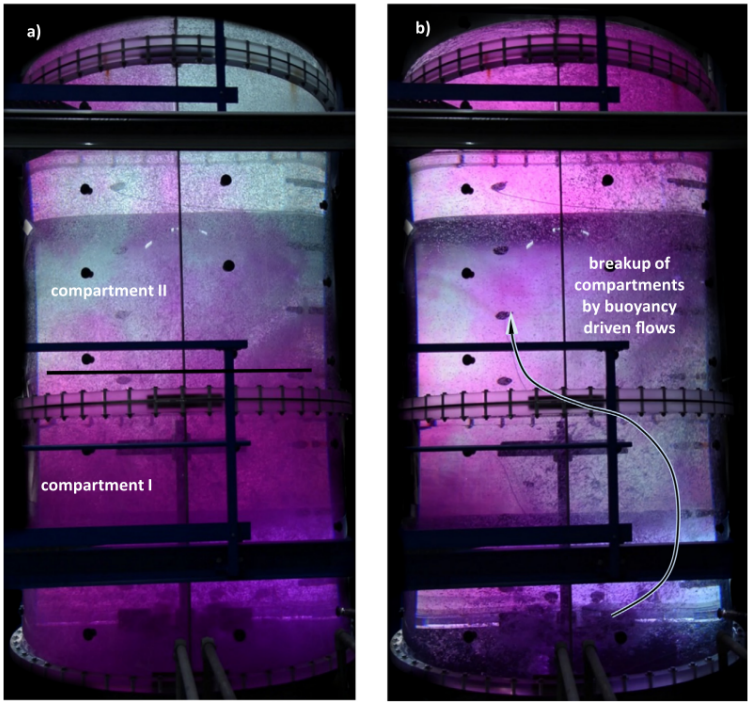

Figure 2.1: Decolouration processes in a 15,000 L acrylic reactor, showing in (a) the visible compartments and in (b) the break-up of the compartments.[Ros18]

Compartments exhibit a varying extracellular environment for the cells, which may trigger regulatory genes within the microorganism, inhibiting important other genes or unintentionally expressing unwanted genes, subsequently reducing productivity and potentially increasing byproduct yield [Lid02]. For instance, the microorganism *Saccharomyces cerevisiae* produces ethanol under anaerobic conditions but adenosine triphosphate under aerobic conditions. Controlling the parameters in a reactor involves the utilization of sensors,

commonly achieved through fixed sensors positioned at the reactor wall. However, data collected from these fixed sensors offers a limited picture of the entire reactor [Lid02].

In bioreactors different microorganisms can be used to produce a desired product. Currently, 60 to 70 % of today's biopharmaceuticals are produced within mammalian cells [Lim10]. The mammalian cell line of the Chinese Hamster Ovary (CHO) cells produces therapeutic proteins and can be characterized by its insensitivity to cell damage [Oma10, Man16]. An essential advantage of CHO cells lies in their similarity to the human glycosylation-associated genes, which can be examined to understand the regulation and expression [Man16]. The CHO cells consist of a 2.5 Gigabase genomic sequence with 24400 genes located on 21 chromosomes, including genes responsible for the therapeutic protein [Man16].

While ideal reactor models apply mainly to laboratory scale, reactors of a larger scale encounter mixing gradients and compartmentalization [Kra18]. To achieve desired gene expression, optimal process conditions must be provided, making it crucial to fully understand the flow behavior within the bioreactor.

2.1.1 Stirrer Configurations and Flow Behavior

Stirrers are used to enhance the mixing in the reactor for an increased mass and heat transfer. They can be divided into stirrers with an axial or a radial flow distribution. In industrial processes, the most common setup is a combination of both stirrer types [Gre11].

In order to achieve an optimal distribution of cells and substrates within the reactor, different impeller setups can be used depending on the respective stirring task and the given system [Kra18]. A distinction is made between turbulent and laminar flows created during agitation. Turbulent mixing achieves a more extensive and effective mixing as eddies are formed. Nevertheless, turbulent mixing might not be suitable for all media.

This chapter primarily focuses on static impellers due to their high technical relevance [Kra18]. The selection of impellers is narrowed

down to those widely accepted in practice, where reliable and accessible design documents exist. When dealing with consumable products, such as pharmaceuticals or food, the U.S. Food and Drug Administration (FDA) is essential [FDA24]. The FDA protects public health and ensures a secure manufacturing process. The approval from the FDA is required for both production and product sale. Consequently, the equipment used in the production must adhere to FDA standards. This requirement influences the choice of materials, operational methods, and process parameters. As a result, introducing and adapting new technologies or approaches hold both technical and regulatory challenges [FDA24].

Axial impellers, notably the EE, the pitched blade (PB), and Hydrofoils, are commonly used for low viscous fluids $\eta_\mathrm{f} < 10^4$ mPa s [Kra04, Eur24]. They are suitable for homogenization and for suspending solids. Axial impellers are characterized by the down-pumping flow pattern, transporting the medium in a vertical direction within the reactor. The fluid, directed either downwards or upwards depending on the orientation of the impeller, initiates a circulation loop by moving from the center along the inner radius of the impeller, reaching the reactor bottom, and is subsequently redirected near the reactor wall, as seen in Figure 2.2 (left) [Kra18].

In contrast, radial impellers, mainly the turbine impellers, are characterized as a high-speed stirrer and suitable for low-viscosity liquids in the range of $\eta_\mathrm{f} < 10^4$ mPa s [Kra18]. These impellers move the fluid in radial direction, from the reactor center to the reactor wall, as shown in Figure 2.2 (right) [Kra18]. The fluid is redirected both upwards and downwards at the reactor wall, creating two circulation loops.

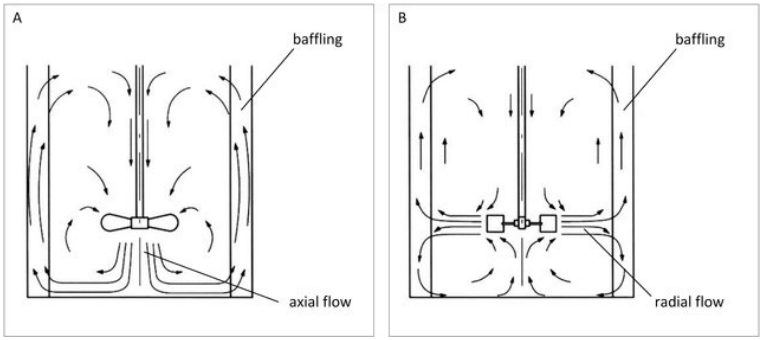

Figure 2.2: Flow patterns shown (A) for an axial stirrer (B) for a radial stirrer [Sch19].

A common combination identified in various studies is the radial Rushton Turbine (RT) impeller in conjunction with the axial PB impeller [Ros18, Fit19, Vrá00]. Consequently, both radial and axial flows are generated. The RT is recognized for its efficient gas dispersion and is positioned near the bottom of the reactor, close to the air outlets. The PB impeller is suggested as an upper impeller, characterized for its high pumping capacities [Nie98]. Both impeller consist of a high throughput and an improved power efficiency [Kra04, Nie97].

2.1.2 Dimensionless Numbers for Comparison

When comparing different reactors, dimensionless numbers are fundamental. Regarding the reactor design, important dimensionless numbers are the Reynolds number Re_{STR} and the Newton number Ne.

The Reynolds number Re_{STR} for an STR is used to determine if the flow is in a laminar or turbulent regime [Dor13]. It is defined as

$$Re_{\mathrm{STR}} = \frac{n \cdot d_2^2 \cdot \rho_{\mathrm{f}}}{\eta_{\mathrm{f}}}, \tag{2.1}$$

with the impeller diameter d_2, the impeller frequency n, the density of the fluid ρ_f and the kinematic viscosity of the medium η_f [Kai18, Wol10].

The dimensionless power input can be estimated by using the Newton number Ne [Kai18, Wol10], defined as

$$Ne = \frac{P}{n^3 \cdot d_2^5 \cdot \rho_\mathrm{f}}. \tag{2.2}$$

The power input P can be calculated by means of

$$P = 2 \cdot \pi \cdot n \cdot M. \tag{2.3}$$

In the equation, M describes the torque, which results from the difference between the torque in the empty vessel compared to the torque in the liquid filled vessel [Kai18].

Furthermore, in process engineering, the power to volume ratio [Kai18, Wol10] is commonly used and can be calculated by

$$\frac{P}{V} = \frac{Ne \cdot n^3 \cdot d_2^5 \cdot \rho_\mathrm{f}}{V}. \tag{2.4}$$

The dimensionless numbers offer the possibility to compare two reactor types with the same dimensionless numbers [Kai18].

In Figure 2.3 the Newton number Ne is plotted over the Reynolds number Re_STR, considering three different impeller types: the RT, the PB and the curved blade turbine. The impeller are located in a baffled tank with no aeration. Ne decreases with increasing Re_STR. In the laminar regime $Re_\mathrm{STR} < 10$, Ne decreases steadily for all impeller and low impeller frequency n. With increasing impeller frequency, the transient regime is reached. At $Re_\mathrm{STR} \gg 10^4$, the regime is considered as turbulent [Old14].

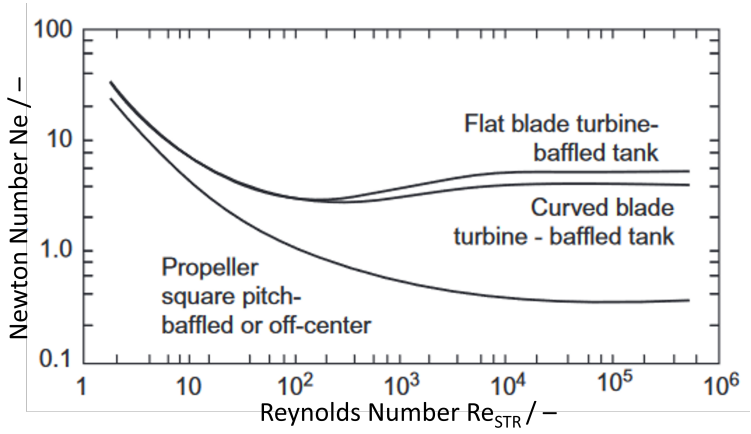

Figure 2.3: Power input for the RT, PB and a curved blade turbine. All impeller are considered in a baffled tank with no aeration. The Newton number Ne is plotted over the Reynolds number Re_{STR} [Old14].

2.1.3 Mixing on Different Scales

Energy is introduced into the system, when a stirrer or agitator is utilized. [Sre15]. The stirrer generates eddies in the fluid, which serve the purpose of mixing in the reactor [Sre15]. The sizes of the eddies depend on the power induced by the stirrer, the distance from the primary vortex's point of origin, and the time elapsed since a vortex was generated [Sre15]. Fluids in which eddies occur are referred to as turbulent flows due to the varying velocities within the eddies [Sre15]. Depending on the size of the eddies, turbulence can be classified as macro-, meso- or micro-turbulence.

Various methods exist for describing turbulence. An applicable approach is by Prandtl, who posited that fluctuations cause flow elements to transport impulses in the flow [Sre15]. Hence, an eddy in a fluid can be understood as the movement of fluid elements. As fluid elements move within a turbulent flow, they stimulate surrounding fluid elements, leading to the development of second-order turbulence [Sre15]. As turbulence progresses from one order to another, kinetic energy is continually divided into smaller eddies [Sre15]. This process continues, generating third-order turbulence and progressing until the smallest turbulent eddies are reached [Sre15]. The kinetic energy of the smallest eddy scale is released as thermal heat due to friction with no further induction of turbulence [Sre15]. The smallest eddy scale is known as the Kolmogorov length scale λ_{K} and is defined as

$$\lambda_K = \left(\frac{\nu^3}{\bar{\epsilon}} \right)^{\frac{1}{4}}, \tag{2.5}$$

where ν is the kinematic viscosity and ϵ describes the mean dissipated energy [Sre15]. $\bar{\epsilon}$ is estimated by

$$\bar{\epsilon} = \left(\frac{P}{V \cdot \rho_{\mathrm{f}}} \right), \tag{2.6}$$

with P and V describing the power to volume ratio [Nie21].

In the following, the mixing process within a reactor is examined more in detail with regard to the stirrer and formed eddy sizes, which is shown in Figure 2.4. The macro-scale is described by Λ. The primary eddy (first order turbulence) originates at the blade with an equal size of $\Lambda = d_2$ [Wol10]. The macro-scale eddies at the impeller tip posses the most energy and decrease cascading into smaller eddies (second-order turbulence), where the kinetic energy splits with each splitting of the eddies $\Lambda = d_2/10$ [Wol10]. On the macro-scale, a turbulent and chaotic flow is observed. The mixing on the scale of particles is considered as meso mixing [Mao17]. Eventually, the kinetic energy dissipates within micro-scale eddies (Kolmogorov scale) into thermal energy [Sre15, Wol10].

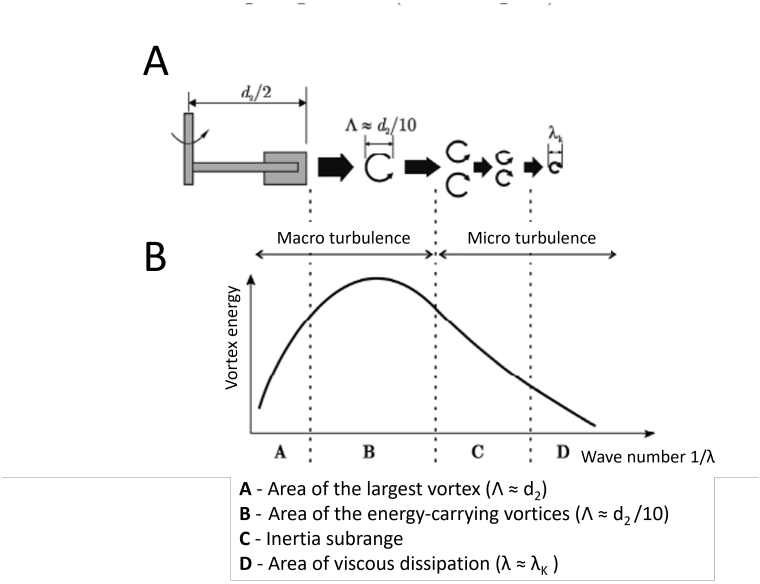

Figure 2.4: Macro and micro turbulences within a reactor in relation to the stirrer blade, with (a) from [Kra04, Wol10], and (b) from [Dec05]. Illustrated as seen in [Rei14].

Homogenization through mixing occurs at different levels. Macro mixing is achieved at the largest level, which corresponds to the size of the reactor, and is marked by convection [Fit21]. At the microscopic level, the smallest scale (Kolmogorov scale) is characterized by microscopic diffusion, which is defined as the level where reactions occur [Fit21]. The mixing time in a reactor is distinguished between the macro mixing and micro mixing, as two different scale levels are observed. Hence, the macro mixing on a macroscopic level may be reached, whereas the micro mixing is still not completed [Fit21]. Meso mixing falls between macro and micro mixing [Kra04]. The turbulence model is considered one of the last unresolved challenges

in classical physics and represents one of the most complex forms of fluid motion [Sre15].

The turbulence scales within a reactor provide a foundation for understanding the dynamics of fluid flow. Transitioning from the macro-scale turbulence characterized by convection to the microscopic Kolmogorov scale involving thermal energy dissipation, the complexity of a particle in a fluid motion becomes apparent.

2.2 Eulerian and Lagrangian Approach

In industry, sensors are used to control process conditions within the reactor. The common approach is to integrate the sensor at a fixed position within the reactor. This measurement is based on the Eulerian approach. The Eulerian approach describes a fixed finite volume of space through which a fluid passes, while process conditions and flow conditions are continuously measured [Aza21]. The information gathered describes the average behavior of the fluid [Sai14]. This is prone to errors, as heterogeneities within the reactor may not be detected. The knowledge within the reactor is limited solely to the measured point. As referred to before in Section 2.1, inhomogeneities within the reactor lead to a decreased productivity since the optimal surrounding for the microorganism cannot be provided.

An alternative is the Lagrangian approach. The Lagrangian approach focuses on an individual particle and is considered as the moving observer, simultaneously gathering information [Rak21]. From the perspective of the particle, it is still, while the surrounding fluid is colliding with the particle [Aza21]. The difference between Lagrangian and Eulerian approach is shown schematically in Figure 2.5.

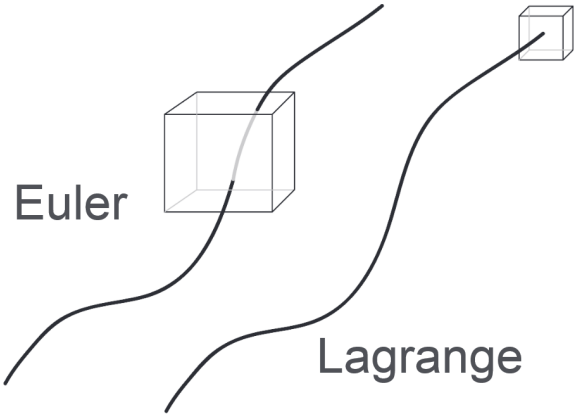

Figure 2.5: Euler as finite volume and fixed observer, compared to the Lagrangian moving volume and moving observer [Cor12].

When information about the location of the particle at different time steps is connected, it can be described as the trajectory of the particle. The Lagrangian approach is more complex; however, it offers a more comprehensive data set on the movement of the respective particles [Gou99]. The Lagrangian Sensor Particles (LSP) are an innovative new sensor type that can be integrated into the moving fluid and continuously collect process data. The measurement offers insights into the movement of an individual particle, whereas in the Eulerian approach, average behavior is displayed [Sai14]. Thus, the Lagrangian approach is essential when optimizing a process, as inhomogeneities can be detected within the reactor. Using an LSP demonstrates the advantage of following the convective mixing streams within the reactor. By tracking the LSP, the frequently visited areas within the reactor are detected, and, conversely, areas remaining unvisited are identified as well. These areas represent the compartments within the reactor. Thus, a better understanding

of the mixing behavior is achieved, which may lead to improved conditions for growing cells.

2.3 Particle Movement

In this chapter, the interaction between the fluid and a particle is discussed more in detail. Therefore, the acting forces are described and differentiated. When a particle is exposed to a moving fluid, flow regimes of the fluid and the flow-following behavior of the particle within the fluid plays a crucial role. Therefore, dimensionless numbers are presented for differentiating the flow regime and for estimating the flow-following behavior.

2.3.1 Forces on Rigid Bodies in a Fluid

A particle in a fluid is exposed to forces affecting the particle movement. These forces are described in this subsection for a particle with a solid sphere and a diameter d_P, which is immersed in a fluid.

The acting forces on the rigid body can be characterized into two groups: surface forces and mass forces. Surface forces include static buoyancy forces $\vec{F}_\mathrm{A}$ and dynamic buoyancy forces $\vec{F}_\mathrm{D}$, as well as friction and drag forces $\vec{F}_\mathrm{W}$. Mass and volume forces encompass gravity forces $\vec{F}_\mathrm{G}$, inertial forces $\vec{F}_\mathrm{T}$ and centrifugal forces $\vec{F}_\mathrm{Z}$. The sum of the before stated forces

$$\vec{F}_\mathrm{A} + \vec{F}_\mathrm{D} + \vec{F}_\mathrm{W} + \vec{F}_\mathrm{G} + \vec{F}_\mathrm{T} + \vec{F}_\mathrm{Z} = 0 \tag{2.7}$$

balance out to zero. The forces involved have a varying impact on the object depending on factors like surface properties, the sphericity, the mass of the rigid body and the properties of the fluid itself [Sti09]. Forces considerably weaker than others forces are neglected [Sti09]. Depending on the size of the particle, smaller particles tend to be more affected by the surface forces, such as the drag force, and larger and heavier particles are predominantly characterized by mass forces.

In further explanations, surface forces and mass forces will be taken into account, with focus on a rigid sphere in a fluid [Sti09].

Surface forces can be further characterized into pressure forces and drag forces. An acceleration field generates a pressure gradient in the fluid. By integrating the pressure over the surface, the static buoyancy $\vec{F}_{\mathrm{A}}$ is obtained, which refers to a body that is uniformly surrounded by a pressure profile that is evenly distributed. The static buoyancy $\vec{F}_{\mathrm{A}}$ acts in the opposite direction of the gravity force $\vec{F}_{\mathrm{G}}$ and it is calculated by formula

$$\vec{F}_{\mathrm{A}} = g \cdot \rho_{\mathrm{f}} \cdot \frac{\pi}{6} \cdot d_{\mathrm{p}}^3, \tag{2.8}$$

where ρ_f is the density of the fluid and g is the gravitational acceleration [Sti09, Kra04].

In case of an unevenly distributed pressure profile, the corresponding force is referred to as dynamic buoyancy $\vec{F}_{\mathrm{D}}$. The dynamic buoyancy force $\vec{F}_{\mathrm{D}}$ acts orthogonal to the direction of flow. This uneven flow around the body can result from variations in the flow profile, the shape of the body or the rotational movement of the body.

Another significant force in a moving fluid is the drag force $\vec{F}_{\mathrm{W}}$, which acts in the opposite direction as the incoming flow. The drag force $\vec{F}_{\mathrm{W}}$ comprises a combination of the pressure and friction forces [Sti09, Kra04]. A crucial parameter in the calculation of the drag force $\vec{F}_{\mathrm{W}}$ is the dimensionless drag coefficient c_D. The drag coefficient is influenced, among other factors, by the particle Reynolds number [Sti09, Kra04]. The drag force $\vec{F}_{\mathrm{W}}$ can be estimated by

$$\vec{F}_{\mathrm{W}} = c_{\mathrm{D}} \cdot \rho_{\mathrm{f}} \cdot \frac{\pi}{4} \cdot d_{\mathrm{p}}^2 \cdot \frac{v_{\mathrm{p}}^2}{2}, \tag{2.9}$$

and includes v_{p} as particle velocity [Sti09, Kra04].

Mass forces encompass gravity force $\vec{F}_{\mathrm{G}}$, inertial forces $\vec{F}_{\mathrm{T}}$, Coriolis forces and centrifugal forces [Sti09, Kra04]. Gravity operates in the direction of the earth's gravitational field and is calculated by

$$\vec{F}_{\mathrm{G}} = g \cdot \rho_{\mathrm{p}} \cdot \frac{\pi}{6} \cdot d_{\mathrm{p}}^3. \tag{2.10}$$

It results from the product of the earth's gravitational field and the particle's density ρ_f and volume of the particle [Sti09, Kra04].

Inertial force $\vec{F}_{\mathrm{T}}$ opposes acceleration and represents the force that, depending on the mass of the particle, leads to a reduced flow velocity compared to the actual velocity. Inertial forces, resulting from the motion of the reference system relative to the inertial system, are considered as "apparent" external forces [Spu19].

Only the buoyancy force and the gravity force act on a static rigid body in a non-moving fluid

$$\vec{F}_{\mathrm{G}} = \vec{F}_{\mathrm{A}}. \tag{2.11}$$

If both forces are equal, the particle is considered to be neutrally buoyant. This principle corresponds to the Archimedes principle [Oer15].

In contrast to a particle in a resting fluid, a particle in motion experiences an increased influence by the surrounding fluid. When a particle is set in motion, it encounters friction and acceleration. The flow behavior of the particle is highly dependent on the flow regime. To distinguish between laminar or turbulent, the particle Reynolds number can be employed.

2.3.2 Particle Reynolds Number

The particle Reynolds number Re_{p} is a dimensionless number, that describes the ratio of the inertia of a particle to the viscosity forces. The particle Reynolds number Re_{p} is calculated by

$$Re_P = \frac{d_{\mathrm{p}} \cdot v_{\mathrm{rel}} \cdot \rho_{\mathrm{f}}}{\eta_{\mathrm{f}}} \tag{2.12}$$

and includes the particle diameter d_{p}, the dynamic viscosity of the fluid η_{f}, the density of the fluid ρ_{f} and the relative velocity of the particle v_{rel}, which is also referred to as slip velocity [Sub23]. The slip velocity is defined as the difference between the particle velocity v_{p} and fluid velocity v_{f} [Sub23]. Moreover, the particle Reynolds number Re_{p} serves as an indicator of the flow regime,

such as laminar or turbulent flow. The particle behavior is strongly influenced by the surrounding flow regime, which can be estimated with the drag coefficient c_{D} .

The drag coefficient c_{D} describes the resistance of a particle, and depends on the particle shape and sphericity, the surface roughness and flow regime [Yan99]. The equation

$$c_{\mathrm{D}} = \frac{24}{Re_{\mathrm{P}}} \cdot (1 + 0.173 \cdot Re_{\mathrm{P}}^{0.657}) + \frac{0.413}{1 + 16300 \cdot Re_{\mathrm{P}}^{-1.09}} \qquad (2.13)$$

is applicable for a spherical particle with a $Re_{\mathrm{p}} < 2.6 \cdot 10^5$. For non-spherical particles or other flow regimes, alternative drag coefficient c_{D} calculations are considered [Hai89]. Since the slip velocity in the fluid is hardly determinable, often assumptions are made for further calculations.

The dependency of $\mathrm{Re_p}$ and $\mathrm{c_D}$ is shown in the Figure 2.6 [Gre08a]. The diagram clearly indicates that the drag coefficient varies depending on the flow regime and the particle shape.

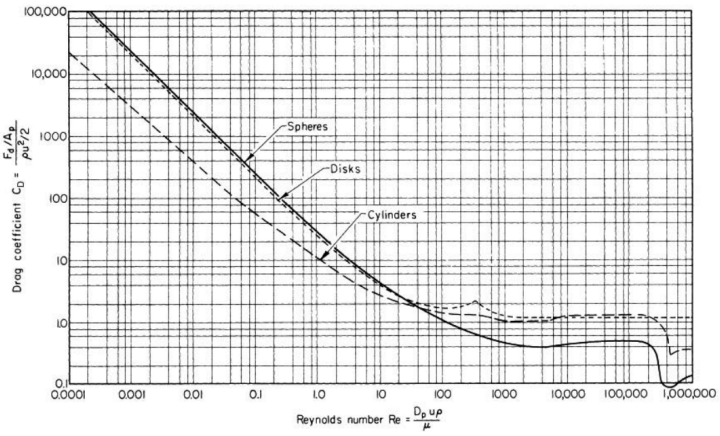

Figure 2.6: Drag coefficients c_D for a sphere, a cylinder and a circular disc in transverse flow, as a function of the Re_p in different flow regimes [Gre08a].

Particles in a turbulent regime are exposed to changing velocities. Furthermore, eddies forming within the fluid can be observed. Depending on the mixing scale, a particle exhibits a different flow-following behavior. To estimate the particle flow-following behavior in a fluid, the Stokes number St is calculated for different mixing scales.

2.3.3 Stokes Number

The Stokes number St is used to evaluate the flow-following behavior of particles. It describes the required time of a particle, to react to changes in flow velocity and flow direction in ratio to the characteristic time until velocity changes occur [Cro98]. The Stokes number can be described with

$$St = \frac{\tau_\mathrm{p}}{\tau_\mathrm{f}} = \frac{\text{char. time of particle}}{\text{char. time of flow}}, \tag{2.14}$$

including both characteristic times [Cro98].

Calculating the Stokes number is especially useful when investigating the flow-following behavior of specific particles with their respective properties. The Stokes number can be differentiated between the cases: $St \ll 1$, $\mathrm{St} \approx 1$, and $\mathrm{St} > 1$. For $\mathrm{St} \ll 1$, an enhanced flow-following behavior is observed, as particles exhibit a wider distribution within the observed system [Lin22]. Moreover, the response time of the particle to adapt to changes within the flow predominates the characteristic length of the system [Rad16]. With a Stokes number of $\mathrm{St} > 1$, the inertia of the particle increases, resulting in an increased response time of the particle to react to a change in velocity [Rad16, Sha03]. To achieve a flow-following behavior in a micro-scale turbulence, it is recommended to aim for a Stokes number of $\mathrm{St} \ll 1$, as particles then show the tendency to drift towards areas with low vorticity [Sha03]. Subsequently, particles with small Stokes numbers follow the fluid, while those with larger Stokes numbers are less likely to exhibit flow-following characteristics in micro-scale eddies [Sha03].

The Stokes number St calculation consists of two parts, with one part being the response time of the particle τ_p and the other part representing characteristic length scale to changes of the fluid velocity τ_f.

The response time of the particle τ_p is calculated by

$$\tau_p = \frac{4 \cdot \rho_\mathrm{p} \cdot d_\mathrm{p}^2}{3 \cdot \eta_\mathrm{f} \cdot Re_\mathrm{p} \cdot c_\mathrm{D}}. \tag{2.15}$$

The drag coefficient c_D and $\mathrm{Re_p}$ are calculated in Equation 2.12 and 2.13 [Rei14].

The characteristic time of change of the fluid velocity τ_f is described by

$$\tau_f = \frac{L}{v_\mathrm{f}}, \tag{2.16}$$

with L describing the characteristic fluid flow length scale and v_f, describing the characteristic fluid velocity.

The Stokes number is calculated for different turbulence scales. In this thesis, the approach by Reinecke [Rei14] estimating the Stokes number for the meso-scale and macro-scale, and the approach by Hofmann et al. [Hof24] applicable for the micro-scale are presented.

The relative velocity v_{rel} in the particle Reynolds number Re_p is calculated by the difference between the fluid velocity v_{f} and the particle velocity v_{p}. For all scales, the fluid velocity v_{f} is represented by the tip velocity v_{tip} and is calculated by

$$v_{tip} = n \cdot d_2 \cdot \pi, \tag{2.17}$$

where n describes the stirrer frequency, and $d_2 \cdot \pi$ describes the circumference [Rei14].

The particle velocity v_{p} is estimated by the maximal average axial velocity $\bar{v}_{\mathrm{ax,max}}$, which is obtained from experimental results. Hence, the relative velocity is calculated by

$$v_{\mathrm{rel}} = v_{\mathrm{tip}} - \bar{v}_{\mathrm{ax,max}}. \tag{2.18}$$

In the micro-scale approach of Hofmann et al. [Hof24], the characteristic length L is described by the Taylor scale L_{E}, which is defined as

$$L_{\mathrm{E}} = u_0 \sqrt{\frac{15\nu}{\bar{\epsilon}}}, \tag{2.19}$$

with u_0 being defined as the root-mean-square of the fluid velocity [Hui21]. Both, v_{f} and u_0 in τ_{f} are represented by the tip velocity v_{tip}. The energy dissipation $\bar{\epsilon}$ is calculated by the previous presented Equation 2.6. This results in the micro-scale Stokes number St, which is calculated by

$$St = \frac{\tau_{\mathrm{p}}}{\tau_{\mathrm{f}}} = \frac{4 \cdot \rho_{\mathrm{p}} \cdot d_{\mathrm{p}}}{3 \cdot \rho_{\mathrm{f}} \cdot (u_{\mathrm{tip}} - \bar{v}_{\mathrm{ax,max}}) \cdot c_{\mathrm{D}}} \sqrt{\frac{15\nu}{\bar{\epsilon}}}. \tag{2.20}$$

For the meso-scale Stokes number St calculation, an adjustment is made, as the relative velocity v_{rel} for the particle Reynolds number Re_p in the approach of Reinecke et al. [Rei14] is initially calculated by the sinking velocity v_s, resulting from a calculation of a

dimensionless diameter d_* and a dimensionless sinking velocity v_*. Since in this thesis a moving fluid is observed, the sinking velocity is replaced by Equation 2.18.

For the meso-scale, the characteristic length L is described by the impeller diameter d_2, and the characteristic velocity of the fluid $\mathrm{v_f}$ corresponds to the impeller tip speed $\mathrm{v_{tip}}$.

By using both equation 2.16 and 2.15 of the characteristic times of the fluid and particle, the Stokes number St for the approach of Reinecke et al. results in

$$St = \frac{\tau_\mathrm{p}}{\tau_\mathrm{f}} = \frac{4 \cdot \rho_\mathrm{p} \cdot v_\mathrm{tip}}{3 \cdot \eta_\mathrm{f} \cdot Re_\mathrm{p} \cdot c_\mathrm{D} \cdot d_2}. \tag{2.21}$$

For the macro-scale Stokes number St, τ_p is calculated as described in the micro- and meso-scale. However, τ_f is replaced by the overall average circulation time $\tau_f = \bar{t}_{\mathrm{c,overall}}$, which is obtained from experiments [Rei12].

The Stokes number St indicates a flow-following behavior for a particle in the fluid. When considering a particle, an innovative method is the integration of sensors within a particle. An important property for these sensors is a flow-following behavior, which can be determined by the Stokes number St.

2.4 Lagrangian Sensor Particles

Within a stirred bioreactor, cells are exposed to changing fluid velocities as the cells move through the reactor. Distinct mixing behaviors are characterized as compartments. To achieve a high product yield, a homogeneous distribution of cells, oxygen, temperature and pH-value is striven for. Common measurements in industry are based on the Eulerian approach, which is a simpler measurement method compared to the Lagrangian approach, as it consists of fixed installed sensors. However, the Eulerian approach solely provides information about the specific measurement point and cannot be used to characterize the mixing behavior or detect compartments within the reactor. A sensor type based on the Lagrangian approach is the Lagrangian Sensor Particle (LSP), which is directly integrated into the moving fluid while simultaneously measuring process data. LSPs are used to provide an overall picture of the reactor, by achieving a sufficient flow-following behavior.

In this Section, first the pressure sensor is described in more detail, as this work is focusing solely on this sensor type. In the following, the state of the art of LSP designs are discussed, as LSPs exist in different sizes, densities and shapes. Afterwards, calculations based on the pressure data are presented regarding the axial velocity, height, circulation time and the Lagrangian Regime Analysis.

2.4.1 Pressure Sensor

A number of sensors can be used to measure process conditions. The most commonly used sensors are the temperature sensor, the pressure sensor, the pH sensor, the dissolved oxygen sensor (DO sensor) and the Inertial Measurement Unit (IMU). The sensors must be designed so that the particular operating conditions are measured and their respective ranges are covered.

Pressure sensors are employed to measure pressure and, thus, can also be utilized to measure the axial depth, when utilizing an immersed sensor. In general, a non-electrical input signal is measured

by a pressure sensor, which is then converted into an electrical output pressure [Sch18]. Through processing electronics, the input signal is analyzed and transferred into a final sensor output signal [Sch18]. Variation exists in how the sensors detect hydrostatic pressures. The piezoelectric effect measures the deformation of materials due to the surrounding pressure, resulting in an electrical voltage within the material [Sch18]. By displacing positive and negative charges in the materials, an electrical polarization is generated, measurable through an electrical voltage [Sch18]. Examples of such materials include piezoelectric crystals and ceramics. The resistive and piezoresistive effect detects the specific electrical resistance induced by the stretching or compression of a conductor. In a magnetoresistive sensor, the resistance is influenced by the magnetic field [Sch18]. These sensors are often filled with a liquid, such as silicone oil. Pressure sensors vary significantly in terms of size, the method of pressure measurement, housing materials, signal acquisition frequency, and the range of measurable pressure [Sch18]. For sensors, filters play a crucial role in data processing and evaluating. Furthermore, in measurements using sensors, interfering signals known as "noise", can superimpose the useful signal. Filters can be used to suppress these interfering signals as far as possible. [Fri98, Wit19] A distinction is made between lowpass filters and highpass filters. Highpass filters permits only high signals above a defined cut-off frequency, while eliminating or reducing low-frequency signals [Mak15]. On the other hand, lowpass filters function to suppress or reduce signals exceeding a set cutoff frequency [Mak15]. A lowpass filter is particularly beneficial in pressure data processing, as it leads to smoother data [Mak15].

2.4.2 State of the Art of Designs

LSPs can be designed in several ways and the data recorded depends on the integrated sensor. Various research groups have been involved in the development of LSPs. In the following, approaches are presented. A summary of the significant information can be found in

Table 2.1.

Table 2.1: Summary of the Lagrangian Sensor Particle, developed by research groups, with the diameter and the integrated sensors.

Group	Diameter d_p /mm	Integrated sensor type
Reinecke et al.	45	Pressure, Temperature, IMU
Hofmann et al.	40	Pressure
Bisgaard et al.	43, 55	Pressure, Temperature
Stine et al.	60	Dissolved Oxygen
Lauterbach et al.	7.9	Pressure, pH
Cabrera et al.	40	IMU
Kamp	20	-
Rautenbach	25, 40	-
GopalSingh	40	Pressure, IMU

Reinecke et al.

The initial LSP design exhibits a cylindrical shape and a diameter of 45 mm. The length and thus density of the LSP is adjustable by an installed piston, so buoyancy neutrality is achieved. The LSP is equipped with a pressure and temperature sensor, as well as a magnetometer. Experiments are conducted in large bio fermenters and waste water treatment plants where Newtonian and non-Newtonian fluids are used to test the sensor particles [Rei14]. Subsequently, the LSP designs are optimized into spherical LSPs. The new LSP design features a pressure sensor and an IMU. The data collected is stored on an internal SD card, which is later processed and analyzed. The axial position is determined using hydrostatic pressure data, while the magnetometer provides information on the radial position due to the generation of a magnetic field within the reactor by a fixed

coil [Rei14]. The research aim was to gain insights into circulation time and particle postions within the reactor [Rei14].

Hofmann et al.

Hofmann et al. investigates particles with a size of 40 mm (Figure 2.7) in a 15,000 L reactor equipped with three EE impellers [Hof22]. The LSPs features a pressure sensor. The recorded data is stored on an internal memory card for further analysis. The aim of the research is to investigate the flow-following behavior, mixing behavior and a general application of LSPs in STRs [Hof22]. The main results include the axial position within the reactor, the axial velocities, the circulation times, the residence times and the Lagrangian hydrodynamic regime analysis [Hof22]. The circulation time is calculated with pressure data from the sensor. For that purpose, horizontal planes within the reactor are observed, which can be considered as detection planes. The required time from crossing the detection plane until entering it from the same direction, therefore achieving a loop, is considered as circulation time [Hof24]. Furthermore, the Circulation Time Distribution (CTD) is calculated for a specific detection plane from all circulation time measured for this specific plane. The mixing time is measured and set into ratio with the overall circulation time, exhibiting a ratio of 1 [Hof24]. It is observed, that in total three compartments are detected, which are located above the EE, below the EE and in between the upper and lower impeller [Hof22].

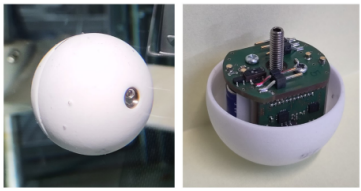

Figure 2.7: The LSP has a diameter of 40 mm and is equipped with a pressure sensor [Hof24].

Bisgaard et al.

The aim of the study of Bisgaard et al. is to provide a deeper understanding of the mixing processes with regards to the axial velocities, mixing and circulation times, and the respective Circulation Time Distributions (CTD). The LSP consists of a diameter of 43 mm (Figure 2.8) and is equipped with an integrated pressure sensor and a temperature-measuring thermocouple. The experiments are conducted in a 0.58 m^3 and 600 m^3 reactor, with exhibiting a variation regarding the aeration, and impeller setup [Bis21, Bis22]. The 0.58 m^3 reactor is investigated by using either a PB or a RT [Bis21]. The axial positions are calculated with the data from the hydrostatic pressure [Bis21]. The maximum pressure and the minimum pressure are initially determined as reference values for all calculations. The mixing time is determined by adding pulses of 1 pH unit, which are detected by fixed pH-electrodes, and measuring the time until homogenization is reached [Bis21]. The circulation time is calculated with pressure data from the sensor. Moreover, the Circulation Time Distribution (CTD) is calculated for a detection plane from all circulation times measured [Bis21]. Due to the different circulation behavior of a RT and a PB, the CTD of the latter consist of all detected circulation times passing the detection plane at the PB height, whereas the CTD with the RT is a summation of the upper and lower loop [Bis21]. The particle flow-following behavior is investigated by the Stokes number St [Bis21]. Therefore, the particle Reynolds number Re_p is calculated, with the slip velocity v_rel represented by a combination of the axial velocity v_ax, a simulated velocity and the region the velocity is referring to, such as bulk or impeller region [Bis21]. The publication of Bisgaard et al. exhibits, that 2.2 - 2.6 circulations equals the mixing time [Bis21]. The sensor shows an increased flow-following behavior at high impeller speeds for the PB, which is observed from the difference of simulated and measured data [Bis21, Bis22].

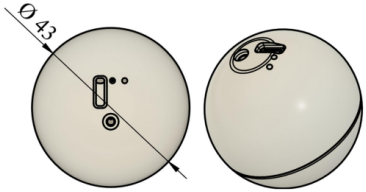

Figure 2.8: An LSP with a diameter of 43 mm, equipped with a pressure sensor, is investigated in a reactor with a PB or RT [Bis21].

Stine et al.

In the studies by Stine et al. a 60 mm LSP, called bio-process online analytical device (bPod) is developed, which is equipped with a DO sensor. Furthermore, the bPod cosists of an Bluetooth low energy microcontroller [Sti20]. The measured data is transmitted to an external receiver via Bluetooth. The DO sensor is calibrated in a 2 L glass vessel, and the experiments are conducted in a 10 L bench scale bio reactor with different oxygen variations [Sti20]. The aim of his research was to investigate the electronic module for signal conditioning and wireless data transmission, investigate an electro chemical sensor for the DO evaluation and design a leak-proof capsule for the sensor [Sti20]. The LSPs showed a linear response to dissolved oxygen concentration [Sti20].

Figure 2.9: LSP, called bio-process online analytical device (bPod), has a diameter of 60 mm and features a DO sensor [Sti20].

Kamp

In Kamp's research, 20 mm Lagrangian Particles (LP) equipped with LED (Figure 2.10) are investigated in a 200 L continuously STR, featuring two different impeller configurations: one with a RT and a PB, and another with two identically PB impeller [Kam22]. Importantly, the reactor exhibits a lack of baffles. The experiments are carried out with different process settings: with and without aeration, and at four different impeller speeds [Kam22]. For each experiment five LPs are used. Since no sensor is employed, the detection of the LPs is achieved by a setup of cameras. A calibration of the cameras is required before the experiments [Kam22].

The primary objective of this study is to investigate flow-following behavior and the particle tracking velocimetry [Kam22]. The results showed that the particles are unable to capture microscale vortices,

but they effectively capture overall flow phenomena [Kam22]. Additionally, a preference for higher mean velocities and acceleration magnitudes is observed when using a combination of RT and PB impeller compared to the PB-PB setup [Kam22].

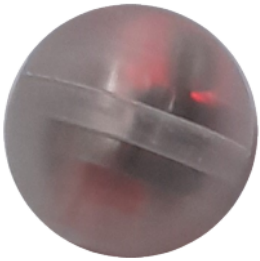

Figure 2.10: Lagrangian particle equipped with LED are designed and tested in Kamp's thesis [Kam22].

Rautenbach

In the thesis of Rautenbach the influence of a shifted mass within an LP is investigated [Rau23]. The aim of this work is to determine the influence of weight eccentricity on the flow-following capabilities of an LSP, since in general built-in sensors within an LSP do not consist of an equatorial centered mass, but rather a displaced one. Two different sizes (25 mm and 40 mm) are investigated exhibiting a centered mass and a shifted mass distribution, which is achieved by centered (equatorial) or off-centered weight [Rau23]. The LP is shown in Figure 2.11. The experiments are conducted within a 50 x 60 x 10 cm rectangular tank with deionized water. The flow within the rectangular tank was assumed to be a stationary circular flow. The velocities in the experiments are tracked with a setup of cameras and no integrated sensor is used [Rau23].

Figure 2.11: LSPs with 25 mm equatorial LP and cylindrical brass insert (top left). The 40 mm off-centre LP with a brass insert with unbalanced mass distribution (top right). Closed 25 mm equatorial and 40 mm off-centre LP (bottom)[Rau23]

The results showed that with an increment of the particle diameter the flow-following behavior decreased. Furthermore, the effects of the eccentric weight were more diverse [Rau23]. In general, the equatorial balanced particle tend to have a better flow following behavior according to the Stokes number [Rau23].

2.4.3 Calculation of Axial Position

Using LSPs provides the advantage of dynamic movement within the reactor, allowing for real-time tracking. In order to be able to trace the axial path, the pressure data is monitored. An LSP equipped with an integrated pressure sensor detects varying pressures as it moves within the reactor. The pressure detected is described by

$$p = p_0 + g \cdot \rho_\mathrm{f} \cdot z, \tag{2.22}$$

equaling the sum of the atmospheric pressure p_0 and the hydrostatic pressure $p_z = g \cdot \rho_f \cdot z$ [Rei14].

The highest pressure is measured at the bottom of the reactor, as it results from the sum of the atmospheric pressure p_0 and the

hydrostatic pressure p_z, which includes the fluid density ρ_f, the fluid height $z(t)$ measured from the top and gravity g. The pressure is lowest at the height of the liquid level H, as only the atmospheric pressure acts on the pressure sensor and a maximum pressure p_{max} is reached at the reactor bottom. Another pressure observes in a stirred tank reactor is the back pressure p_s. It is generated in the immediate vicinity of the agitators. These dynamic pressures only occur in the limited and minor volume fraction of ≈ 1 % in reference to a biogas fermenter $V_{BF} < 1000$ m^3 [Rei14].

The back pressure is neglectable in the calculation of the axial position, since the back pressure $p_s << p_z$ and $p_s << p_0$. This is also confirmed by experiments conducted by Reinecke [Rei14], which were carried out in a reactor with a height of 0.755 m with different impeller speeds and fixed pressure sensors at the reactor wall. The results affirmed that dynamic pressure exerts a minor influence on the axial position measurements when considering the entire reactor volume. With larger reactors, the influence becomes even more irrelevant [Rei14].

Necessary for the calculation is a reference pressure of the atmospheric pressure p_0 and the pressure p_{max} at the reactor bottom, both of which must be determined before conducting the experiments. The height can be calculated by

$$z(t) = \frac{p(t) - p_0}{\rho_f \cdot g}. \tag{2.23}$$

This height $z(t)$ represents the immersion depth at a certain time t. Consequently, $z(t) = 0$ equals the liquid level at the top of the reactor and $z(t) = z_{max}$ corresponds to the maximum immersion depth at the reactor bottom [Rei14].

The axial position $h(t)$ describes the position in the reactor, with $h = 0$ representing the reactor bottom and $h_{max} = H$ representing the liquid level. In order to calculate the axial position $h(t)$ at a certain time t within the reactor, the immersion depth $z(t)$ is subtracted from the maximum height of the liquid level $h_{max} = H$, as calculated in

$$h(t) = H - z(t). \tag{2.24}$$

The axial velocities can be calculated by using the height difference divided by the respective time steps, which can be seen in equation 2.25 [Rei14].

$$v_{\mathrm{ax}} = \frac{h_{\mathrm{t1}} - h_{\mathrm{t0}}}{t_1 - t_0} \tag{2.25}$$

2.4.4 Circulation Time

In a moved fluid, different mixing behavior is observed. Depending on the length scale examined, the mixing is distinguished into the micro, meso and macro mixing. The mixing time $t_{\mathrm{mix,global,95}}$ and circulation time t_{c} are categorized as macro mixing [Fit21].

The two terms mixing time and circulation time are first distinguished. The mixing time $t_{\mathrm{mix,global,95}}$ describes the duration required until homogenization within the reactor is reached. Whereas the circulation time t_{c} is defined as the time that an element takes to return to a specific reference plane, thus, completing a full circle [Bis21].

The mixing time can be classified into the global and local mixing time. The global mixing time describes the mixing time of the complete observed system, whereas the local mixing time divides the system into cells or cubes and observing the mixing time for each cell respectively [Fit21]. The global mixing time $t_{\mathrm{mix,global,95}}$ is proportional to the circulation time t_{c}, as a fluid element passing through the reactor requires an amount of "runs" on a circulation loop until the reactor is considered as fully mixed. As a rule of thumb, the time required for five circulations corresponds to the mixing time in a vessel stirred by a RT impeller [Kha76, Hol64].

The time for one circulation starts $t_{\mathrm{c}} = 0$ as soon as the LSP enters the reference plane (Figure 2.12). A full circulation loop is achieved, when the LSP re-enters the reference plane from the same direction from which the loop originated [Hof24]. This implies that

LSPs initiating a circulation loop from top to bottom also complete the loop from top to bottom. The measured time for a full circle corresponds to the circulation time t_c.

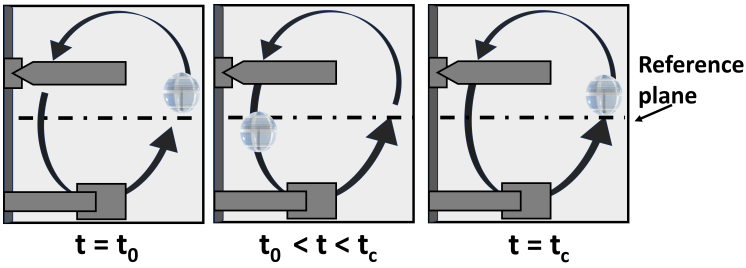

Figure 2.12: Schematic illustration of a circulation loop, with the respective circulation time. The dashed line describes the reference plane.

When detecting a reference plane within the reactor over a time period, it can be observed that the LSP is crossing the reference plane several times, resulting in a quantity of circulation times t_c. From the circulation times, it is possible to calculate an average circulation time $\bar{t}_c$ or a Circulation Time Distribution CTD. When calculating the average circulation time, the total reactor height is divided into horizontal planes, calculating an average circulation time for each detection plane. The reactor height can be displayed with the average circulation time for the heights, respectively [Rei14, Hof24]. Furthermore, $\bar{t}_{c,overall}$ is calculated from all observed circulation times within the reactor [Hof24].

There are multiple existing circulation loops, resulting in a distribution of circulation loops followed by the particle. The respective distribution of circulation times can be assessed as Circulation Time Distribution (CTD) [Rei14]. A reference plane on the height axis is considered. For an axial impeller, it is typically at the stirrer level within the reactor, since it is the location the fluid is pushed through

and vortexes are generated [Rei14]. Whereas in a radial impeller, the height above and below the impeller are chosen [Bis21]. All circulation times t_c measured for this height are displayed in a probability for certain circulation times to occur. When plotting the CTD for a specific height with one main circulation flow, a log-normal distribution is expected, which is observed in publication of Bisgaard et al. [Bis21], Hofmann et al. [Hof24], Oosterhuis et al.[Oos85], and Van Barnefeld et al. [van87]. For a detection plane with two main circulation flows, a bimodal CTD is observed, resulting from two loops respectively [Bis21].

2.4.5 Lagrangian Regime Analysis

Distinct flow behaviors can be observed for particles in a moving fluid within a reactor. The areas with a distinct flow behavior are considered as compartments. Furthermore, the compartments can be identified by displaying the average circulation times $\bar{t}_c$ and average axial velocities $\bar{v}_{ax}$ over the reactor height [Hof24].

The Lagrangian Regime Analysis is a method to investigate the compartments. To do so, the reactor is divided into zones based on a characteristic property, such as a similar flow-behavior or homogeneity [Har18]. In the publication of Hofmann et al. [Hof24], a Lagrangian regime analysis is applied on a single-phase reactor equipped with three EE impellers. The compartments determination in this publication is based on the plots of the average circulation time $\bar{t}_c$, with minimal and maximal values indicating distinct flow behaviors [Hof24]. The compartment borders are marked as horizontal planes within the reactor, as only axial data is evaluated. With the horizontal planes, a similar method to Haringa et al. [Har18] is presented. The residence times of a particle are collected, with each residence time resulting from the time required from a particle entering the horizontal detection plane into the compartment until leaving the compartment by the same detection plane. A probability is calculated from the residence times, which is shown in Figure 2.13. The Figure 2.13 displays the probability of a particle spending a

certain time in a compartment until leaving it [Har18].

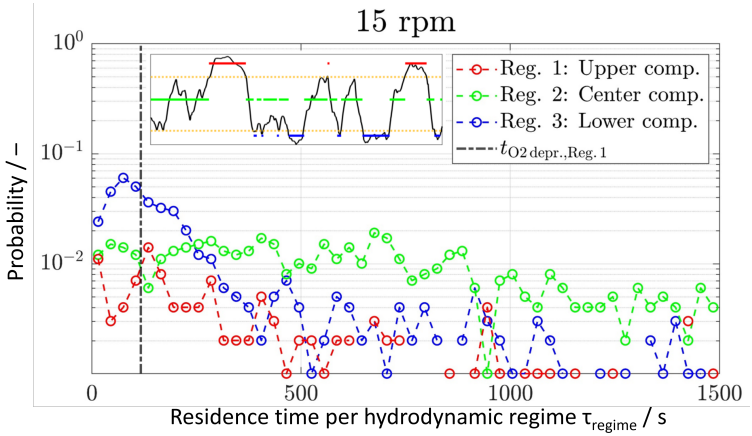

Figure 2.13: Residence time probability distribution per regime for 15 rpm, in a single-phase 15,000 L reactor equipped with three EE impellers. [Hof24]

In bioprocesses, micro organisms are strongly dependent on an adequate supply of substrates and oxygen. An insufficient supply leads to a decrease in the overall yield, as stated in Section 2.1 [Lid02]. By investigating the compartments regarding the time spend in it, inlet streams for substrates can be adjusted, as an inlet stream in a poorly mixed compartment is not efficient.

3 Design and Experimental Procedures

This thesis addresses three main work packages. The first work package (Section 3.1) consists of the design and manufacture of the Lagrangian Sensor Particle (LSP) by means of 3D-CAD Autodesk program Inventor 2024. The second work package (Section 3.2) focuses on the experimental investigation of differently sized LSPs in a 15 m^3 reactor, with adjustments to the impeller speed and consequently the power input. Finally, the third work package (Section 3.3) involves the implementation of a calculation tool using the open source programming language Python™. The developed script is universally usable and applicable, not limited to a specific data set.

In this thesis, two LSP sizes are investigated: the 60 mm diameter LSP (LSP_{60}) and the 40 mm diameter LSP (LSP_{40}). The LSP_{60} is designed and manufactured in this work, whereas the LSP_{40} has already been developed as it is used in previous investigations by Hofmann et al. [Hof24]. Hence, the designing process is described solely for the LSP_{60}. However, the LSP_{40} is introduced as well, as experiments in this thesis are conducted with both LSP sizes.

3.1 Design and Development

The primary objective of LSPs is to achieve flow-following behavior while simultaneously acquiring data on process conditions. To achieve this, it is essential to consider specific requirements for the LSPs such as weight, shape, robustness, manufacturability and, for

economic efficiency, cost-effectiveness. In this section, a more detailed explanation will be provided regarding particle size selection, sensor selection and LSP design utilizing the 3D CAD Autodesk program Inventor 2024.

3.1.1 Particle Size Selection

The first step in the design process is to determine the particle size, which is influenced by a number of factors, such as the technical feasibility and the required flow-following behavior.

For the technical feasibility, the sensor's internals are examined, consisting of the sensor unit, and the components essential for its operation. When focusing on the sensor itself, sizes can vary widely, depending on the specific property targeted for measurement. Furthermore, integrating more than one sensor is beneficial but results in an increase in the overall size of the LSP. Additionally, the potential range of particle sizes is limited due to technical restrictions regarding to battery sizes and the limited miniaturization of data storage and circuit boards.

To estimate the flow-following behavior of the LSP, the dimensionless Stokes number is used. In general, a reduction of the particle diameter, results in a decreased Stokes number, indicating an increased flow-following behavior (Section 2.3.3). Since a miniaturization is not feasible, the focus of the LSP aim is shifted to enable the detection of compartments using the LSP without being able to track micro turbulence. The consideration of larger reactor scales includes influences such as circulation time and macro mixing time [Rei14]. Using the circulation time as a characteristic time scale and a low viscosity medium, a particle diameter of $d_\mathrm{p} = 40$ mm can be reached. When considering higher viscosities, the particle diameter increases up to $d_\mathrm{p} = 100$ mm. To achieve a flow-following behavior a Stokes number $\ll 1$ is aimed for.

Since LSPs with diameters of $d_\mathrm{p} = 20$ mm and $d_\mathrm{p} = 40$ mm have already been designed, the particle size has been chosen deliberately to $d_\mathrm{p} = 60$ mm. Additionally, a larger particle size offers the advan-

tage of allowing the integration of multiple sensors. In industrial processes, reactors are often aerated and the dissolved oxygen (DO) is measured by a DO-sensor. The LSP developed by Stine et al. [Sti20] consists of a DO-sensor and exhibits a diameter of 60 mm. As the overall goal is to implement a LSP in an industrial scale process, the particle size is set to 60 mm, allowing the possibility of integrating a DO-Sensor, and other sensors.

3.1.2 Sensor Selection

For both, LSP_{40} and LSP_{60}, the pressure sensor 89BSD-006BA-A from the manufacturer TE Connectivity is selected for the pressure measurements, which is shown in Figure 3.1. It is made of stainless steel with an O-ring seal. The sensor is an absolute, sealed gage with a diameter of 9 mm and a length of 25 mm. The sensor measures the temperature in the range of -22 to +85 ° C, with an accuracy of ±2 °C and pressure in the range of 0.00 to 6.00 bar, with an accuracy of ±0.03 %span. It is applicable for different systems, such as corrosive fluids and gas measurements. The minimal conversion time is 0.48 ms and the maximal is 8.22 ms.

Figure 3.1: Selected pressure sensor 89BSD-006BA-A from the manufacturer TE Connectivity [Dig23].

The sensor has a digital output (24-bit analog-to-digital converter (ADC)) and is connected to the micro controller (MC) STM32L562 via an I^2C bus. The MC collects the pressure and temperature data with a sampling frequency of 50 Hz and stores them on an SD card in Version 1 (LSP_{40}, LSP_{60}) or on a Not-And (NAND)-flash storage in Version 2 (LSP_{40}) .

In addition to the pressure and temperature sensor in LSP_{40} and LSP_{60}, solely the LSP_{40} is equipped with an internal measurement unit (IMU), and therefore includes motion sensors such as an accelerator, gyroscope and magnetometer. The built-in gyroscope is from Bosch BMG250 with a measuring range $\pm$ 2000 $^{\circ}s^{-1}$. The accelerometer from Analog Devices ADXL355 with a range of $\pm$ 8 G. The magnetometer is the Memsic MMC5983MA with a measuring range of $\pm$ 800 uT. A schematic illustration of the integrated electronic devices is shown in Figure 3.2. This thesis focus solely on the pressure data, as both LSPs consists of a pressure sensor. The IMU data is neglected.

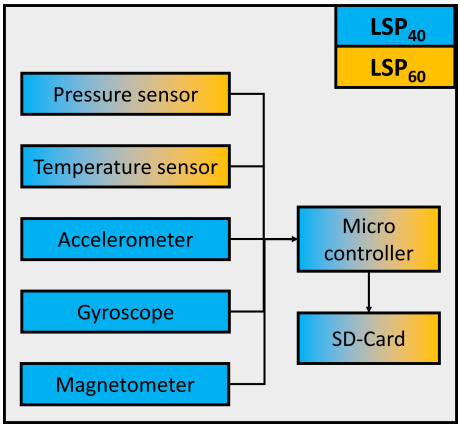

Figure 3.2: Schematic illustration of the LSP_{40} and the LSP_{60} with the electronic devices. Both LSP sizes consist of a pressure and temperature sensor. LSP_{40} is additionally equipped with an IMU.

3.1.3 Design of the Lagrangian Sensor Particle

The LSP_{60} is based on the LSP_{40} design of Buntkiel et al. [Bun23]. The LSP_{40} is developed in advance at the Helmholtz-Zentrum Dresden-Rossendorf (HZDR) and is not part of this thesis.

The LSP_{60} shells are made of polymethyl methacrylate (PMMA), also referred to as acrylic glass. PMMA has a high impact resistance, is shatterproof and lightweight. It is also a cost-effective and non-toxic polymer [Ali15].

When working with acrylic glass, heat can be generated by the work performed, such as drilling, milling or gluing. This heat in turn creates tension in the material, which first manifests as small cracks, and then spreads throughout the entire material. To counteract this phenomenon and to produce greater stability, the material is slowly heated and cooled down, which is referred to as tempering.

The temper process is divided into three phases: heating phase (1), tempering phase (2), and cooling phase (3), which is shown in Figure 3.3. The temperature for the tempering phase (2) depends on the manufacturing process of the PMMA, as extruded PMMA is tempered at 70 °C and cast PMMA at 80 °C [Tom23]. In this thesis, a 70 mm cast PMMA rod is used.

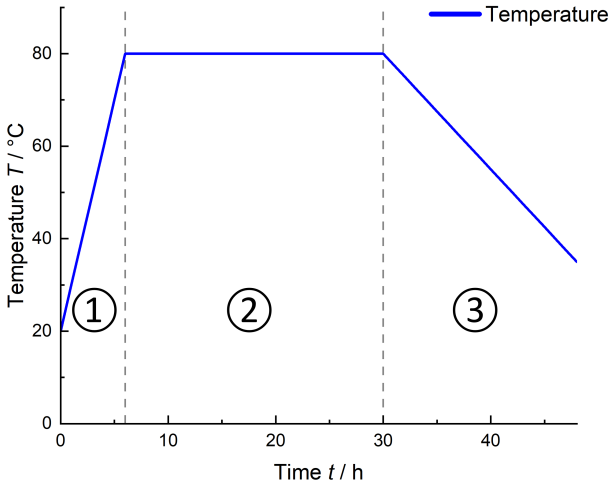

Figure 3.3: Tempering process, with 6 hours of heating time, 24 hours of tempering time at 80 °C, and 18 hours of cooling time.

For the heating phase (1), the PMMA rod is heated from room temperature to 80 °C within 6 hours. For the tempering phase (2), the temperature of 80 °C is maintained for 24 hours. The tempering time results from a rule of thumb, where the material thickness is divided by 3. In the cooling phase (3), the temperature is steadily decreased within 18 hours until room temperature is reached again.

For the cooling time, the material thickness is divided by 4, with the cooling rate not exceeding 15 °C an hour [Tom23].

For the LSP_{60}, the shells are manufactured separately from the inlay which can be seen in Figure 3.4. Following, the three different components will be described more in detail, which will be referred as the top half shell (A), bottom half shell (B) and the inlay (C).

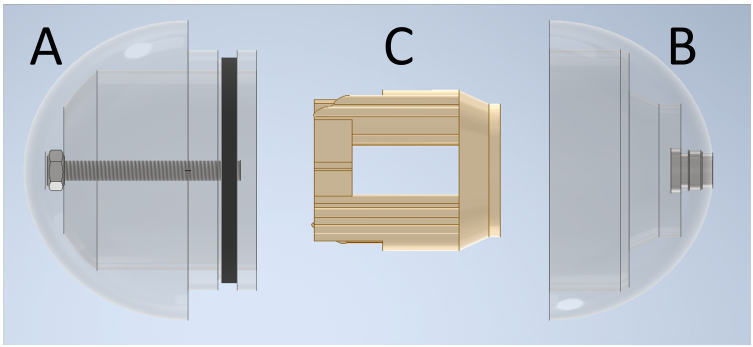

Figure 3.4: Three components of the LSP_{60}: The half shell (A) with an O-ring sealing and an M4 rod, the half shell (B) with a hole for the sensor outlet and the inlay (C) for the inlets, such as batteries, circuit board and SD card.

The top half shell (A), seen in Figure 3.5, is made of PMMA and includes a pre-drilled hole in the center to squeeze in an M4 screw nut. Into the nut, a M4 rod is screwed. To adjust the weight of the LSP_{60}, brass rings are pinned on the M4 rod and are fixed by another M4 screw nut. The brass rings exhibit an inner diameter of 4.5 mm, an outer diameter of 12.25 mm and a height of 1 mm. To ensure a sealed LSP, an O-ring with a cord thickness of 2.6 mm and an inner diameter of 42.52 mm made of ethylene-propylene-diene-monomer (EPDM) rubber is integrated. The material EPDM is resistant to polar liquids, hot water and steam [Lud23], which is suitable as the experiments are conducted in water.

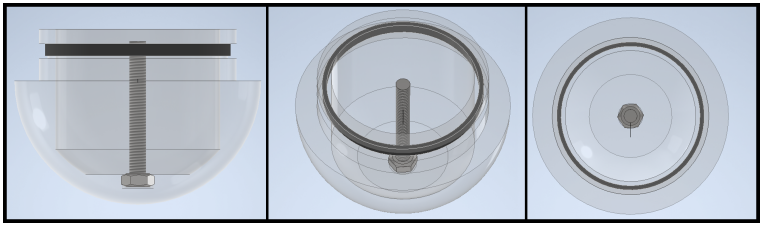

Figure 3.5: Different angle on the top half shell: Side view (left), beveled top view (center), top view (right).

The bottom half shell (B), which is seen in Figure 3.6, is made of PMMA. In the center of the bottom half shell (B), a hole is pre-drilled, in which the sensor is placed, achieving a direct contact between the sensor and the fluid.

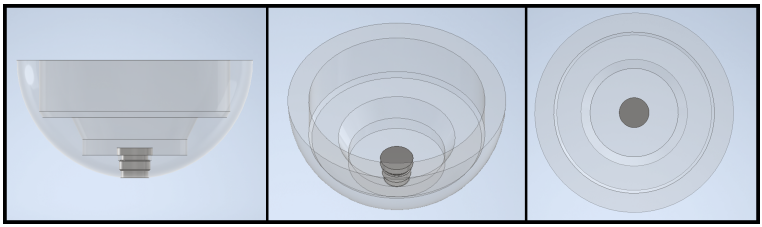

Figure 3.6: Different angle on the bottom half shell: Side view (left), beveled top view (center), top view (right).

The inlay (C), which is seen in Figure 3.7, is based on Buntkiel et al.'s design [Bun23] with minor modifications. It is manufactured by the 3D-printer FormLabs using the clear resin RS-F2-GPCL-04. The purpose of the inlay is to contain the electronics, such as batteries, circuit board and SD card. The inlay is subdivided into three main components: the socket at the bottom, two cylindrical battery holders and a top layer connecting the cylindrical battery holders. The bottom socket is designed to fit into the bottom half

shell (B). Furthermore, a hole in the socket is required to connect the pressure sensor with the electronics. The cylindrical battery holders are placed on the bottom socket. To enhance stability, additional struts were added on the outer walls of the cylinders. The top layer connects both battery holders, achieving a higher stability. Within the top layer, a pre-drilled hole is required in which a melting mother is integrated.

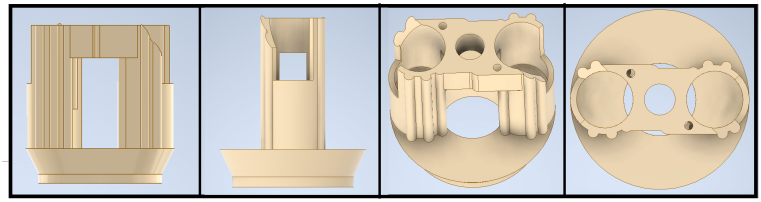

Figure 3.7: Different angle on the inner housing: Side view (left), beveled top view (center left), beveled top view (center right), top view (right).

In Figure 3.8, the assembly of the LSP_{60} is presented. The bottom socket of the inlay (C) is glued into the bottom half shell (B) (Figure 3.4 (middle)). Then the M4 rod of the top half shell (A) is screwed into the melting mother of the inlay (C) (Figure 3.4 (right)). When screwing the shells together, the LSP is sealed as the top half shell (A) is enclosed by the bottom half shell (B).

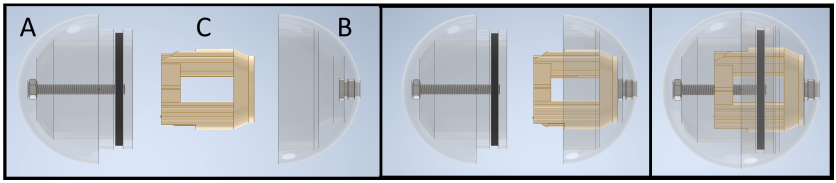

Figure 3.8: Three components of the LSP_{60}: The top half shell (A), the bottom half shell (B), and the inlay (C). The assembly is shown with the three pictures.

The final result of the LSP design is shown Figure 3.9, with the top half shell (A), the bottom half shell (B) and the inlay (C). This Figure 3.9 contains the electronic. The inlay (C) is barley displayed, as electronics are screwed onto the inlay (C).

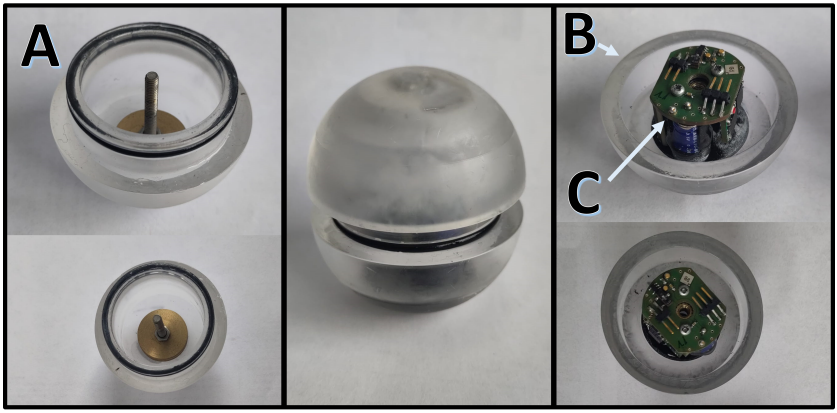

Figure 3.9: The top half shell (A), the bottom half shell (B), and the inlay (C) are presented. The inlay (C) is below the electronics, seen in the right pictures.

3.2 Experimental Investigations

In this section, a detailed description of the reactor and the experimental procedure is provided. First, the reactor setup is presented, followed by the density calibration of the LSPs and finally the experimental procedure is described more in detail.

3.2.1 Reactor Setup

An acrylic glass stirred tank reactor (STR) with a volume of V_R=15 m^3 by Boehringer Ingelheim Pharma GmbH & Co. KG is utilized for the experiments, which is equipped with a bottom mounted magnetic agitator (ZETA BMRF). A Rushton Turbine (RT) and a pitched blade (PB) impeller with an impeller diameter of $d_2 = 0.665$ are used for stirring. The center of the RT is located with a distance of $d_2 = 0.665$ m to the reactor bottom. Above the RT, the PB impeller is installed, maintaining a distance from the center of the PB to the RT of $d_2 \cdot 0.65 = 1.097$ m and thus a total distance of 1.762 m to the reactor bottom is maintained. Three baffles are installed with a distance of 120°. The STR with this setup can be described by a Newton number Ne of 6.5. An illustration of the reactor set-up and significant dimensions is shown in Figure 3.10.

For heating purposes, a pump and a heat exchanger are integrated into the system. This setup allows for the circulation of water from the reactor's bottom through the pump and heat exchanger, effectively rising the water temperature to the desired value. Temperature sensors are placed within the reactor to control the heating.

The reactor has a diameter of $d_2 = 2$ m and is filled with deionized water (DW) to an $H = 4.2$ m, resulting in a volume of 12.5 m^3. The temperature is set to 22.0 ± 0.2°C, which corresponds to a density of 998.2 ± 0.1 kg m^{-3}. The experiments are conducted without aeration.

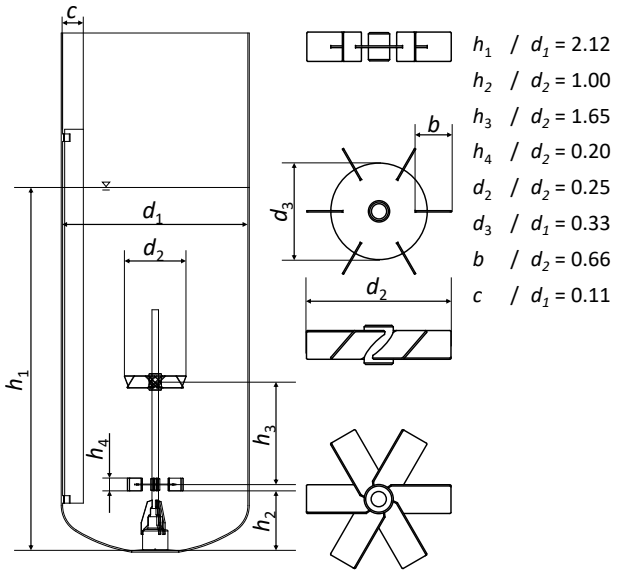

Figure 3.10: Schematic illustration of the reactor which is equipped with a PB and a RT. The constants displayed are: H (reactor height), h_2 (RT height from bottom), h_3 (distance between RT and PB), h_4 (impeller height), d_1 (reactor diameter), d_2 (impeller diameter), d_3 (inner disc diameter), b (blade width), c (baffle width).

3.2.2 Density Calibration

One important property in respect to the flow-following behavior of an LSP is buoyancy-neutrality in the medium, which results from the density of the LSPs corresponding to the density of the target medium. The target medium is DW with a density of 998.2 ± 0.1 kg m^{-3} at a temperature of 22.0 ± 0.2°C. The density is measured with a density meter by Anton Paar GmbH. The density of the LSPs is adjusted in advance of the experiments. For this purpose, two vessels with

a filling volume of $\approx$ 3 L are used. One vessel is filled with DW from the reactor, and the other vessel contains a mixture of DW and NaCl, with a higher density of approximately $\triangle\rho = 1.6 \pm 0.1$ kg m^{-3} between the two vessels. Both vessels are heated in a water bath to a temperature of 22.0 $\pm$ 0.2°C. The density of the DW from the reactor is 998.2 $\pm$ 0.1 kg m^{-3} and of the NaCl-DW mixture 999.8 $\pm$ 0.1 kg m^{-3}.

The densities of the two vessels are chosen with a density difference of $\triangle\rho = 1.6 \pm 0.1$ kg m^{-3}, so that the LSP slowly sinks in the water from the reactor (DW) and slightly rises in the vessel with the NaCl-DW mixture, resulting in a quasi neutrally-buoyant LSP.

3.2.3 Experimental Procedure

The experiments are carried out with the LSP_{40} and LSP_{60}. The process settings for the experiments are listed in Table 3.1. Three runs are carried out for each of the five different rpm settings, resulting in a total of 15 runs.

Table 3.1: Experimental settings.

	Stirring frequency n /rpm				
	24	32	40	55	63
P V^{-1} \W m^{-3}	4.32	10.24	20.00	52.00	78.14
v_{tip} \m s^{-1}	0.84	1.11	1.39	1.92	2.19
Re_{STR} ($\cdot 10^5$) \–	1.77	2.35	2.94	4.05	4.63

Before the experiments are conducted, the density of the LSPs are calibrated, which is carried out as described in Subsection 3.2.2. Afterwards, they are positioned on the top of the reactor wall for at least a minute in order to recognize a clear starting point from the pressure data. The stirrer frequency is set at least five minutes before conducting the experiments to achieve a fully developed flow.

After one hour, the LSPs are removed from the reactor and the

time measurement is stopped. The LSPs are positioned again on the top of the reactor wall to identify the measurement stopping point in the pressure data.

3.3 Data Processing and Evaluation

After the experiments are conducted, the data is stored and pre-processed before proceeding with calculating and evaluating the data.

3.3.1 Data Preparation

The sensor data is saved on the SD card or NAND flash device integrated within the LSPs. After each experimental run, the LSPs are opened and the data is transferred and stored on an external hard drive. In order to prepare the data, it is essential to collect the meta data in an eXtensible Markup Language (XML) file. Furthermore, the raw data is saved on the hard drive. The storing chain is shown in Figure 3.11.

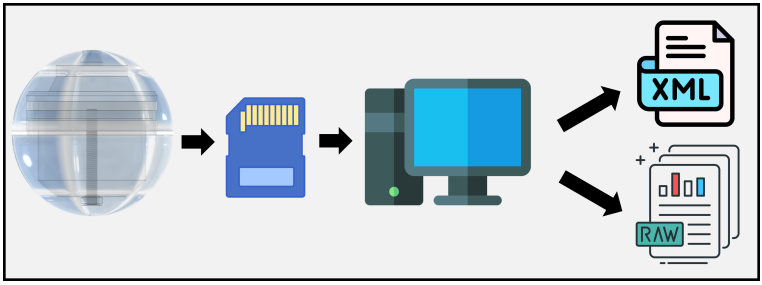

Figure 3.11: Data flow from LSP and integrated pressure sensor to storage device to the hard drive, which is further processed to a XML-file.

In Figure 3.12 a snippet of the XML file is shown. The XML file

contains all necessary meta data to process the raw data set, which is accessed by the Python™ script. For each measurement a time range to determine the respectively measured average ambient pressure is manually selected, which is referred to as air pressure timestamp. Additionally, an initiation and termination timestamp for the data set being evaluated, must be chosen, which is called data evaluation timestamp. Furthermore, the experiment run number is saved in an XML file along with information regarding the frequency of data collection, fluid density, data set file path, and the stirrer rpm of the run. Each LSP is assigned with specific IDs which are consistent throughout the experiments and serve as a recognition. These IDs are also stored on the XML file.

```
<dataset>
  <agitator_setup>
    <stirrer>
      <stirrer_rpm>24</stirrer_rpm>
      <stirrer_type>Rushton turbine</stirrer_type>
    </stirrer>
  </agitator_setup>
  <air_pressure_timestamp>
    <t_start>350</t_start>
    <t_stop>430</t_stop>
  </air_pressure_timestamp>
  <data_evaluation_timestamp>
    <t_start>540</t_start>
    <t_stop>4140</t_stop>
  </data_evaluation_timestamp>
  <experiment>4</experiment>
  <file_path>daten\v4-sp11-60mm_pressure_data.mat</file_path>
  <fill_level>4.2</fill_level>
  <fluid_density>998.1</fluid_density>
  <sensor_particle_id>11</sensor_particle_id>
  <stirrer_rpm>24</stirrer_rpm>
</dataset>
```

Figure 3.12: Snippet from the XML file as an example for how data is saved and are accessed.

3.3.2 Data Processing

Python™, an open source programming language, is used with the Spyder environment to process the data. The structure of the python code is roughly presented in Figure 3.13. Two Python™scripts are used, which is the "Data Pre-processing"-script and the "Calculation"-script. The code for the data processing is stored in the GitLab repository. The raw data is available through the DaRUS repository.

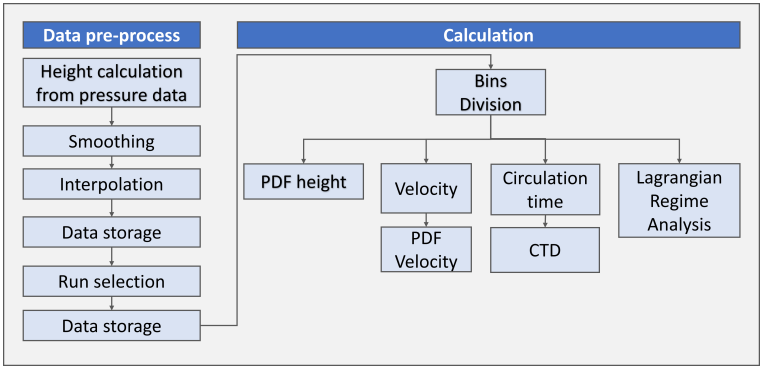

Figure 3.13: Python script handling and schematic structure of the code.

Depending on the LSP size investigated, the code is adjusted before running the script, as the calculation of both LSP sizes at similar time is not implemented in the code. In the following, the "Data Pre-processing"-script is described more in detail. The heights are calculated by using equation 2.23 for each collected pressure data by using the averaged ambient pressure from the XML file. The height data is smoothed by using a low-pass filter with a moving average of five to eliminate rogue data which are attributed to fluctuations in the pressure data. Subsequently, all data is interpolated to match the same time steps of 50 Hz, to achieve a consistent timeline across the data set. This is crucial, since the actual frequency may differ to

50 ± 2 Hz. After smoothing and interpolating, the data set is saved in respective data lists according to the impeller frequency. From all data, the heights of the representative runs and the maximum time line are selected and saved in a new document for further calculations.

3.3.3 Bin Size Selection

The selection of bin sizes is crucial for calculating weighted averages across the normalized height of the reactor. In publication of Hofmann et al. [Hof24], a bin size of 100 mm is selected while using the LSP_{40}, whereas Bisgaard et al. [Bis21] utilizes a bin size of 46 mm with a 43 mm LSP. This results in a bin-to-diameter ratio of 2.5 for Hofmann's study and 1.07 for Bisgaard's. Increasing the bin size reduces localization accuracy, as data points are assigned to larger bins. For 100 mm, the LSP_{60} consists of a bin size-to-diameter ratio of 1.67, which is inbetween the two prior stated ratios. Moreover, a 100 mm bin size exhibits the advantage of a direct comparability of the results of Hofmann et al.[Hof24]. In the following calculations, the bin size of 100 mm is selected.

3.3.4 Calculation

The Python "Calculation"-script (Figure 3.13 (right)) consists of the main calculation steps, including all relevant variables and results. The "Calculation"-script accesses the "Data Arranging" file which includes all of the relevant functions.

At first, the maximum height $H = 4.2$ m of the reactor is divided by the bin size of 100 mm, resulting in 42 bins. The probability of presence is calculated by sorting the heights into the respective bins. Sorting one height into a bin is detected as one count in the bin. Hence, after all heights are sorted, the counts in the bins represents, how often this respective height interval is detected. From this, the probability of presence is calculated.

Furthermore, the axial velocities v_{ax} are calculated by subtracting the axial positions and dividing them by the time derivative (Equation 2.25). The axial velocities v_{ax} are divided into absolute velocities, positive velocities $v_{\mathrm{ax,pos}}$ and negative velocities $v_{\mathrm{ax,neg}}$. The velocities are combined with the respective height they are detected at and can be sorted into the respective bin. A weighted average velocity $\bar{v}_{\mathrm{ax}}$ is calculated from all velocities detected in a bin, resulting in 42 average velocities. Hence, the average velocities can be plotted over the height. Another approach is to calculate the probability for certain velocities to occur. The maximal velocity $v_{\mathrm{ax,max}}$ is divided into 50 velocity intervals. All detected velocities are then sorted into the respective velocity range.

Moreover, the circulation times t_{c} are determined as described in Section 2.4.4. The center of the bins are defined as planes and mark the initiating timestamp for the circulation times. When the LSP passes the plane in a down streaming motion, the time stamp starts with $t = t_0$. When the LSP re-enters the plane from the same direction, the time stamp is marked $t = t_{\mathrm{detected}}$. The time step difference between the two time markers is considered as the time for one circulation loop. The timestamp is logged every time the plane is passed in a downward direction, resulting in various circulation times t_{c} for this plane. The weighted average circulation time $\bar{t}_{\mathrm{c}}$ per plane is calculated, by averaging all circulation times for this particular plane respective to the counts within the bin. For the Circulation Time Distribution (CTD) the maximum circulation time $t_{\mathrm{c,max}}$ detected for this plane is divided by 50. The calculated circulation loops are categorized into the respective time intervals and the probability density function CTD is calculated for the specific detection plane.

Furthermore, the Lagrangian Regime Analysis can be calculated. First, the reactor is divided into compartments, which are based on the average circulation time $\bar{t}_{\mathrm{c}}$ plot. The plot displays heights within the reactor of minimal and maximal circulation times, indicating different mixing behaviors, between the peaks, the compartment borders are placed. For each compartment, the time is measured

from the LSPs entering the compartment until exiting the compartment. This respective time is considered as the residence time in the hydrodynamic regime. A possible large residence time is divided into time intervals. For each compartment, the residence times are categorized into the time intervals, resulting in the probability of the LSP for the time spent in the respective compartment.

Every result obtained from the collected data of the particular LSP and run, such as heights, velocities and circulation times, is averaged and weighted regarding the amount of the size of the specific data set and respective counts, to ensure comparability of the results. Furthermore, an uncertainty is calculated.

4 Results and Discussion

In this section, the results of the experiments are presented, including the Stokes number estimation, the probability of presence over the reactor height, the calculation of axial velocities, the circulation time, the Lagrangian regime analysis and the correlation of mixing time and circulation time. Moreover, possible errors are discussed.

4.1 Stokes Number Estimation

The Stokes number St is defined as the ratio of the characteristic response time of the particle τ_p to adapt to changes of the fluid, to the characteristic time length τ_f of change of the fluid. Depending on the mixing scale observed, the Stokes number St is distinguished between the micro-, meso-, and macro-scale and is calculated for the utilized impeller frequencies as listed in Table 4.1.

The Stokes number calculations are based on the approaches of Hofmann et al. [Hof24] and Reinecke [Rei14].

The meso-scale Stokes number St reported by Hofmann et al. ranges from $0.17 < St < 0.18$ for three Elephant Ears (EE) impellers. For Bisgaard et al. a $St = 9$ for the Rushton Turbine (RT) setup and a $St = 36$ for the pitched blade impeller (PB) setup is estimated, and for Reinecke a value of $St > 10$ with a PB is calculated. In the macro-scale, the Stokes number St results in $St \approx 0.06$ for Hofmann et al. [Hof24], in $St < 0.05$ for Reinecke [Rei14], and in $0.20 < St < 0.46$ for the RT setup and $0.33 < St < 0.74$ for the PB setup in the publication of Bisgaard et al. [Bis21].

The estimated St in this thesis are in the same range as the results of Barnevald et al. [van87], Reinecke [Rei14], Hofmann et al. [Hof24]

and Bisgaard et al. [Bis21]

Table 4.1: Overview of the results of Stokes numbers St in different scales.

	Stirring frequency n /rpm				
Micro-scale	24	32	40	55	63
LSP_{40} St /-	2.9	3.3	3.7	4.4	4.7
LSP_{60} St /-	4.2	4.7	5.5	6.4	7.1
Meso-scale					
LSP_{40} St /-	$St \approx 0.21$				
LSP_{60} St /-	$0.31 < St < 0.32$				
Macro-scale					
LSP_{40} St /-	$0.002 < St < 0.003$				
LSP_{60} St /-	$0.003 < St < 0.004$				

For the macro-scale flow, a sufficient flow-following behavior is assumed, as it results in $St \ll 1$.

4.2 Probability of Presence

The probability of presence describes the probability that the LSP is located at a particular height. To determine the probability, the heights are calculated from each pressure data set and sorted into the corresponding height bin. An increased probability for a particular height represents a bin in which the LSP is frequently detected. In this section the probability of presence is plotted over the normalized reactor height h_{norm}.

In Figure 4.1, the probability of presence is plotted for the LSP_{40}.

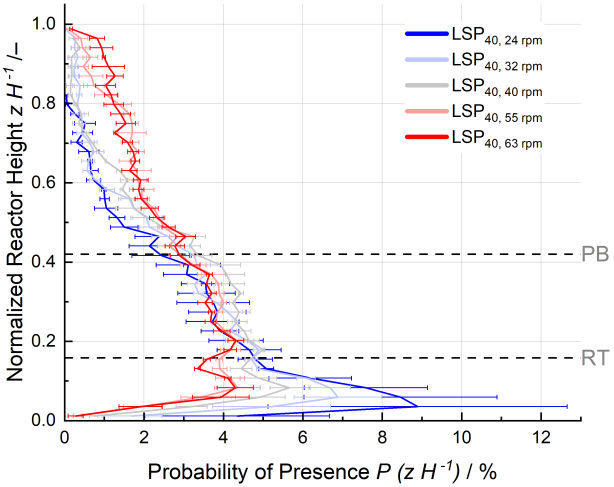

Figure 4.1: Axial probability of presence of LSP_{40} over the normalized reactor height (H= 4.2 m) with a vertical bin size of 0.1 m calculated for each impeller frequency (24 rpm, 32 rpm, 40 rpm, 55 rpm, 63 rpm), including the respective uncertainties. The horizontal lines represent the center of the RT and PB, respectively.

The probability reaches a peak for all impeller frequencies, at the reactor bottom, up to the lower dashed line, which indicates the middle of the RT impeller stage. In this area, the overall highest probability over the total height is observed for the impeller frequencies of 24 rpm, 32 rpm and 40 rpm, whereas for the impeller frequencies of 55 rpm and 63 rpm, a comparable lower peak is detected. Both impeller frequencies do not consist of an overall maximum peak over the total height. The highest peak occurs at the lowest impeller frequency of 24 rpm. With increasing impeller frequencies, the peak

decreases and is shifted slightly towards a higher height. At a decreased impeller frequency, a reduced $P\,V^{-1}$ input is induced into the system. The vortices generated by the impeller exhibit a lower energy level, resulting in a turbulence on macro-scale with a limited decay of the vortices and furthermore, a limited mixing behavior within the reactor. With a limited turbulence on macro-scale, the LSPs are influenced more stronger by the inertia, as the particles exhibit a constant velocity, when no further force is influencing the particle. The RT produces a radial flow, which is pushed towards the wall, resulting in an upwards and downwards movement. The height of the peak indicates the changing point from axial to radial flow and furthermore, exhibits the turning point of the lower circulation loop. For lower impeller frequencies, the radial movement is followed through more slowly by the LSP, resulting in an increased presence. As the inertia is strongly dependent on the mass, the density adjustment for the LSP at lower impeller frequency becomes more evident. Between the impeller frequency of 40 rpm $\leq n \leq$ 55 rpm, an increment of the macro turbulence is observed, since the impeller frequencies higher than 55 rpm do not consist of an overall significantly increased probability below the RT.

Between the RT and the PB, the probabilities for all frequencies are in a similar range with their respective uncertainties. Two notable sections in this area are observed. The first section is located directly above the RT at $h_{\mathrm{norm}} = 0.20$ and exhibits a peak at all frequencies. For the 24 rpm the peak is barely detectable. As the impeller frequency increases, the peak above the RT also increases. This results from the increased turbulence on macro-scale at higher energy level within the fluid, as a higher $P\,V^{-1}$ input is utilized. The inertial forces are less influencing at higher impeller frequencies and the LSPs tend to an increased presence above the RT. The peak above the RT can be considered a turning point in the upper circulation loop created by the RT. This occurs as the fluid is pushed radially towards the reactor wall.

The second section, situated between the RT and PB, does not appear as a local peak but rather as an increased probability over a

broader range between $0.27 < h_{\text{norm}} < 0.39$. This section is evident only for 40 rpm, 55 rpm, and 63 rpm. This area indicates the upper turning point of the upper loop generated by the RT, as an increased horizontal movement is detected at this height.

Above the second dashed line, indicating the center of the PB, another peak is detected at $h_{\text{norm}} = 0.46$ directly above the PB for all speeds except 32 rpm. This increased horizontal movement indicates the area for the turning point for the highest main circulation loop, which is assumed to result from the upper circulation loop generated by the RT and the axial loop from the PB merging. As height increases, probabilities for the impeller frequencies of 24 rpm, 32 rpm, and 40 rpm behave similarly, dropping almost to zero above $h_{\text{norm}} = 0.75$. The probability for 55 rpm drops nearly to zero above $h_{\text{norm}} = 0.90$, while for 63 rpm, a probability of 0 is not reached over the total height. Furthermore, decreased impeller frequency shows a decreased probability for an increased h_{norm}. Especially in the area above $h_{\text{norm}} = 0.70$ the probabilities are in similar range with their respective uncertainties, which results from a low data base.

In Figure 4.2 the probability of presence over the normalized height h_{norm} for the LSP_{60} for all impeller frequencies is plotted.

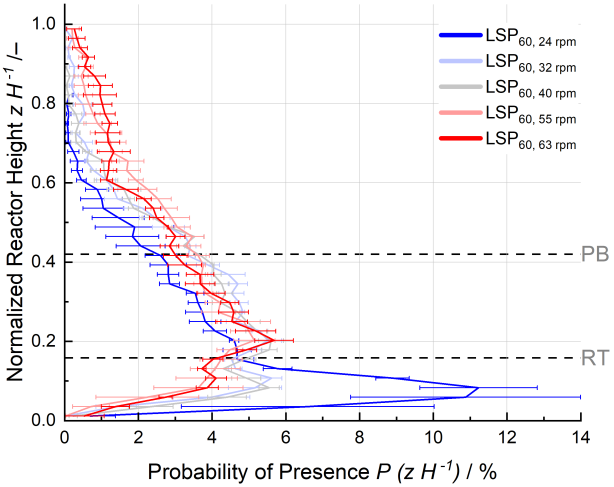

Figure 4.2: Axial probability of the presence of LSP_{60} over the normalized reactor height (H= 4.2 m) with a vertical bin size of 0.1 m calculated for each impeller frequency (24 rpm, 32 rpm, 40 rpm, 55 rpm, 63 rpm), including the respective uncertainties. The horizontal lines represent the center of the RT and PB, respectively.

At the reactor bottom, up to the RT, a distinct peak is observed at frequencies of 24 rpm, 32 rpm and 40 rpm. In contrast to the LSP_{40}, below the RT the probability of presence of the LSP_{60} is significantly higher at 24 rpm. The peak reaches a probability of 11.2 at h_{norm} = 0.08, exceeding the probability of LSP_{40} by 3 % at this respective height. Similar to LSP_{40}, at low impeller frequencies, the area is strongly influenced by the inertia of the particles, the reduced $P\ V^{-1}$ input, and thus, the lack of turbulence on macroscale. Especially the inertia of particles has a great impact at low

impeller frequencies, as it is mass-dependent. The increased mass of the LSP_{60} requires a more sensitive density adjustment. From this, it can be concluded that the LSPs are not fully neutrally buoyant. Furthermore, an increased center of gravity resulting from the brass rings was observed for LSP_{60}, as it exhibits tilting movement. This results in a decreased flow-following behavior; thus, an enhanced energy level in the system is required to set LSP_{60} into motion.

Between the RT and the PB, the probability of presence for LSP_{60} is similar to the probability of LSP_{40} with a peak at $h_{\text{norm}} = 0.20$. In contrast to the LSP_{40}, significant peaks are observed over the total height for 55 rpm and 63 rpm, with a probability of 5.1 and 5.7, respectively. This indicates that the area between the RT and PB is subjected to higher turbulence. However, the increased inertia of the LSP_{60} results in an increased passing of the circulation loops with increased energy. Furthermore, for 55 rpm and 63 rpm, no significant peak below the RT is observed. However, a peak above the RT is detected, indicating a preference for the upper loop at 55 rpm and 63 rpm. It is assumed that the LSP_{60} is caught in the same circulation loop. At 24 rpm, the lower circulation loop is favored, as no peak is observed above the RT.

In the area above the PB, another peak is detected at $h_{\text{norm}} = 0.46$ directly above the PB, as observed with the LSP_{40}. Contrary to the LSP_{40}, the peaks detected are not as distinct noticeable and are rather considered as smooth peaks. Similar to LSP_{40}, the peaks may result from the upper turning point of the circulation loop generated by the PB, whereas the smooth peak is assumed to result from the inertia of the LSP_{60}, which does not exhibit radial movements but rather tangential movements until entering the suction zone induced by the PB. Thus, the peak may indicate the upper barrier of the suction zone. As the LSP_{60} has a larger diameter compared to the LSP_{40}, the LSP_{60} is observed to collide more often with the PB.

Above these peaks, the probability of presence decreases. For 24 rpm, a probability of 0.5 at $h_{\text{norm}} = 0.61$ is observed. The probabilities for 32 rpm and 40 rpm achieve similar low values at a height of $h_{\text{norm}} = 0.70$. For the 55 rpm and 63 rpm probabilities in

the same range are only reached at the top of the reactor. Values above $h_{\mathrm{norm}} \approx 0.60$ are considered with caution, as only low data sets are available.

In conclusion, an increased impeller frequency improves mixing throughout the entire height. This is evident from the probability shifting towards higher heights with increased impeller frequencies, and the LSP is distributed more evenly throughout the altitude. Each detected peak is considered a circulation loop turning point, as predominantly radial movement is observed. Below the RT, the probability of an LSP increases with decreasing impeller frequency. The RT generates a radial flow, displacing the fluid to the reactor wall. A downward movement is detected for the LSP. The probability of presence for the LSP_{60} is highest at 24 rpm, which is also observed for the LSP_{40} and is confirmed by the observations during the experiments, as the LSPs are mainly detected at the reactor bottom. The increased probabilities at the reactor bottom for low impeller frequencies result from the insufficient energy of the inner vortex, which transports the LSP up again at higher impeller frequencies.

In the area between the PB and RT, the probability increases with increasing impeller frequency. The flow from the RT is divided into two circulation loops, the upper loop and the lower loop. The PB transports the fluid axially towards the RT, where the axial flow merges with the radial upper loop from the RT. Therefore, LSPs reach the height of the radial impeller RT more frequently when positioned between the PB and RT. The peaks above and below the RT represent circulation turning points, as the LSPs are pushed axially outward until a radial circulation develops. The LSP only passes through the upper circulation radius at higher impeller frequencies.

In the area above the PB, a peak is detected in the vicinity of the impeller. This increased probability results from the LSP following the upper loop of the axial circulation initiated by the PB. At this height, floating is observed until the LSP is sucked into the stream to start another circulating loop.

Regarding the compartments, both diagrams indicate three dif-

ferent presence behaviors: below the RT, between the RT and PB, and above the PB. However, distinguishing the compartment borders based solely on these diagrams is challenging.

In the publication by Bisgaard et al. [Bis21], the RT and the PB are individually observed. Similarities can be found in the height profiles, such as the peak below and above the RT, and the peak below the PB, as observed in the Figures 4.1 and 4.2. However, in Bisgaard et al.'s plot, no peak is detected above the PB.

In Bisgaard's et al. publication, the following thesis is put forward:"The variation of pk (Probability of presence) with impeller speed when using the PB and not the RT can be explained by a limitation in the flow following capabilities of the relatively large sensor devices" [Bis21]. - This thesis cannot be applied to the diagrams presented here, as a shift in the probability of presence is characterized both below the RT and above the PB. However, it can be seen that the probabilities approach each other at higher impeller frequencies. Bisgaard et al.'s [Bis21] hypothesis is based on a 25-fold decreased reactor volume with a 4-fold higher $P\,V^{-1}$ input, resulting in higher impeller speeds. Hence, an identical distribution between the impeller frequencies is observed, as the experiments are conducted in a highly turbulent regime. Furthermore, the data for Bisgaard et al. [Bis21] is collected at 8 Hz and sorted into a bin size of 4.6 cm, whereas in this study, 50 Hz and a bin size of 10 cm are utilized. Hence, the data of Bisgaard et al. [Bis21] display an increased uncertainty.

In Hofmann et al.'s paper [Hof24], a reactor identical to the one used in this study is equipped with three EE's, which are axially pumping impellers. Furthermore, similar to this study, a decrease in probabilities with increasing impeller frequency for the region below the lowest impeller is detected. The peak recognized results from the turning point of the axial circulation loop. Within the upper and lower impeller, a constant probability is observed. In contrast, in this study, an increment is detected, resulting from circulation loops of the RT and PB. In the EE setup, one main axial loop is generated. This supports the assumption that each peak in the probability of

presence is considered as turning point of a circulation loop.

4.3 Axial Velocity

In this section the average axial velocity $\bar{v}_{\mathrm{ax}}$ is discussed first, followed by the probability density function (PDF) of said axial velocity v_{ax}, each constituting the Eulerian and the Lagrangian analysis, respectively. The LSP_{40} and LSP_{60} are analyzed independently at all impeller frequencies. The two LSP sizes are then compared for selected impeller frequencies.

4.3.1 Average Axial Velocity

The Figure 4.3 displays the average axial velocities of the LSP_{40} for all impeller frequencies over the normalized height h_{norm}, which are divided into positive $\bar{v}_{\mathrm{ax,pos}}$ (solid line) and negative $\bar{v}_{\mathrm{ax,neg}}$ (dashed line). $\bar{v}_{\mathrm{ax,pos}}$ indicate movement towards the reactor top, while $\bar{v}_{\mathrm{ax,neg}}$ describe ascending movement towards the reactor bottom. The Figure 4.3 shows a symmetry between $\bar{v}_{\mathrm{ax,pos}}$ and $\bar{v}_{\mathrm{ax,neg}}$. For the area in between the reactor bottom and RT, almost no quantitative difference can be observed for varying impeller frequencies and for both positive and negative $\bar{v}_{\mathrm{ax}}$.

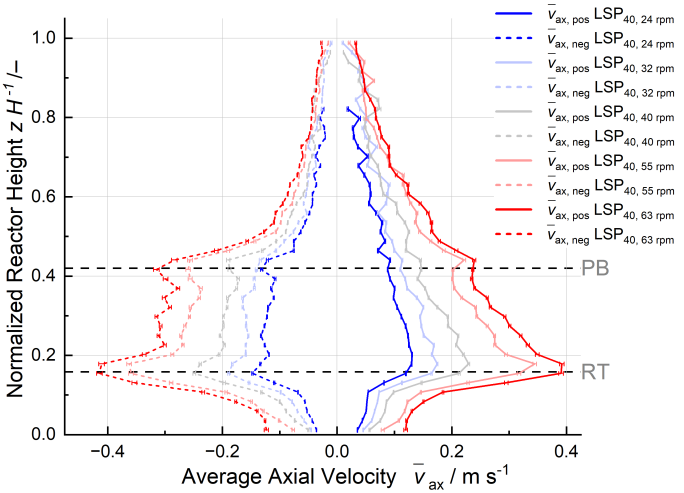

Figure 4.3: Average axial velocities $\bar{v}_{\mathrm{ax}}$ of LSP_{40} over the normalized reactor height ($H = 4.2$ m) with a vertical bin size of 0.1 m is calculated for each impeller frequency (24 rpm, 32 rpm, 40 rpm, 55 rpm, 63 rpm), including the respective uncertainties. The horizontal lines represent the center of the RT and PB, respectively.

The Figure 4.3 illustrates that velocities increase as the impeller frequency increases. A higher $P\ V^{-1}$ input introduces more energy into the fluid, which affects the vortex formation and generates a more extensive macro turbulence. With increasing the impeller frequency, the tip speed v_{tip} increases as well. In the area between the reactor bottom and $0.08 < h_{\mathrm{norm}} < 0.11$, low velocities are observed, resulting from low axial movement. The height indicates the edge of the lower circulation loop, as the LSP exhibits predominantly a radial movement at this height. This can be confirmed, as the

probability of presence exhibits a peak at the same height. Beyond this point, the velocities increase to a maximum at the height of the RT. This results from the fluid being pushed faster towards the outer wall at the height of the radial impeller, so that the fluid generates a stronger upward and downward displacement at this point, which leads to a stronger axial loop formation.

Between the RT and PB, the velocities decrease gradually towards the PB, with another peak being reached at the PB, which results from the axial motion of the fluid, being pushed towards the RT. The positive axial velocity $\bar{v}_{\mathrm{ax,pos}}$ displays a peak rather above the PB at $h_{\mathrm{norm}}= 0.44$. This increased velocity indicates the circulation loop originated by the suction zone. Both detected peaks are more distinct the higher the impeller frequencies and are more clearly recognizable with negative $\bar{v}_{\mathrm{ax,neg}}$. The peak of the RT increases stronger compared to the peak at the PB, which results from the axial flow from the PB merging with the upper circulation loop of the RT. For low impeller frequencies $n = 24$ rpm, it is assumed, that the $P\ V^{-1}$ input is not sufficient enough, to result in the axial flow of the PB and the upper circulation flow of the RT merging.

Above the PB, the axial positive and negative velocities decrease strongly until $0.46 < h_{\mathrm{norm}} < 0.53$, suggesting the upper region of the circulation loop.

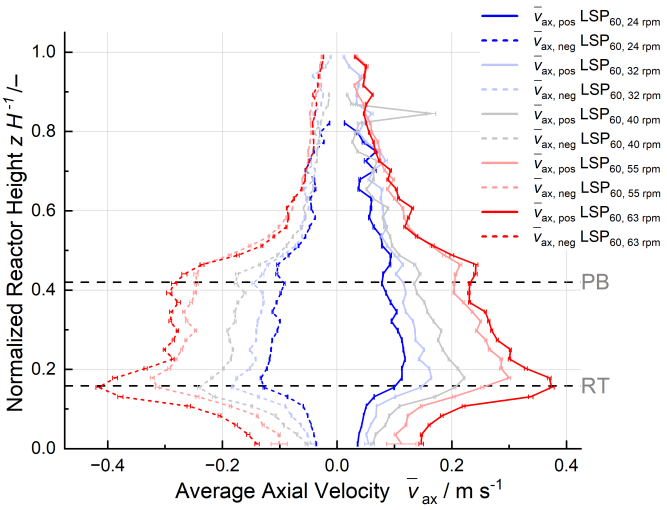

Figure 4.4: Average axial velocities of LSP_{60} over the normalized reactor height (H= 4.2 m) with a vertical bin size of 0.1 m is calculated for each impeller frequency (24 rpm, 32 rpm, 40 rpm, 55 rpm, 63 rpm), including the respective uncertainties. The horizontal lines represent the center of the RT and PB, respectively.

The Figure 4.4 shows the average axial velocities $\bar{v}_{ax}$ over the normalized height for the LSP_{60}. Similar to the diagram for the LSP_{40}, a symmetry is recognized. In the area between the reactor bottom and RT, an increase of velocity with a similar velocity profile as seen for the LSP_{40} is observed in regard to the impeller frequencies over the normalized height h_{norm}. Similar to LSP_{40}, a peak at the height of the RT, which is more distinct at a higher impeller frequency, and a peak at the PB are observed. Between the RT and PB, the velocity decreases with increasing h_{norm}. Between the PB and the top

of the reactor, v_{ax} drops to near 0, with the lower impeller frequency declining more rapidly.

As an exception, one clear outlier can be recognized for $\bar{v}_{\mathrm{ax,pos}}$ at $h_{\mathrm{norm}} = 0.85$. The outlier is based on experiment number 9. In the other experiments no data is detected for this height. For the height below and above the outlier, 234 counts and 283 counts are detected, respectively, whereas for the $h_{\mathrm{norm}} = 0.85$ solely 30 counts are observed, resulting in an at least 8-fold lower data base. The velocities are comparable high to the others velocities in the area. Additionally, the negative axial velocities $\bar{v}_{\mathrm{ax,neg}}$ show a 1.5-fold decrease in counts compared to the heights both above and below the outlier.

When comparing the two LSP sizes at the impeller speeds of 24 rpm and 63 rpm, it can be clearly seen that the velocity profiles are very similar. However, a slightly decreased velocity for the LSP_{60} compared to the LSP_{40} is observed. This becomes evident at the height of the RT, as for 24 rpm and for 63 rpm a velocity difference of 0.02 m s^{-1} between the two LSP sizes is observed. In between the RT and PB, the velocities for both LSPs at 24 rpm are in the same range, exhibiting a close-fitting velocity profile, whereas at impeller frequency 63 rpm, a velocity difference between both LSP sizes is maintained. Above the PB, both LSP sizes display a more distinct behavior at 63 rpm. Contrary, a rather confused behavior is observed, especially above $h_{\mathrm{norm}} = 0.37$, which results from a reduced data base, as the LSPs tend to stay below the RT at 24 rpm.

To summarize, a similar velocity profile is observed. Only in the area above the PB an overlapping of the velocity curves of different impeller frequencies occur, resulting from a low data base.

Two peaks are displayed, one at the RT, and one at the PB for both LSP sizes. The higher the impeller frequency, the higher $\bar{v}_{\mathrm{ax}}$ and the more distinct the peaks, whereas the peak at RT increases stronger than the peak at the PB. The Peak from the PB results from the axial pumping impeller. The RT transports the fluid radially towards the reactor wall. Due to the high impeller frequency, the velocity peaks increase at this height. The faster the fluid is conveyed

radially outwards, the faster it is pushed in either the upper or lower circulation loop. In between the PB and RT, a steady increase of the velocities towards the RT is observed. This leads to the conclusion that the axial flow initiated by the PB, combines with the upper circulation loop of the RT and reaches a maximum at the height of the latter (Figure 4.5). At low impeller frequencies, the velocity peaks at the PB and RT are similar, as the circulation loops of the PB and RT do not interact as strongly as they do at higher impeller frequencies.

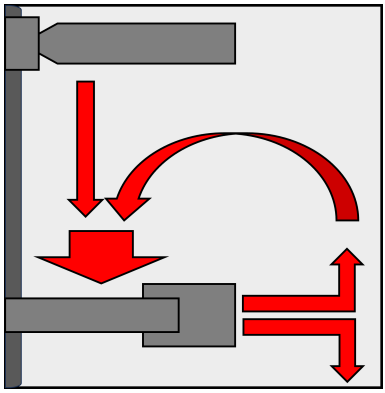

Figure 4.5: Schematic illustration of the velocity peak at the RT. Arrows describing the fluid flow.

The maximum axial velocities are reached for the negative velocities $\bar{v}_{\mathrm{ax,neg}}$ at the RT and are listed in Table 4.2, displaying similar velocities.

Between the reactor bottom and the RT, a sharp increase in velocity can be observed. At approximately the same height, an increased probability of presence is noted (Figure 4.1 and 4.2).

Comparing the results with Hofmann et al. [Hof24] with the three EE, a peak right below the upper impeller and above the lower impeller are detected. Furthermore, also the increment towards

Table 4.2: Maximum velocities $|\bar{v}_{ax}|$ reached with its respective uncertainty and the tip velocity v_{tip} for each impeller frequency.

	Stirring frequency n /rpm				
	24	**32**	**40**	**55**	**63**
LSP_{40} $|\bar{v}_{ax}|$ /m s^{-1}	0.147	0.189	0.241	0.359	0.414
Δ LSP_{40} $|\bar{v}_{ax}|$	0.001	0.002	0.002	0.004	0.005
LSP_{60} $|\bar{v}_{ax}|$ /m s^{-1}	0.128	0.183	0.241	0.322	0.416
Δ LSP_{60} $|\bar{v}_{ax}|$	0.002	0.002	0.002	0.003	0.005
v_{tip} /m s^{-1}	0.836	1.114	1.393	1.915	2.194

the peak above the lower impeller is detectable, which results from the cumulative axial flow. The maximal velocities of the EE are 1.3 to 1.5-fold higher as the RT and PB setup with the same $P\ V^{-1}$ input, which might result from the increased turbulence and vortex formation when a radial and axial flow merge. Whereas in solely axial flow, the stream is pushed in the same direction, resulting in a steady increase in velocities with low vortex formation. Furthermore, this result can be compared with an additional publication of Hofmann et al. [Hof22], where a reactor setup with two RTs is analyzed and the velocity magnitude is plotted over the normalized reactor height. This publication encompassed the axial and radial velocity analysis. Similar to the result from this study, at the RT heights a peak can be observed. However, Bisgaard et al. [Bis21] observed a decrease in velocity at the height of the RT, with peaks occurring just above and below the RT. This observation is a result of the measurements, as the pressure sensor operates at a frequency of 8 Hz and exhibits a reduced bin size diameter of 0.046 m. Concurrently, LSP exhibits faster movements and height fluctuations in response to high velocities. Assuming the LSP is at the bin center, a distance of 0.023 m is required to reach the next bin. The calculated maximal velocity required to still detect the LSP in this bin is obtained by

dividing the distance by the frequency, resulting in a velocity of 0.184 m s^{-1}. If the LSP exceeds this velocity, it is detected in the bin above or below, depending on its movement. The maximal velocities observed in the diagrams presented by Bisgaard et al. displayed velocities higher than 0.184 m s^{-1}. Thus, the measurements of Bisgaard et al. were not able to detect high velocities at the height of the RT.

4.3.2 Probability of Velocity

In Figure 4.6, the positive axial Lagrangian velocity profiles are plotted logarithmically in the range of $0 < v_{\mathrm{ax,pos}} < 2.5$ m s^{-1}, depicting the probability of the velocity occurrence.

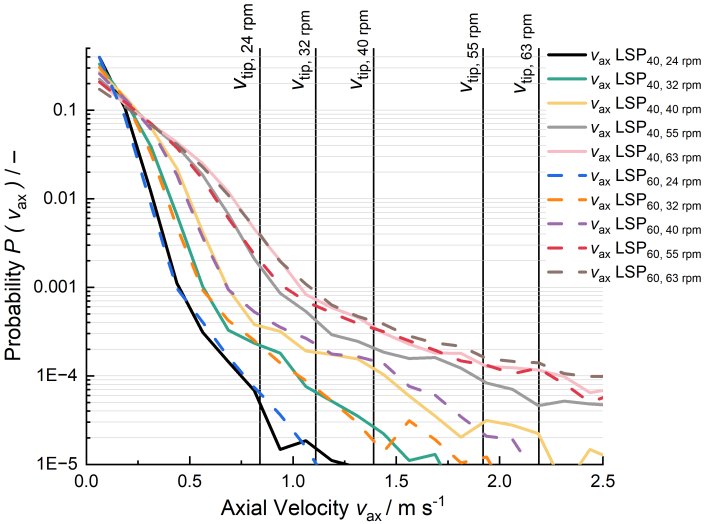

Figure 4.6: Probability of the overall positive axial velocities $v_{\mathrm{ax,pos}}$ of the LSP_{40} and LSP_{60} calculated for each impeller frequency (24 rpm, 32 rpm, 40 rpm, 55 rpm, 63 rpm) using three LSP data sets within a range of 2.5 m s^{-1}. Vertical lines depict the respective tip speed. The class width is 0.0625 m s^{-1}.

In this Figure 4.6, both LSP sizes are plotted with all five different impeller frequencies. The solid lines describe the probability of the LSP_{40} and the dashed lines describe the probability of the LSP_{60}. In addition, the tip velocity v_{tip} of the impeller frequency is plotted using vertical lines. The plot shows clearly, that the probability of certain speeds occurring is almost identical for both LSP sizes, especially for low impeller frequencies. For higher impeller speeds higher axial velocities are more likely to occur, and thus the trend shows a less steep slope.

Furthermore, velocities above v_{tip} for the respective impeller frequency can be observed, however, with low probabilities of less than $1.5 \cdot 10^{-4}$. The assumption that the maximum speed of the LSP equals v_{tip} is refuted by this graph, as velocities exceeding the tip velocity are detected. As the impeller frequency increases, the probability of an axial velocity higher v_{tip} increases. However, for the probabilities of velocities exceeding the tip velocities, fluctuations are observed resulting from the low data base for this velocity range.

Comparing LSP_{40} and LSP_{60}, a minimally lower $v_{\text{ax,pos}}$ for the LSP_{60} at same probabilities can be observed from the velocity curves until a switching point, which is at approximately the half of the tip velocity. This increase is assumed to result from the LSPs colliding on the PB, repulsing in a 45° angle. This was observed frequently during the experiments, especially at high impeller frequencies.

In general, the LSP_{40} demonstrates an enhanced flow-following behavior, resulting in slightly higher achieved velocities. The slightly reduced velocities of LSP_{60} can be attributed to inertia, due to the increased mass of the LSP. Furthermore, with the diameter of the LSP_{60} a flow-following behavior up to the macro-scale eddies is achieved. However, LSP_{40} demonstrates the capability to follow meso-scale flows as well. This potentially leads to a higher number of eddies that the LSP_{40} can follow, resulting in a more continuous movement, with less energy required to accelerate the particle within the fluid. Furthermore, in the transitional zone between the core and exterior of a Rankine eddy, the highest velocity is achieved. Due to the smaller diameter of the LSP_{40}, there is an increased likelihood of precisely following an eddy on this radius.

The observation reveals an increased probability for 55 rpm for the LSP_{60} compared to the LSP_{40}. Hence, the LSP_{60} exhibits a more pronounced upward movement. This phenomenon may be attributed to LSP_{60} colliding more frequently with the PB. One assumption is that, within the impeller frequency range of 24 rpm $\leq n \leq$ 40 rpm, both LSP sizes pass through the impellers with approximately the same amount of collision. Beyond $n \geq 55$ rpm, LSP_{60} experiences more frequent collisions, while LSP_{40} is still able to pass through

the impeller. For $n \leq 63$ rpm, both LSP_{40} and LSP_{60} collide more frequently with the impeller.

In Figure 4.7, the probability for the negative axial velocities in the range of $0 < |\, v_{ax,neg}| < 2.5$ m s^{-1} are displayed.

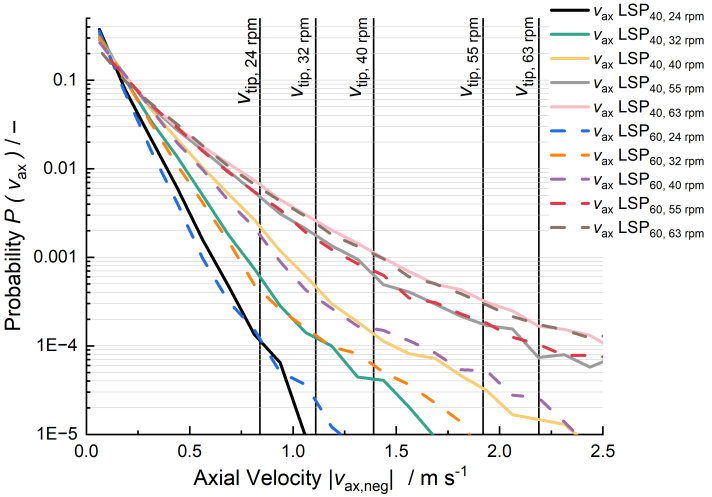

Figure 4.7: Probability of the overall negative axial velocities $|v_{ax,neg}|$ of the LSP_{40} and LSP_{60} calculated for each impeller frequency (24 rpm, 32 rpm, 40 rpm, 55 rpm, 63 rpm) using three LSP data sets within a range of 2.5 m s^{-1}. Vertical lines depict the respective tip speed. The class width is 0.0625 m s^{-1}.

The distinction between positive and negative velocities reveals only one notable difference: the point at which the probability for LSP_{60} exceeds that of LSP_{40}. In the case of negative velocities, this point aligns precisely with the impeller tip speed, indicating that

LSP_{60} collides with the impeller at all frequencies, leading to increased velocities. The LSP is pushed downwards, causing direct contact with the impeller. For an impeller frequency of $n \geq 55$ rpm, both LSP sizes collide with the impeller, as no significant difference between the probabilities is observed. Furthermore, for impeller frequencies of $n \leq 40$ rpm, the probabilities of LSP_{40} and LSP_{60} approach each other with increasing impeller frequency for velocities $\geq v_{tip}$.

In order to evaluate a velocity range smaller than 1 m s^{-1}, the observation range is adapted in the following Figure 4.8. Only the positive axial velocities $v_{ax,pos}$ are displayed, as the probabilities of $v_{ax,neg}$ exhibit a similar distribution, which is seen in the Appendix in Figure A.3.

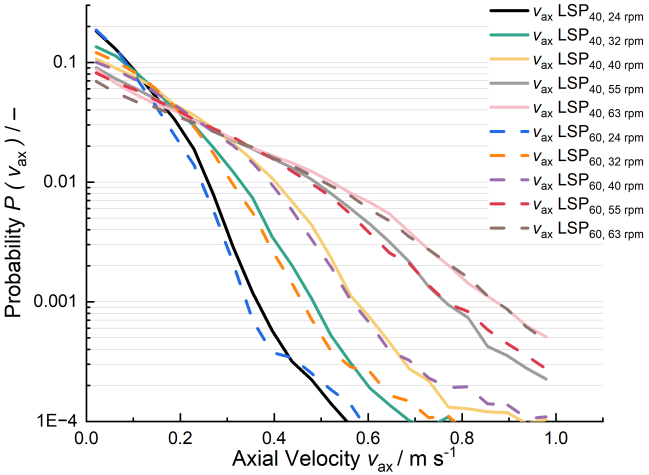

Figure 4.8: Probability of the overall positive axial velocities $v_{\mathrm{ax,pos}}$ of the LSP_{40} and LSP_{60} calculated for each impeller frequency (24 rpm, 32 rpm, 40 rpm, 55 rpm, 63 rpm), using a class width of 0.04 m s^{-1}.

The probabilities for the velocity of $v_{\mathrm{ax,pos}} \leq 0.06$ m s^{-1} decrease as the impeller frequency increases, with the highest probability occurring at 24 rpm. This suggests that lower velocities are predominantly associated with lower impeller frequencies, resulting from the lower $P\ V^{-1}$ induced into the system. For 24 rpm, for $v_{\mathrm{ax,pos}} = 0.06$ m s^{-1} a probability of 0.13 is achieved. In comparison, for the same $v_{\mathrm{ax,pos}} = 0.06$ m s^{-1}, a probability of 0.06 is reached for 63 rpm. All probability curves meet at a node point with a probability of 0.04 and a $v_{\mathrm{ax,pos}} = 0.14$ m s^{-1}.

When examining velocities exceeding 0.14 m s^{-1}, lower impeller frequencies show a reduced probability compared to higher frequen-

cies. Consequently, the probability for higher axial velocities increase with higher impeller frequencies.

In conclusion, higher impeller frequencies lead to increased positive axial velocities ($v_{\mathrm{ax,pos}}$), and the probabilities for the same $v_{\mathrm{ax,pos}}$ are higher with increased impeller frequency. This statement is valid for a $v_{\mathrm{ax,pos}}$ higher than 0.14 m s^{-1}.

Importantly from the Figure 4.6, 4.7 and 4.8, higher v_{ax} than the respective v_{tip} are measured. This is not observed in the Figure of the average axial velocities, which is due to the averaged velocities. This behavior was also observed by Hofmann et al. [Hof22].

4.4 Circulation Time

This section shows the average circulation times $\bar{t}_{\mathrm{c}}$ of the LSPs over the reactor height. The circulation times $\bar{t}_{\mathrm{c}}$ are first described for the LSP_{40}, consequently for LSP_{60} and eventually compared. Additionally, circulation time distributions on specific horizontal planes in the reactor are evaluated.

4.4.1 Average Circulation Time

For analyzing the average circulation time $\bar{t}_{\mathrm{c}}$, the reactor is divided into 42 equally distributed horizontal planes. The duration required from entering a plane until re-entering it from the same direction, forming a complete loop, is designated as one circulation loop. The weighted average for the circulation times $\bar{t}_{\mathrm{c}}$ are calculated based on the weighted average of all circulation times per plane. By graphing these, weighted average circulation times $\bar{t}_{\mathrm{c}}$ provide insights into its overall flow dynamics [Baj82]. This investigation contributes to a comprehensive understanding of the reactor's fluid behavior, and occurring compartmentalization.

In the Figure 4.9, the normalized reactor height h_{norm} is plotted on the vertical axis and the weighted average circulation time $\bar{t}_{\mathrm{c}}$ is displayed on the horizontal axis. Overall, the graph indicates that at

reactor heights of $0.15 < h_{\mathrm{norm}} \leq 0.44$, the circulation times of all impeller frequencies are in the same range, whereas above and below that height, the curves are spread over a wider range.

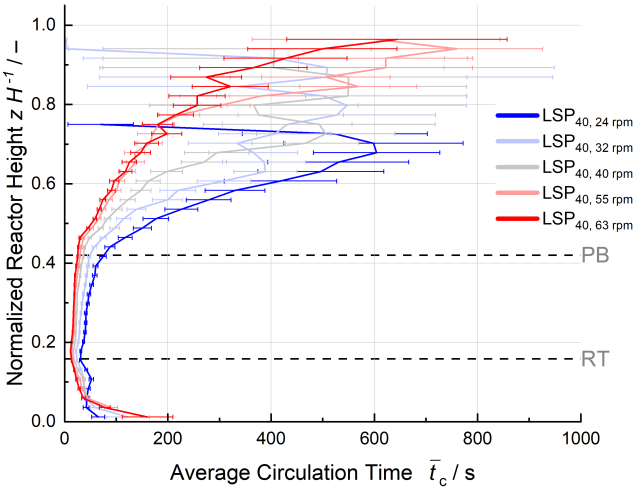

Figure 4.9: Average circulation times $\bar{t}_{\mathrm{c}}$ of LSP_{40} over the normalized reactor height (H= 4.2 m) with a vertical bin size of 0.1 m calculated for each impeller frequency (24 rpm, 32 rpm, 40 rpm, 55 rpm, 63 rpm), including the respective uncertainties. The horizontal lines represent the center of the RT and PB, respectively.

At the bottom of the reactor where $h_{\mathrm{norm}} \leq 0.01$, a circulation time $\bar{t}_{\mathrm{c}}$ could be measured for LSP_{40} at impeller frequencies of 24 rpm, 32 rpm, and 63 rpm. The observed $\bar{t}_{\mathrm{c}}$ range between 65 s $< \bar{t}_{\mathrm{c}} <$ 161 s and exhibited an increased higher standard deviation compared to the bin above, attributed to a limited dataset,

as LSP_{40} tends to infrequently visit that specific area. In the area between the reactor bottom and RT $0.01 < h_{norm} < 0.08$, it can be seen that the curves overlap stronger and have a low $\bar{t}_c$, ranging between 28 s $\leq \bar{t}_c \leq$ 46 s. From $h_{norm} = 0.06$, the $\bar{t}_c$ increases for decreasing impeller frequency. In the range between the RT and PB, $\bar{t}_c$ remain almost constant, especially for higher impeller frequencies greater than 40 rpm, whereas for lower impeller frequencies, a slight increase in the average circulation time $\bar{t}_c$ with increasing h_{norm} is observed. The circulation times range between 11 s $< \bar{t}_c <$ 17 s right above the RT and between 29 s $< \bar{t}_c <$ 74 s slightly below the PB. In the area above the PB, a wide spread and distribution of the $\bar{t}_c$ is noticed. Above $h_{norm} = 0.65$, the $\bar{t}_c$ for all impeller frequencies are in the same range, displaying high uncertainties. For all impeller frequencies, values above $h_{norm} = 0.65$ have to be treated with caution, since a comparably low data base is available in this region. The $\bar{t}_c$ for impeller frequency of 55 rpm and 63 rpm is distributed over the entire height.

The Figure 4.10 shows the average circulation times $\bar{t}_c$ for the LSP_{60} for all five impeller frequencies over h_{norm}.

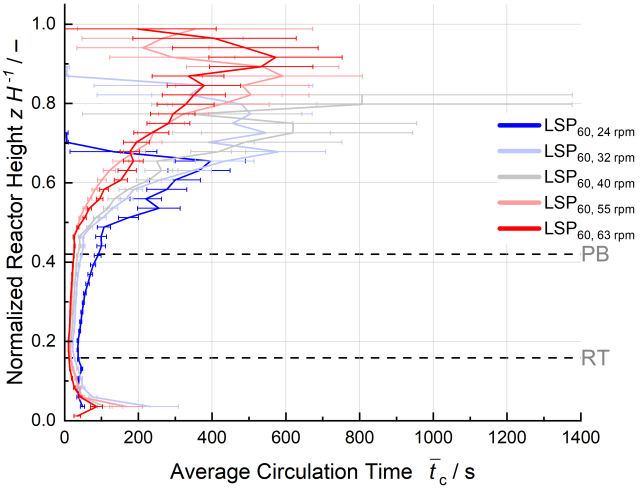

Figure 4.10: Average circulation times t_c of LSP_{60} over the normalized reactor height (H= 4.2 m) with a vertical bin size of 0.1 m, calculated for each impeller frequency (24 rpm, 32 rpm, 40 rpm, 55 rpm, 63 rpm), including the respective uncertainties. The horizontal lines represent the center of the RT and PB, respectively.

At the bottom of the reactor at $h_{norm} \leq 0.01$, contrary to the LSP_{40}, only for 63 rpm a circulation time is detected with a $\bar{t}_c = 35$ s. This results from the increased inertia of the LSP_{60}, as towards reactor walls low velocities are present. The circulation times $\bar{t}_c$ are detected at $h_{norm} \leq 0.04$ for all impeller frequencies, displaying high uncertainties, primarily due to the limited dataset available in this particular range. Generally, the circulation times $\bar{t}_c$ decrease as the impeller frequency increases. As exception, the lowest circulation time $\bar{t}_c$ below $h_{norm} \leq 0.13$ is achieved at 24 rpm. As the proba-

bility of presence already demonstrated, the LSP_{60} predominantly resides below the RT. Consequently, circulation loops are smaller, and detection planes are reached more frequently.

Similar to LSP_{40}, the circulation time $\bar{t}_c$ is equally distributed between the RT and the PB, displaying a decreased $\bar{t}_c$ with increased impeller frequency, whereas impeller frequencies greater than 40 rpm remain almost constant. The circulation times range between 10 s $< \bar{t}_c <$ 35 s at the height of the RT and between between 22 s $< \bar{t}_c <$ 89 s slightly below the PB. The similar distribution for the LSP_{40} and LSP_{60} displays intense and thorough mixing discernible based on short circulation time.

In the area above the PB, a kink in the graph is detected for the impeller frequency of 24 rpm at an $h_{norm} = 0.49$ and for the impeller frequencies $\geq$ 32 rpm at an $h_{norm} = 0.46$, which marks the upper edge of the circulation loop generated by the PB, and furthermore, defines the boundary of the middle compartment. Beyond this kink, a wider spreading of the average circulation time distribution is recognizable, indicating the upper compartment. Above $h_{norm} = 0.65$, the circulation times and uncertainties increase, which results from low data set for the respective heights. Hence, similar to the LSP_{40}, the values above $h_{norm} \approx 0.60$ have to be treated with caution. The circulation times $\bar{t}_c$ for the impeller frequencies 55 rpm and 63 rpm continue to increase above $h_{norm} = 0.75$, which are also detected at the reactor top.

The circulation times $\bar{t}c$ for both LSPs are analyzed. Below an $h_{norm} \leq 0.08$, LSP_{60} display a broader range of circulation times compared to LSP_{40}. This variance can be attributed to a generally limited data set for LSP_{60} below this height. The LSP_{60} exhibit an increased inertia, predominantly aligning with the macro-scale flow, resulting in a less frequent detection below $h_{norm} \leq 0.08$. Additionally, between the RT and PB, the respective curves are in the same range.

In the well-mixed range between RT and PB, the LSP diameter therefore has no significant influence. Above the PB, a broader distribution of the LSPs can be observed. The LSP_{60} shows a steeper increase in the circulation time compared to the LSP_{40}, which is

interpreted a less turbulent area in the reactor.

As a conclusion, both LSPs have a comparable profile of average circulation times $\bar{t}_c$ over h_{norm}. For an increased impeller frequency, a reduced average circulation time $\bar{t}_c$ is detected, which is also observed by Hofmann et al. [Hof24]. This is observed for both LSP sizes in the range of $0.13 \leq h_{norm} \leq 0.63$. The lowest circulation times are stated in Table 4.3.

Table 4.3: Minimal average circulation time $\bar{t}_{c,min}$ with a respective uncertainty $\Delta\ \bar{t}_{c,min}$ at detected normalized reactor heights.

	Stirring frequency n /rpm				
	24	**32**	**40**	**55**	**63**
LSP_{40} $\bar{t}_{c,min}$ /s	30.8	22.2	16.9	13.3	11.7
LSP_{40} $\Delta\ \bar{t}_{c,min}$ /s	1.8	1.2	0.7	0.7	0.6
LSP_{40} h_{norm}/-	0.15	0.18	0.18	0.18	0.18
LSP_{60} $\bar{t}_{c,min}$ /s	35.8	22.1	16.2	13.3	10.3
LSP_{60} $\Delta\ \bar{t}_{c,min}$ /s	2.0	1.0	0.8	0.6	0.5
LSP_{60} h_{norm}/-	0.18	0.18	0.18	0.20	0.20

The Table 4.3 illustrates that there is no significant difference observed for all rpm cases but 24 rpm for the minimal average circulation time. The position of the minimum average circulation time is determined above the RT, marking the turn-over point for the circulation loop, as stated by Reinecke [Rei14]. This observation is consistent with the results obtained from analyzing the average velocity, where a maximum velocity is identified at this particular height. However, it is essential to acknowledge the existence of at least three distinct circulation loops in this reactor.

For $h_{norm} \leq 0.06$, the LSPs exhibit increased circulation times and uncertainties due to a lower number of data points. In general, it can be stated that the circulation times $\bar{t}_c$ increase towards the bottom of the reactor, resulting from lower vortex presence and decreased macro-

scale flow. Furthermore, the circulation times generally decrease with increasing impeller frequencies, except for the case of 24 rpm. Both LSP_{40} and LSP_{60} exhibit the shortest circulation time below the RT at $h_{norm} \leq 0.06$ and $h_{norm} \leq 0.13$, respectively. Moreover, for both LSPs at 24 rpm, a peak is detected at $h_{norm} = 0.11$. A possible explanation for the increased $\bar{t}_c$ at this level might be that at this position, the vortex by the RT changes into a radial and tangential movement. As the circulation times below and above $h_{norm} \leq 0.11$ decrease, this height could also be considered a barrier for lower impeller frequencies, as the LSPs predominantly stay at $h_{norm} \leq 0.08$

In the area above $h_{norm} = 0.63$ the circulation times of all impeller frequencies are in the same range for both LSP sizes, as low data points are observed for all impeller frequencies, indicating a decreased presence in this area.

The overall weighted average circulation time $\bar{t}_{c,overall}$ is displayed in Table 4.4, with the LSP_{60} consisting of a slightly decreased $\bar{t}_{c,overall}$ compared to the LSP_{40}. The higher inertia of LSP_{60} leads it to consistently trace the same loop more frequently and demonstrates the ability of following macro-scale flow. In contrast, LSP_{40} is presumed to have the capacity to follow macro- and meso-scale flows.

Table 4.4: Total average circulation time $\bar{t}_{c,overall}$ with a respective uncertainty $\Delta\ \bar{t}_{c,overall}$.

	Stirring frequency n /rpm				
	24	**32**	**40**	**55**	**63**
LSP_{40} $\bar{t}_{c,overall}$ /s	63.1	52.9	40.5	39.2	34.9
LSP_{40} $\Delta\ \bar{t}_{c,overall}$ /s	1.4	1.2	0.7	0.7	0.7
LSP_{60} $\bar{t}_{c,overall}$ /s	59.0	50.7	37.0	32.7	30.3
LSP_{60} $\Delta\ \bar{t}_{c,overall}$ /s	1.3	1.1	0.8	0.7	0.6

Overall, three compartments are detected within the reactor for

both LSP_{40} and LSP_{60} at all impeller frequencies. The bottom compartment is located between $0 \leq h_{\text{norm}} \leq 0.08$, which separates the bottom peak from the middle compartment. In this compartment, medium-length average circulation times are observed. The middle compartment ranges between $0.08 < h_{\text{norm}} \leq 0.53$, and is characterized by short circulation times. Hence, an overall sufficient mixing is achieved and the compartment consists of high velocities and pronounced turbulent flows on macro-scale. The upper compartment $0.53 < h_{\text{norm}} \leq 1$ is characterized by its high circulation times, which result from an insufficient mixing with a low probability of presence. As a conclusion for the compartments, regarding the circulation time, it can be assumed that a lower circulation time results from a more turbulent and sufficient mixing in the regime. Consequently, indicating a predominantly macro-scale flow, whereas in compartments with higher circulation times, insufficient mixing is observed.

The $\bar{t}_c$ is investigated by Hofmann et al. [Hof24] utilizing three axial impellers. Similarly, three compartments are observed.

When comparing the minimal circulation times for this impeller configuration with the three EE configuration in Hofmann et al. [Hof24] using the same $P\ V^{-1}$ input, it is expected to achieve increased circulation times for EE configuration, as the RT and PB combination display increased vortex formation at the RT and therefore smaller circulation loops. In this study, at least three circulation loops exists, indicating that the circulation loop above the RT consists of the strongest flow. In this flow, the axial stream originated by the PB unites with the upper circulation loops of the RT, resulting in an increased velocity and consequently lower circulation times. The circulation loop of the EE is assumed to have a greater distance as it flows from bottom to the upper compartment, resulting in one large circulation loop. This can be confirmed, as the average circulation times of the PB and RT configurations are shorter compared to the EE configuration. However, the differences between the minimal circulation times are relatively small, with variances of 2 to 5 seconds. This is a result of faster velocities in the EE configuration, where the

maximum velocity is 1.3 to 1.6 times higher than in the PB-RT configuration. Additionally, eddies in the vicinity of the EE contribute to a decreased circulation loop. Moreover, the distribution of average circulation time $\bar{t}_c$ is comparable, implying that especially in highly turbulent regions, the configurations are indistinguishable, leading to the generation of similar compartments.

4.4.2 Circulation Time Distribution

The Circulation Time Distribution (CTD) represents the distribution of all measured circulation times on a specific horizontal plane. Three planes are chosen for CTD evaluation: the first one just below the RT at an $h_{\text{norm}} = 0.13$, the second one right above the RT at $h_{\text{norm}} = 0.19$, and the third one below the PB at $h_{\text{norm}} = 0.37$, which can be seen in Figure 4.11.

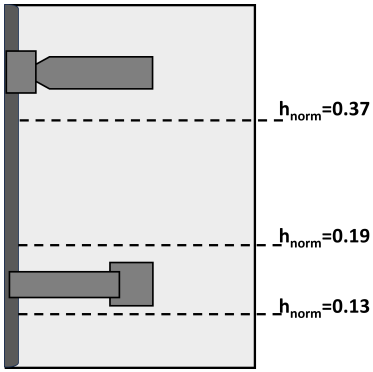

Figure 4.11: Schematic illustration of the specific planes analyzed within the reactor.

Six figures are presented, featuring two for each plane. They illustrate the CTD for both the LSP_{40} (left) and LSP_{60} (right) at the impeller frequency of 63 rpm, demonstrating the three selected

experiments: 10, 11, and 17. The vertical axis displays the probability, while the horizontal axis represents the circulation time in seconds. The probabilities from all three experiments are stacked behind each other in the figures.

Beginning with the specific plane at $h_{\mathrm{norm}} = 0.13$, the Figure 4.12 (left) displays the LSP_{40} and the Figure 4.12 (right) displays the LSP_{60}. The probability for lower circulation times exhibits a peak that diminishes towards higher circulation times. Figure 4.12 clearly illustrates the log-normal distribution of the circulation time as already described by Bisgaard et al. [Bis21], Hofmann et al. [Hof24], and Reinecke [Rei14].

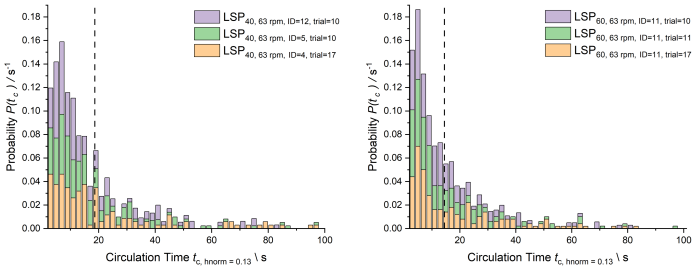

Figure 4.12: Circulation Time Distribution (CTD) is plotted for LSP_{40} (left) and LSP_{60} (right) at $h_{\mathrm{norm}} = 0.13$, using 50 bins and a class width of 2 s. The data correspond both to 63 rpm. The weighted average $\bar{t}_{\mathrm{c}}$ is represented by a dashed line.

In the Figure 4.13 the CTD for h_{norm}=0.19 is shown. Similar as in the Figure 4.13, a peak for the lower circulation times is detected with a decline towards higher circulation times. Additionally, a second peak is recognized. Thus, a bimodal distribution is observed above the RT, indicating that two circulation loops are detected at this height.

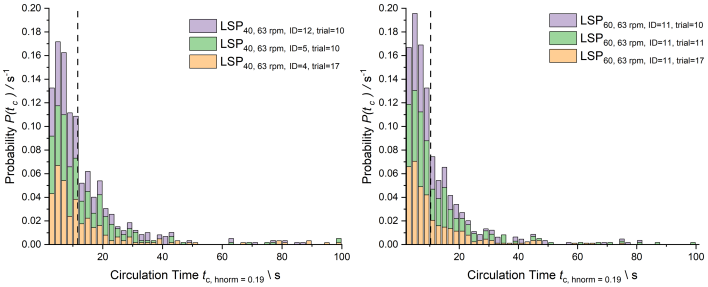

Figure 4.13: Circulation Time Distribution (CTD) is plotted for LSP_{40} (left) and LSP_{60} (right) at h_{norm}=0.19, using 50 bins and a class width of 2 s. The data correspond both to 63 rpm. The weighted average $\bar{t}_c$ is represented by a dashed line.

In the Figure 4.14, the CTD for $h_{norm} = 0.37$ is shown. In contrast to Figures 4.12 and 4.13, three peaks are observable. For the LSP_{40}, one peak is located at low circulation times below $t_c < 20$ s, the second peak is located between 20 s $< t_c <$ 30 s, and the third peak is located between 40 s $< t_c <$ 60 s. Whereas for the LSP_{60}, the first peak is detected below $t_c < 25$ s, the second peak is detected between 25 s $< t_c <$ 35 s, and the third peak is located between 35 s $< t_c <$ 60 s. The CTD for $h_{norm} = 0.37$ is characterized as a trimodal distribution.

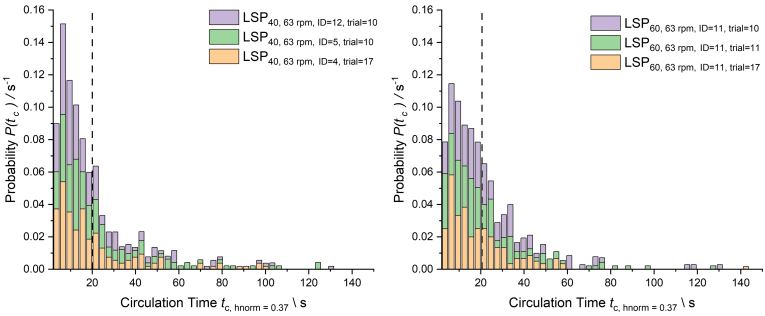

Figure 4.14: Circulation Time Distribution (CTD) is plotted for LSP_{40} (left) and LSP_{60} (right) at h_{norm}=0.37, using 50 bins and a class width of 3 s. The data correspond both to 63 rpm. The weighted average $\bar{t}_{\mathrm{c}}$ is represented by a dashed line.

The selection of these three specific planes is chosen by the intention to observe the vicinity of the impeller closely without directly aligning the circulation plane with the impeller height.

When examining the Circulation Time Distribution (CTD) for $h_{\mathrm{norm}} = 0.13$, the observed log-normal distribution characterizes the lower circulation loop of the RT (Figure 4.15 (left)). This log-normal distribution signifies that circulation times are centered around a peak, with the probability decreasing for higher circulation times. Hence, the majority of runs through the same circulation loop exhibit a similar circulation time. The log-normal distribution aligns with results detected by Hofmann et al. [Hof24], Bisgaard et al [Bis21], Reinecke [Rei14], and more [Oos85, van87, Vrá00].

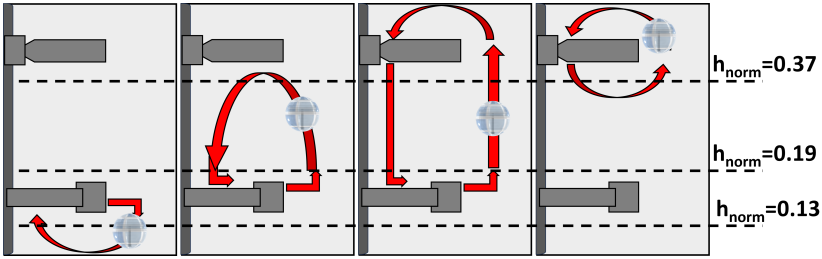

Figure 4.15: Schematic illustration of the four main circulation loops measured in the reactor.

For $h_{\text{norm}} = 0.19$, a bimodal distribution is detected. In Bisgaard et al.'s publication, no bimodal distribution is observed, as the reactor investigated is equipped with one RT. Hence, the bimodal distribution displayed in the CTD in this thesis results from two circulation loops, resulting from the upper circulation loop (Figure 4.15 (center left)) of the RT and the loop generated by the PB (Figure 4.15 (center right)). Placing the circulation plane precisely at the RT yielded no clear distribution. This results from the fact that the LSP hovers on the defined plane and is repeatedly detected slightly above and below the plane, creating a movement on the plane that is perceived as circulation, as the pressure sensor solely measures axial positions. Representing circulation times at the center of the RT is therefore not recommended due to the radial movement of the LSP at the height of the RT.

For the CTD at $h_{\text{norm}} = 0.37$, below the PB a trimodal distribution can be obtained. This area is chosen since in the average velocity profile, an increase in velocities is detected at this point.

For $h_{\text{norm}} = 0.37$ (Figure 4.14), the first peak is associated with the upper circulation loop of the RT (Figure 4.15 (center left)), demonstrating high velocities and low average circulation times. The second peak and the third peak represent either the large axial loop (Figure 4.15 (center right)) or the smaller axial loop (Figure 4.15 (right)).

In conclusion, each peak in the CTD signifies a circulation loop.

Below the RT, one circulation loop is present (Figure 4.12) Slightly above the RT, two circulation loops are demonstrated (Figure 4.13), and below the PB, in total three circulation loops are detected (Figure 4.14). Consequently, this assumption leads to a total of four circulation loops when considering both the loops of the RT and those of the PB.

For further clarification, radial positions could be considered, and an expanded database is essential, especially for both loops generated by the PB, to enhance the validity of the findings.

4.5 Lagrangian Regime Analysis

This section examines the Lagrangian regime analysis, which describes the probability of the LSPs remaining within specific compartments for a given period of time. The compartment boundaries are determined visually in advance based on the distribution of the average circulation times. Three distinct compartments are identified, categorized as the top, middle, and bottom compartments. The compartment boundaries are set to $h_{\text{norm}} = 0.08$ and $h_{\text{norm}} = 0.53$ (Figure 4.16), providing general demarcations, as compartments do not possess precise boundaries.

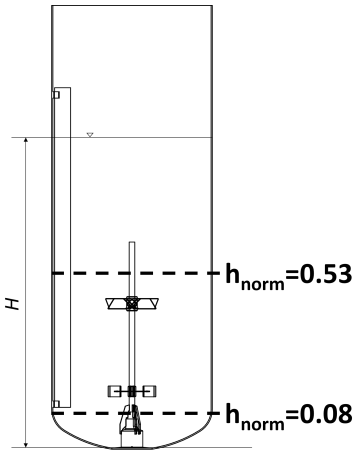

Figure 4.16: Schematic illustration of the compartment boundaries within the reactor.

In this section, the compartment regimes of both, LSP_{40} and LSP_{60}, are presented for the two impeller frequencies 40 rpm and 63 rpm. The LSP_{40} is displayed with a round symbol and the LSP_{60} with a square symbol. The top compartment is represented by the color pink, the middle compartment by the color blue, and the bottom compartment by the color green. The residence time t_{res} per hydrodynamic regime is plotted on the horizontal axis and the probability on the vertical axis, describing the likelihood of an LSP remaining within a compartment for a specific time period t_{res}.

In the Figure 4.17, the probabilities of the LSP_{40} and LSP_{60} at the impeller frequency of 40 rpm are displayed. Notably, the probabilities for LSP_{40} and LSP_{60} are in the same range for the compartments, indicating similar behavior.

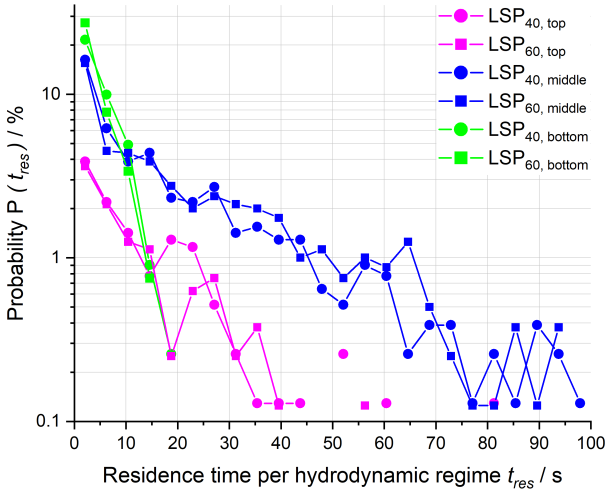

Figure 4.17: Lagrangian regime analysis for impeller frequency of 40 rpm, using 25 bins and a class width of 4 s. The compartments are defined as top, middle, and bottom compartments, with selected boundaries of $h_{\text{norm}} \in \{0.08, 0.53\}$.

The Figure 4.17 reveals that low residence times in the hydrodynamic regimes are predominantly observed in the bottom and middle compartments. The probabilities of the bottom compartment decrease more steeply, suggesting shorter residence times for LSP_{40} and LSP_{60} in this compartment, eventually ending up in the middle compartment. Although the middle compartment also displays a high probability of low residence times, it also shows larger residence times, which in turn suggests that there are circulation loops below the PB, which do mix up with the radial circulation loop generated by the RT, keeping the LSP in a loop between the PB and RT.

It is evident that the top compartment displays a notably low probability smaller than 3.7 % for short residence times for both LSP sizes. For residence time $t_{res} > 15$ s, the probability decreases below a probability of approximately 1.0 %, and for $t_{res} > 30$ s, a probability of 0.1 % is displayed. This is attributed to insufficient mixing at the reactor top, resulting in a reduced macro-scale flow. When the LSPs entered the top compartment, a floating and slow drifting was observed in the experiments.

There is no significant distinction of the residence times between the LSP sizes for the bottom compartment, implying a similar distribution within the compartment. However, a 5.7 % higher probability for low residence time $t_{res} < 5$ s is observed for the LSP_{60} compared to LSP_{40}. The low probabilities can be attributed to a slightly smaller radius of the circulation loop for LSP_{60} at 40 rpm, causing it to remain at slightly higher levels and resulting in shorter residence times for the bottom compartment.

The Figure 4.18 shows the residence time per hydrodynamic regime for both LSP_{40} and LSP_{60} at the maximum impeller frequency of 63 rpm. The residence profile exhibits a distribution similar to the impeller frequency of 40 rpm. However, a stronger overlap between the probability curves of LSP_{40} and LSP_{60} are observed.

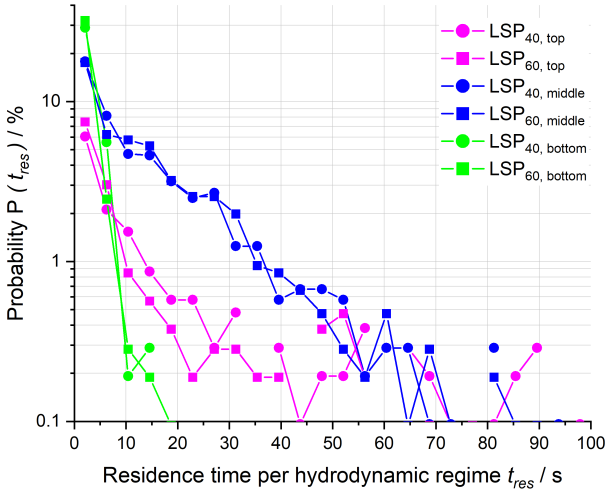

Figure 4.18: Lagrangian regime analysis for impeller frequency of 63 rpm, using 25 bins and a class width of 4 s. The compartments are defined as top, middle, and bottom compartments, with selected boundaries of $h_{\mathrm{norm}} = \in\{0.08, 0.53\}$.

When comparing the bottom compartment at the impeller frequencies 40 rpm and 63 rpm, the probability of shorter residence times increases from 21.6 % to 29.0 % for the LSP_{40}, and from 27.3 % to 32.1 % for the LSP_{60}, respectively. Additionally, in the bottom compartment for both sizes, a slight shift of the probability for longer residence times is observed compared to the impeller frequency of 40 rpm. This could be attributed to the LSP following an increased radius on the lower circulation loop of the RT, influenced by the enhanced flow on the macro-scale. Similar trends are observed in the top compartment, as the probability shifts towards longer residence

times. This shift is attributed to the LSP flowing towards higher heights as turbulence increases. In the top compartment, where less macro-scale flow is present, there is an increased time period until reentering the middle compartment. Notably, the middle compartment shows no pronounced alteration for shorter residence times at both low and high impeller frequencies. For the middle compartment, the probability for the residence time < 4 s is approximately about 15.5 % at 40 rpm, and 17.5 % at 63 rpm for both LSP sizes. Consequently, the region between the impellers is considered as highly turbulent on macro-scale.

The probability of the total residence time is listed for the two different impeller frequencies for the LSP_{40} and LSP_{60} in Table 4.5, including the top, middle and bottom compartment.

Table 4.5: Summarized percentage of the total probabilities for the Lagrangian regime, categorized into top, middle, and bottom compartments.

		Compartments		
		Top	Middle	Bottom
40 rpm	LSP_{40} $P(t_{res})$ / %	12.4	48.7	37.6
	LSP_{60} $P(t_{res})$ / %	10.7	49.3	39.2
63 rpm	LSP_{40} $P(t_{res})$ / %	14.9	50.0	35.1
	LSP_{60} $P(t_{res})$ / %	14.7	49.9	35.1

As the impeller frequency increases, the middle compartment shows no significant variation in the probability for both LSPs. In contrast, the probability for LSP_{40} and LSP_{60} in the bottom compartment decreases by approximately 2.5 % and 4.0 %, while the top compartment increases of approximately 2.5 % and 4.0 %, respectively.

In summary, the compartments exhibit less effective mixing at low impeller frequencies, as evidenced by the increased residence time in the bottom compartment. As the impeller frequency increases, a shift in the mixing regime towards the less-mixed top compartment

is observed.

Furthermore, a reduction in the probability of short residence times is observed for the LSPs in both the bottom and top compartments at lower impeller speeds. This diminishing trend aligns with the characteristic exponential decay of recirculation flow, as previously demonstrated by Haringa et al. [Har18]. With increasing impeller frequency, the probabilities for both LSP sizes converge in each compartment, indicating that macro-scale flow predominates over micro-scale flow. With regard to the compartments, short residence times are particularly observed in the bottom compartment, whereas a low probability for all residence times are measured in the top compartment. Notably, the middle compartment displays the widest range between short and long residence times.

When comparing single-phase hydrodynamic regimes with existing publications, Hofmann et al.'s work aligns with this study, in which experiments within a 15,000 L reactor with three EE were conducted [Hof24]. The compartment boundaries are set differently, as the EE exhibits a unique flow pattern. Therefore, only the trends of the probability for the overall residence times can be compared. The boundaries of the middle compartment are set to cover a larger area for the EE, as the primarily axial flow results in an expanded circulation loop. In contrast, the PB and RT are characterized by forming smaller circulation loops due to the radial flow of the RT combining with the axial flow of the PB, thus, a decreased area for the middle compartment is applied in this study. In Hofmann et al. [Hof24], similar to this study, it was observed, that the LSPs were preferentially located within the middle compartment. Additionally, the bottom compartment showed an elevated probability of shorter residence times, with an overlap in the probabilities of the bottom and top regimes. At higher impeller frequency, the probabilities for the bottom compartment declined more strongly and the total percentage of the probability for the top compartment increased. Hence, even with a different impeller setup and different compartment boundaries, the compartments exhibit similar mixing behavior with increasing impeller frequencies.

4.6 Mixing Time Correlations

In Figure 4.19 the overall circulation time $\bar{t}_{c,overall}$ for the LSP_{40} and the LSP_{60} are displayed. Furthermore, the global mixing time $t_{mix,global,95}$ and $\bar{t}_{c,overall}$ for the EE by Hofmann et al. [Hof24] and the mixing time $t_{mix,global,95}$ for the PB-RT combination by Rosseburg et al. [Ros18] is integrated into the Figure 4.19.

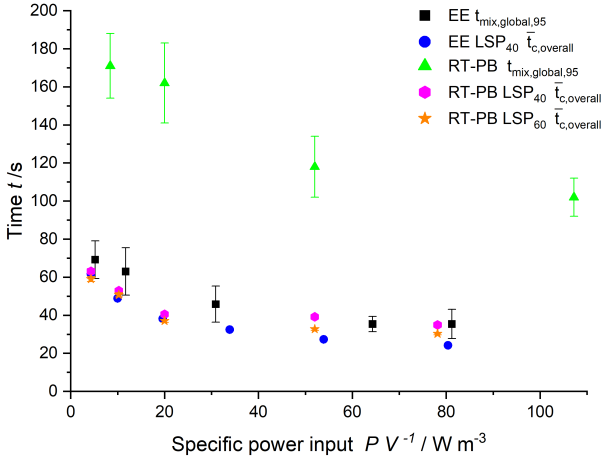

Figure 4.19: Measured overall circulation time $\bar{t}_{c,overall}$ of LSP_{40} and LSP_{60} as a function of the specific $P\ V^{-1}$ input. The mixing time $t_{mix,global,95}$ and $\bar{t}_{c,overall}$ for the EE by Hofmann et al. [Hof24] and the mixing time $t_{mix,global,95}$ for the PB-RT by Rosseburg et al. [Ros18] are integrated.

All data (Table 4.6) are obtained in the same reactor. The uncertainties and standard deviations are plotted with the corresponding data.

Table 4.6: Global mixing time $t_{\mathrm{mix,global,95}}$ and overall circulation time $t_{\mathrm{c,overall}}$ with their respective $P\ V^{-1}$ input for the EE and the RT-PB setup, with respective uncertainities Δ.

EE						
$P\ V^{-1}$ / W m^{-3}	5.2	11.7		30.9	64.3	81.2
n / rpm	16	21		29	37	40
$t_{\mathrm{mix,global,95}}$ / s	69.2	63.0		45.8	35.4	35.4
$\Delta\ t_{\mathrm{mix,global,95}}$ / s	9.9	12.5		9.5	4.0	7.4
$P\ V^{-1}$ / W m^{-3}	4.3	10.0	19.6	33.9	53.9	80.4
n /rpm	15	20	25	30	35	40
LSP$_{40}$ t_{c} / s	61.8	48.9	38.2	32.4	27.3	24.2
LSP$_{40}$ $\Delta\ t_{\mathrm{c}}$ / s	0.9	0.7	0.4	0.4	0.3	0.2
RT-PB						
$P\ V^{-1}$ / W m^{-3}		8.4	20.0		52.0	107.2
n / rpm		30	40		55	70
$t_{\mathrm{mix,global,95}}$ / s		171.0	162.0		118.0	102.0
$\Delta\ t_{\mathrm{mix,global,95}}$ / s		17.0	21.0		16.0	10.0
$P\ V^{-1}$ / W m^{-3}	4.3	10.2	20.0		52.0	78.1
n / rpm	24	32	40		55	63
LSP$_{40}$ t_{c} / s	63.1	52.9	40.5		39.2	34.9
LSP$_{40}$ $\Delta\ t_{\mathrm{c}}$ / s	1.4	1.2	0.7		0.7	0.7
LSP$_{60}$ t_{c} / s	59.0	50.7	37.0		32.7	30.3
LSP$_{60}$ $\Delta\ t_{\mathrm{c}}$ / s	1.3	1.1	0.8		0.7	0.6

The Figure 4.19 shows a decreasing trend with increasing $P\,V^{-1}$ input of $\bar{t}_{\mathrm{c,overall}}$ and the mixing times $t_{\mathrm{mix,global,95}}$. The ratio of $t_{\mathrm{mix,global,95}}$ to $\bar{t}_{\mathrm{c,overall}}$ results in 3 to 4 for both LSP sizes. Furthermore, a slightly decreased overall circulation time $\bar{t}_{\mathrm{c,overall}}$ is observed for the LSP_{60} compared to the LSP_{40}. Importantly, this does not result from a faster circulation, as seen from the axial velocities since similar ranges are observed for both LSP sizes. Thus, the slightly reduced circulation time for LSP_{60} can be traced back to following a shorter overall circulation loop. It is further assumed that with increasing LSP diameter, the $\bar{t}_{\mathrm{c,overall}}$ decreases, as the possible eddy sizes to be followed decreases, reducing the possible length of the circulation loop due to its comparably higher moment of inertia. Whereas decreasing the LSP diameter increases the circulation time, as the circulation loop length or possible loops increases. Moreover, it is observed that the mixing times $t_{\mathrm{mix,global,95}}$ and the $\bar{t}_{\mathrm{c,overall}}$ for the EE from the publication of Hofmann et al. [Hof24] show similar values to the $\bar{t}_{\mathrm{c,overall}}$ of the LSP_{40} and the LSP_{60}. As the EE impeller generates one total axial flow loop due to the axial pumping impellers, the ratio of the $t_{\mathrm{mix,global,95}}$ to the $\bar{t}_{\mathrm{c,overall}}$ is observed as 1. Whereas, the RT and PB combination exhibits at least three to four circulation loops, resulting from two oppositely directed vortices generated by the RT and one main axial loop from the PB. The fourth loop is a bypass stream generated by the PB, flowing directly back to the PB. According to literature [Hol64, Kha76] a ratio of 3 to 5 is expected for the RT. However, Bisgaard et al. [Bis21] observed a ratio of 2.6 for the RT and 2.2 for the PB. This indicates a lower ratio for the RT compared to literature expectations. Based on the findings of this study, an increased reactor volume would further decrease the ratios, with an expected ratio of 2 for the RT and 1 for the PB. This is assumed, as the ratios in this study and Hofmann et al. correlate with the quantity of circulation loops, with a reactor volume 10-fold bigger than the reactor used in Bisgaard's et al. study for a similar LSP size.

As a summary, both LSPs result in a $t_{\mathrm{mix,global,95}}$ to $\bar{t}_{\mathrm{c,overall}}$ ratio of 3 to 4, indicating the amount of circulation loops within the reactor

until it is homogeneously mixed on the macro-scale. An increased reactor volume, or a decrease of the LSP diameter increases the $\bar{t}_{c,overall}$ further, subsequently reducing the ratio of $t_{mix,global,95}$ to $\bar{t}_{c,overall}$.

4.7 Error Discussion

The results presented in the previous section require careful observation due to potential factors influencing the LSP, thus affecting the data points. In the following section, possible errors occurring during the experiments and as a result of data processing are discussed.

4.7.1 Experimental Errors

Tilting Movements

During the experiments, primarily tilting movements were particularly observed in the LSP_{60}. This phenomenon is caused by a combination of two weight distributions, one centered along the middle axis and the other resulting from an overweight in one shell. The centered weight is a consequence of the pressure sensor positioned along the middle axis and the brass rings around the M4-rod on the middle axis. The weight distribution towards a shell is caused by a relatively low weight on one shell, where the pressure sensor is integrated, and a heavy weight on the other shell due to the brass rings. This creates an imbalance that places a greater load on the latter shell.

The overall weight distribution causes the pressure sensor to consistently face upwards. When pushed aside, either by the liquid or the impellers, tilting movements around the heavily weighted center occurred, and a rolling over of the LSP_{60} was barely observed, even at higher impeller frequencies. In contrast, the LSP_{40} displayed no identifiable center and exhibited rollovers, while the tilting movements of the LSP_{60} resulted in energy loss due to friction, impacting its ability to maintain alignment with the same flow stream.

Temperature

The reactor temperature and the temperature of the water bath for density calibration were set to 22°C. However, despite the laboratory's temperature being considered relatively constant, colder values of around 20°C were observed. When the LSPs were sealed, the enclosed air matched the laboratory's temperature. During the density calibration of the LSPs, the temperature within the LSP could not adapt to the water bath temperature as fast as the calibration process occurred. Throughout the experiments, the temperature within the LSP gradually increased matching the reactor's temperature, leading to a distinct change in the temperature within the LSP during the experiments. This change increased the pressure within the LSP, potentially causing a slight opening of the shells and achieving an decreased density.

Density Calibration

The density calibration exhibited an average range of $\Delta\rho = 1.6\ \mathrm{kg\ m^{-3}}$ in which the LSP was adjusted. Slight differences in densities among the LSPs may have resulted in varying flow-following behaviors due to differences in buoyancy.

Furthermore, when the LSPs were closed, air bubbles tended to attach to the shell sealing area. Although shaking the LSPs proved to be highly effective in removing these bubbles from the shells, there was a probability of new bubble attachment when positioned on the upper reactor wall for calibration. In this case, new bubbles could become trapped within the sealed LSP, leading to a decreased density.

Singularity of Particle

In the initial two experiments with the LSP_{60}, two units were investigated. However, due to an error, only one of the LSP_{60} units was utilized in the following experiments. This highlights an issue with the reliability of the LSP_{60} sensor device, as the same ID is

consistently applied, making it challenging to immediately identify occurrences of errors. The validation method for the pressure data relies on comparing them to those obtained from the LSP_{40}.

Data Basis in the Top Compartment

The diagrams reveal noticeable fluctuations, particularly in the top compartment. In this regime of high fluctuations, a low number of data points are available, and thus, data values deviating from the average have a stronger impact on the distribution compared to compartments with high data points. Consequently, the distribution for the top compartments should be regarded more as tendencies rather than precise representations.

4.7.2 Data Processing Errors

Bin Selection

When categorizing data points into bins, the chosen bin size can impact averages values or probabilities. Differences between the LSP_{40} and LSP_{60} may not always be as strongly detected as the actual values suggest. Furthermore, in this study, a pressure frequency of 50 Hz is used, which shows the potential to reduce the bin size.

Compartment Boundaries

The compartment boundary was determined by the distribution of the average circulation times $\bar{t}_c$. As the compartments do not possess precise boundaries, it is challenging to determine accurate locations for the boundaries. Since the Lagrangian Regime Analysis relies on these compartment boundaries, the probabilities might differ slightly when adjusting them.

5 Conclusion

This study investigates the two Lagrangian Sensor Particle (LSP) sizes of 40 mm (LSP_{40}) and 60 mm (LSP_{60}) in diameter. Both LSPs are equipped with a pressure sensor. This thesis addresses three key aspects: the hydrodynamic characterization of a single-phase 15,000 L bioreactor with a pitched blade impeller (PB) and Rushton Turbine (RT) setup at five impeller frequencies n $\in\{24, 32, 40, 55, 63\}$rpm, the comparison of two LSP sizes regarding their flow-following behavior, and the determination of differently mixed regimes within the reactor, known as compartments.

The LSPs are designed with Inventor (Autodesk). The collected data from the pressure sensor is stored on a hard drive. For calculation purpose and due to extensive data sets, a Python™ script is developed. First the data is pre-processed, which includes smoothing with a low-pass filter, interpolating, and the selection of the data sets for further evaluation. Subsequently, the Stokes number, the axial height, the probability of presence, the velocity, and the circulation time are calculated and a Lagrangian regime analysis is conducted. Additionally, the overall circulation times of both LSPs are compared to global mixing times in the same setup. The results are plotted for both LSP sizes.

The estimated Stokes numbers are ranging from $0.002 < St < 0.004$ for the macro-scale, $0.21 < St < 0.32$ for the meso-scale, and $2.9 < St < 7.1$ for the micro-scale. For the probability of presence, in total four peaks are observed, which are located below the RT, right above the RT, below the PB and right above the PB for both LSP sizes, except for the impeller frequency of 24 rpm. The peak below the PB is understood as an area of probability increment rather than a distinct peak. For the average velocities, a symmetry

between positive and negative axial velocities is observed, with two distinctive peaks, one above the RT and one below the PB. Notably, the maximal axial velocities are in a same range for both LSP sizes. The velocities increase with increasing impeller frequency. For the circulation times, an area with comparably low circulation times between the PB and RT is observed. Furthermore, the minimum circulation time, which displays the turn-over point of the circulation loop, is for both LSP sizes observed at an h_{norm}=0.20 ranging between the same values. The CTD is analyzed on three specific heights, which are below the RT, above the RT and below the PB. The CTD for the height below and above the RT exhibits a log-normal and a bimodal distribution, respectively, whereas for the height below the PB, a trimodal distribution is observed. For the Lagrangian Regime Analysis, three compartments are investigated. The overall circulation time is plotted with the global mixing, exhibiting a ratio of the examined global mixing time to overall circulation time between 3 and 4.

The estimated Stokes number for the LSP_{40} and LSP_{60} exhibit comparable values, as reported in the publications of Hofmann et al [Hof24], Reinecke [Rei14] and Bisgaard et al. [Bis21]. Since the Stokes number ranges between 0.002 and 0.004 for the macro-scale, a flow-following behavior is assumed as it results in $St \ll 1$. An increased inertia of the LSP_{60} compared to the LSP_{40} is experimentally observed in the probability of presence and the Lagrangian velocity analysis. In the probability of presence, the LSP_{60} display a greater probability for the height right above the RT and a barely noticeable probability for the height below the RT at impeller frequencies of 55 rpm and 63 rpm, whereas, for the LSP_{40} at same impeller frequencies, an equal probability of presence below and over the RT is observed. The heightened probability observed in LSP_{60} stems from its increased inertia, as it consistently remains within the same loop. Furthermore, the overall circulation times of LSP_{60} are up to 1.4 times lower than those of LSP_{40}. As LSP_{60} exhibit velocities in the same range as the LSP_{40}, this indicates that LSP_{60} follow shorter circulation loops.

Four circulation loops within the reactor are estimated, as seen

in the CTD displaying a trimodal distribution for the horizontal plane below the PB. The ratio of the examined global mixing time to overall circulation time is between 3 and 4, which agrees with findings according to literature. The log-normal CTD observed below the RT results from one circulation loop and the bimodal distribution above the RT from two circulation loops. Whereas, the trimodal CTD indicates three circulation loops influencing this height. Furthermore, the four peaks of the probability of presence result from radial movements of the circulation loop. The height above the RT represents the turn-over point of the main loop, as a minimum circulation time and a high axial velocity is reached. Assuming that this turn-over point indicates the strongest circulation loop, which combines the upper circulation loop of the RT with the loop generated by the PB, as underlined by the result of the maximum average velocity at this height.

Circulation time results reveal three compartments within the reactor, which boundaries are assumed above the PB at $h_{\mathrm{norm}} = 0.53$ and below the RT at $h_{\mathrm{norm}} = 0.08$. According to these results, the Lagrangian regime analysis shows that the middle compartment exhibits a broad residence time distribution. In contrast, the top and bottom compartment show less probability for higher residence times. Below the RT and above the PB, the circulation times increased, with the top compartment displaying the highest circulation time. In conjunction with the probability of presence, the top compartment indicates low mixing behavior, since LSPs rarely enter the top compartment and when entered, long circulation times occur.

To summarize, both LSP sizes exhibit similar behavior, regarding velocities and circulation times. Nevertheless, the LSP_{40} exhibits a better flow-following behavior, as it tends to follow also meso-scale vortices, whereas the LSP_{60} is more influenced by inertia. The RT and PB combination reveal four circulation loops, involving two loops generated by the RT and one loop originating from the PB, assumed to split into two separate loops. In total three compartments are detected with one turbulent compartment being between the RT and PB, one bottom compartment and one top compartment. All data

are gathered from the pressure data within the LSP, demonstrating the adaptability for industrial processes to achieve an insight of the reactor mixing processes without visual observation necessary.

6 Outlook

For future investigation, the design of a further increased diameter, such as 80 mm or 90 mm, should be considered. Ideally the experiments should be conducted within a reactor exceeding 15,000 L. By using an increased diameter, further sensors may be integrated, providing a richer data set concerning the mixing process, leading to a better insight into the reactor. For this purpose, the implementation of a Dissolved Oxygen (DO) sensor might exhibit new information about the overall aeration process, which until now, is detected by a fixed sensor integrated into the reactor wall. One attempt by Stine et al. [Sti20] was to integrate a DO-sensor in a 60 mm Lagrangian Sensor Particle (LSP), exhibiting the possibility for replacing the pressure sensor of the LSP_{60} from this thesis for a DO sensor. A cooperation with the project A08 of the SFB1615 by Trieu should be considered, as Lagrangian devices are also investigated in this project. For the LSP_{60} the integration of an IMU should be implemented to evaluate the acceleration.

To achieve an increased flow-following behavior and avoid tilting movement of the LSPs, the weight distribution around the centered axis and on the lower shell should be optimized.

Furthermore, an increased data set is needed to especially validate the values measured of the top compartment. For that reason, at least three LSPs of one size should be tested simultaneously within the reactor to achieve an overall reliable data basis with a total increased recording time.

Moreover, an aerated reactor with the RT and PB setup should be tested. This might be interesting, as the introduction of air bubbles could potentially enhance overall mixing, whereas at the same time, distorting the LSPs flow-following capability.

A fed batch is more representative for a bio process since the substrates are added sequentially. For further investigations, a fed batch with variable placed inlets streams at different heights should be investigated.

Bibliography

[Ali15] Ali, U., Karim, Khairil Juhanni Bt. Abd and Buang, N.A. *A Review of the Properties and Applications of Poly (Methyl Methacrylate) (PMMA). Polymer Reviews*, 55(4):678–705, 2015. ISSN 1558-3724. doi:10.1080/15583724.2015.1031377.

[Aza21] Azarpira, M., Zarrati, A. and Farrokhzad, P. *Comparison between the Lagrangian and Eulerian Approach in Simulation of Free Surface Air-Core Vortices. Water*, 13(5):726, ISSN 2021. doi:10.3390/w13050726.

[Baj82] Bajpai, R.K. and Reuss, M. *Coupling of mixing and microbial kinetics for evaluating the performance of bioreactors. The Canadian Journal of Chemical Engineering*, 60(3):384–392, 1982. ISSN 0008-4034. doi:10.1002/cjce.5450600308.

[Bis21] Bisgaard, J., Muldbak, M., Tajsoleiman, T., Rydal, T., Rasmussen, T., Huusom, J.K. and Gernaey, K.V. *Characterization of mixing performance in bioreactors using flow-following sensor devices. Chemical Engineering Research and Design*(174):471–485, 2021. ISSN 0263-8762. doi:10.1016/j.cherd.2021.08.008.

[Bis22] Bisgaard, J., Zahn, J.A., Tajsoleiman, T., Rasmussen, T., Huusom, J.K. and Gernaey, K.V. *Data-based dynamic compartment model: Modeling of E. coli fed-batch fermentation in a 600 m3 bubble column. Journal of industrial microbiology & biotechnology*, 49(5), ISSN 2022. doi:10.1093/jimb/kuac021.

[Bun23] Buntkiel, L., Ma, Y., Reinecke, S.F. and Hampel, U. *Orientation resolved measurements of accelerations with sensor particles in bioreactors.* *tm - Technisches Messen*, 90(12):835–845, 2023. ISSN 2196-7113. doi:10.1515/teme-2023-0115.

[Cor12] Corell, H. *Applications of ocean transport modelling.* Department of Meteorology, Stockholm University, Stockholm, 2012. ISBN 9789174474961.

[Cos11] Cossar, D. *1.51 - Bioprocessing Techniques.* In M. Moo-Young and M. Butler, editors, *Comprehensive Biotechnology (Second Edition)*, pp. 679–690. Elsevier Science, Burlington, 2011. ISBN 978-0-08-088504-9. doi:10.1016/B978-0-08-088504-9.00078-7.

[Cro98] Crowe, C.T., Sommerfeld, M. and Tsuji, Y. *Multiphase flows with droplets and particles.* CRC Press, Boca Raton, Fla., 1998. ISBN 9780849394690.

[Cur11] Curley, S.M., Nicoletti, S.E. and Sharfstein, S.T. *3.58 - Applications of Nanotechnology to Bioprocessing.* In M. Moo-Young, editor, *Comprehensive biotechnology*, pp. 712–730. Pergamon, Oxford, 2011. ISBN 978-0-444-64047-5. doi:10.1016/B978-0-444-64046-8.00193-2.

[Dec05] Decker, S. *Zur Berechnung von gerührten Suspensionen mit dem Euler-Lagrange-Verfahren.* Ph.D. thesis, Universitäts- und Landesbibliothek Sachsen-Anhalt, 2005. doi:10.25673/3689.

[Dig23] Digi-Key Electronics. *89BSD-006BA-A | Digi-Key Electronics | https://www.digikey.at/de/products/detail/te-connectivity-measurement-specialties/89BSD-006BA-A/5277619*, 09.12.2023.

[dJ11] de Jesus, M. and Wurm, F.M. *3.31 - Manufacturing Recombinant Proteins in kg-ton Quantities Using Animal Cells in*

Bioreactors. In M. Moo-Young and M. Butler, editors, *Comprehensive Biotechnology (Second Edition)*, pp. 357–362. Elsevier Science, Burlington, 2011. ISBN 978-0-08-088504-9. doi:10.1016/B978-0-08-088504-9.00544-4.

[Dor13] Doran, P.M. *Chapter 8 - Mixing*. In P.M. Doran, editor, *Bioprocess Engineering Principles (Second Edition)*, pp. 255–332. Academic Press, London, 2013. ISBN 978-0-12-220851-5. doi:10.1016/B978-0-12-220851-5.00008-3.

[Eur24] Euromixers. *Impeller Types:Selecting the right impeller for a mixing or storage tank application is vital to achieve optimum performance, mixing impellers come in a veriety types. (29.04.2019)*, https://www.euromixers.co.-uk/impeller-types/(12.01.2024).

[FDA24] FDA. *Approvals of FDA-Regulated Products (12.06.2018). FDA*, ISSN https://www.fda.gov/news-events/approvals-fda-regulated-products(12.01.2024).

[Fit19] Fitschen, J., Maly, M., Rosseburg, A., Wutz, J., Wucherpfennig, T. and Schlüter, M. *Influence of Spacing of Multiple Impellers on Power Input in an Industrial–Scale Aerated Stirred Tank Reactor. Chemie Ingenieur Technik*, 91(12):1794–1801, 2019. ISSN 0009-286X. doi:10.1002/cite.201900121.

[Fit21] Fitschen, J., Hofmann, S., Wutz, J., Kameke, A., Hoffmann, M., Wucherpfennig, T. and Schlüter, M. *Novel evaluation method to determine the local mixing time distribution in stirred tank reactors. Chemical Engineering Science: X*(10):100098, 2021. ISSN 2590-1400. doi:10.1016/j.cesx.2021.100098.

[Fri98] Frischmuth, U. *Das erweiterte Kalman-Filter zur Unterdrückung harmonischer Störsignale in der Seismik*. ISBN 1998.

[Gou99] Gouesbet, G. and Berlemont, A. *Eulerian and Lagrangian approaches for predicting the behaviour of discrete particles in turbulent flows. Progress in Energy and Combustion Science*, 25(2):133–159, 1999. ISSN 0360-1285. doi:10.1016/S0360-1285(98)00018-5.

[Gre08a] Green, D.W., editor. *Perry's chemical engineers' handbook.* McGraw-Hill, New York [etc.], 8th ed. edn., op. 2008. ISBN 0071422943.

[Gre08b] Gregory T. Benz. *Piloting bioreactors for agitation scale-up.* ISBN 2008.

[Gre11] Gregory T. Benz. *Bioreactor design for chemical engineers.* ISBN 2011.

[Guh06] Guha, D., Dudukovic, M.P., Ramachandran, P.A., Mehta, S. and Alvare, J. *CFD–based compartmental modeling of single phase stirred–tank reactors. AIChE Journal*, 52(5):1836–1846, 2006. ISSN 1547-5905. doi:10.1002/aic.10772.

[Hai89] Haider, A. and Levenspiel, O. *Drag coefficient and terminal velocity of spherical and nonspherical particles. Powder Technology*, 58(1):63–70, 1989. ISSN 0032-5910. doi:10.1016/0032-5910(89)80008-7.

[Har17] Haringa, C., Deshmukh, A.T., Mudde, R.F. and Noorman, H.J. *Euler-Lagrange analysis towards representative down-scaling of a 22 m 3 aerobic S. cerevisiae fermentation. Chemical Engineering Science*(170):653–669, 2017. ISSN 00092509. doi:10.1016/j.ces.2017.01.014.

[Har18] Haringa, C., Mudde, R.F. and Noorman, H.J. *From industrial fermentor to CFD-guided downscaling: what have we learned? Biochemical Engineering Journal*(140):57–71, 2018. ISSN 1369-703X. doi:10.1016/j.bej.2018.09.001.

[Hof22] Hofmann, S., Weiland, C., Fitschen, J., von Kameke, A., Hoffmann, M. and Schlüter, M. *Lagrangian sensors in a stirred tank reactor: Comparing trajectories from 4D-Particle Tracking Velocimetry and Lattice-Boltzmann simulations. Chemical Engineering Journal*(449):137549, 2022. ISSN 1385-8947. doi:10.1016/j.cej.2022.137549.

[Hof24] Hofmann, S. and Buntkiel, L. *Experimental Analysis of Lifelines in a 15,000 L Bioreactor by Means of Lagrangian Sensor Particles*, ISSN 2024.

[Hol64] Holmes, D.B., Voncken, R.M. and Dekker, J.A. *Fluid flow in turbine-stirred, baffled tanks—I. Chemical Engineering Science*, 19(3):201–208, 1964. ISSN 00092509. doi:10.1016/0009-2509(64)85030-2.

[Hui21] Huilier, D.G.F. *An Overview of the Lagrangian Dispersion Modeling of Heavy Particles in Homogeneous Isotropic Turbulence and Considerations on Related LES Simulations. Fluids*, 6(4):145, 2021. ISSN 2311-5521. doi:10.3390/fluids6040145.

[Kai18] Kaiser, S.C., Werner, S., Jossen, V., Blaschczok, K. and Eibl, D. *Power Input Measurements in Stirred Bioreactors at Laboratory Scale. Journal of Visualized Experiments : JoVE*, (135), ISSN 2018. doi:10.3791/56078.

[Kam22] Kamp, Maximilian. *Experimental Investigation of the Flow Behavior of Lagrangian LED Particles in a 200 L Bioreactor*. Bachelor theseís, Technical University Hamburg-Harburg, Hamburg, 29.04.2022.

[Kar07] Karthik P. Jayapal, Katie F Wlaschin, Wei Hu and M. Yap. *Recombinant protein therapeutics from CHO cells : 20 years and counting. Chemical Engineering Progress*, ISSN 2007.

[Kha76] Khang, S.J. and Levenspiel, O. *New scale-up and design method for stirrer agitated batch mixing vessels. Chemical Engineering Science*, 31(7):569–577, 1976. ISSN 00092509. doi:10.1016/0009-2509(76)80020-6.

[Kra04] Kraume, M. *Partikelbewegung.* In *Transportvorgänge in der Verfahrenstechnik*, pp. 333–361. Springer, Berlin, Heidelberg, ISBN 2004. doi:10.1007/978-3-642-18936-4_11.

[Kra18] Kraume, M. *Misch- und Rührtechnik in chemischen Reaktoren.* In *Handbuch Chemische Reaktoren*, pp. 1–46. Springer Spektrum, Berlin, Heidelberg, ISBN 2018. doi:10.1007/978-3-662-56444-8_18-1.

[Leu08] Leung, P.S. and Gershwin, M.E. *6 - NATIVE AUTOANTIGENS VERSUS RECOMBINANT AUTOANTIGENS.* In Y. Shoenfeld, M.E. Gershwin and P.L. Meroni, editors, *Autoantibodies*, pp. 37–45. Elsevier, Amsterdam, 2008. ISBN 978-0-444-52763-9. doi:10.1016/B978-044452763-9/50010-X.

[Lid02] Lidén, G. *Understanding the bioreactor. Bioprocess and Biosystems Engineering*, 24(5):273–279, 2002. ISSN 1615-7605. doi:10.1007/s004490100263.

[Lim10] Lim, Y., Wong, N.S.C., Lee, Y.Y., Ku, S.C.Y., Wong, D.C.F. and Yap, M.G.S. *Engineering mammalian cells in bioprocessing - current achievements and future perspectives. Biotechnology and Applied Biochemistry*, 55(4):175–189, 2010. ISSN 1470-8744. doi:10.1042/BA20090363.

[Lin22] Lin, S., Liu, J., Xia, H., Zhang, Z. and Ao, X. *A numerical study of particle-laden flow around an obstacle: flow evolution and Stokes number effects. Applied Mathematical Modelling*(103):287–307, 2022. ISSN 0307-904X. doi:10.1016/j.apm.2021.10.022.

[Lud23] Ludwig Meister. *Dichtungstechnik und Dichtungen - Ludwig Meister*, https://www.ludwigmeister.de/technische-informationen/dichtungstechnik(21.05.2023).

[Mak15] Makandar, A. and Halalli, B. *Image Enhancement Techniques using Highpass and Lowpass Filters. International Journal of Computer Applications*, 109(14):21–27, 2015. ISSN 0975-8887. doi:10.5120/19256-0999.

[Man16] Mandenius, C.F. *Bioreactors.* Wiley, ISBN 2016. doi: 10.1002/9783527683369.

[Mao17] Mao, Z. and Yang, C. *Micro-mixing in chemical reactors: A perspective. Chinese Journal of Chemical Engineering*, 25(4):381–390, 2017. ISSN 1004-9541. doi:10.1016/j.cjche.2016.09.012.

[Mit23] Mittermeier, F., Bäumler, M., Arulrajah, P., García Lima, J.d.J., Hauke, S., Stock, A. and Weuster-Botz, D. *Artificial microbial consortia for bioproduction processes. Engineering in Life Sciences*, 23(1):e2100152, 2023. ISSN 1618-2863. doi:10.1002/elsc.202100152.

[MY11] Moo-Young, M., editor. *Comprehensive biotechnology.* Pergamon, Oxford, 2011. ISBN 978-0-444-64047-5.

[Nie97] Nienow, A.W. *On impeller circulation and mixing effectiveness in the turbulent flow regime. Chemical Engineering Science*, 52(15):2557–2565, 1997. ISSN 00092509. doi: 10.1016/S0009-2509(97)00072-9.

[Nie98] Nienow, A.W. *Hydrodynamics of Stirred Bioreactors. Applied Mechanics Reviews*, 51(1):3–32, 1998. ISSN 0003-6900. doi:10.1115/1.3098990.

[Nie04] Nienow, A.W. *Aeration in Biotechnology.* In R.E. Kirk and D.F. Othmer, editors, *Encyclopedia of chemical technology*, pp. 1–23. Wiley, New York and Chich-

ester, 2004. ISBN 9780471484943. doi:10.1002/0471238961.0209152014090514.a01.pub3.

[Nie21] Nienow, A.W. *The Impact of Fluid Dynamic Stress in Stirred Bioreactors – The Scale of the Biological Entity: A Personal View. Chemie Ingenieur Technik*, 93(1-2):17–30, 2021. ISSN 0009-286X. doi:10.1002/cite.202000176.

[Oer15] Oertel jr., H., Bohle, M. and Reviol, T. *Strömungsmechanik: Für Ingenieure und Naturwissenschaftler*. SpringerLink Bücher. Springer Fachmedien Wiesbaden and Imprint and Springer Vieweg, Wiesbaden, 7., überarb. aufl. 2015 edn., 2015. ISBN 3658077867. doi:10.1007/978-3-658-07786-0.

[Old14] Oldshue, J.Y. *Chapter 7 - Agitation*. In C.M. Todaro and H.C. Vogel, editors, *Fermentation and Biochemical Engineering Handbook/by Celeste M. Todaro (Editor), Henry C. Vogel (Editor)*, pp. 109–133. William Andrew Publishing, William Andrew/c2014., 2014. ISBN 978-1-4557-2553-3. doi:10.1016/B978-1-4557-2553-3.00007-6.

[Oma10] Omasa, T., Onitsuka, M. and Kim, W.D. *Cell engineering and cultivation of chinese hamster ovary (CHO) cells. Current pharmaceutical biotechnology*, 11(3):233–240, ISSN 2010. doi:10.2174/138920110791111960.

[Oos85] Oosterhuis, N.M., Kossen, N.W., Olivier, A.P. and Schenk, E.S. *Scale-down and optimization studies of the gluconic acid fermentation by Gluconobacter oxydans. Biotechnology and Bioengineering*, 27(5):711–720, 1985. ISSN 1097-0290. doi:10.1002/bit.260270521.

[Rad16] Rader, D.J. and Geller, A.S. *Chapter 2 - Transport and Deposition of Aerosol Particles*. In R. Kohli and K.L. Mittal, editors, *Developments in surface contamination and cleaning series*, pp. 23–90. William Andrews, Amsterdam

and Boston and Heidelberg, 2016. ISBN 978-0-323-29960-2. doi:10.1016/B978-0-323-29960-2.00002-2.

[Rak21] Rakhsha, M., Kees, C.E. and Negrut, D. *Lagrangian vs. Eulerian: An Analysis of Two Solution Methods for Free-Surface Flows and Fluid Solid Interaction Problems. Fluids*, 6(12):460, 2021. ISSN 2311-5521. doi:10.3390/fluids6120460.

[Rau23] Rautenbach, Ryan M. *Experimental Investigations of the Flow-Following Capabilities and Hydrodynamic Characteristics of Lagrangian Sensor Particles with Respect to their Centre of Mass.* Master thesis, Technical University Hamburg-Harburg, Hamburg, 01.02.2023.

[Rei12] Reinecke, S., Deutschmann, A., Jobst, K., Kryk, H., Friedrich, E. and Hampel, U. *Flow following sensor particles—Validation and macro-mixing analysis in a stirred fermentation vessel with a highly viscous substrate. Biochemical Engineering Journal*(69):159–171, 2012. ISSN 1369-703X. doi:10.1016/j.bej.2012.09.010.

[Rei14] Reinecke, S.F. *Instrumentierte Strömungsfolger zur Prozessdiagnose in gerührten Fermentern: Zugl.: Dresden, Techn. Univ., Fak. Elektrotechnik und Informationstechnik, Diss., 2013*, vol. Bd. 52 of *Dresdner Beiträge zur Sensorik*. TUDpress, Dresden, 2014. ISBN 9783944331508.

[Ros18] Rosseburg, A., Fitschen, J., Wutz, J., Wucherpfennig, T. and Schlüter, M. *Hydrodynamic inhomogeneities in large scale stirred tanks – Influence on mixing time. Chemical Engineering Science*(188):208–220, 2018. ISSN 00092509. doi:10.1016/j.ces.2018.05.008.

[Sai14] Saidi, M.S., Rismanian, M., Monjezi, M., Zendehbad, M. and Fatehiboroujeni, S. *Comparison between Lagrangian and Eulerian approaches in predicting motion*

of micron-sized particles in laminar flows. Atmospheric Environment(89):199–206, 2014. ISSN 1352-2310. doi: 10.1016/j.atmosenv.2014.01.069.

[San16] Sanford, K., Chotani, G., Danielson, N. and Zahn, J.A. *Scaling up of renewable chemicals. Current Opinion in Biotechnology*(38):112–122, 2016. ISSN 0958-1669. doi: 10.1016/j.copbio.2016.01.008.

[Sch18] Schönfelder, G. and Hering, E., editors. *Sensoren in Wissenschaft und Technik: Funktionsweise und Einsatzgebiete: Funktionsweise und Einsatzgebiete*. Springer Vieweg, Wiesbaden, 2., überarbeitete und aktualisierte auflage edn., 2018. ISBN 3658125616.

[Sch19] Schwedhelm, I.P. *A non-invasive microscopy platform for the online monitoring of hiPSC aggregation in suspension cultures in small-scale stirred tank bioreactors: Doctoralthesis*. Ph.D. thesis, Universität Würzburg, 2019. doi: 10.25972/OPUS-19298.

[Sha03] Shaw, R.A. *Particle-Turbulence Interaction in Atmospheric Clouds. Annual Review of Fluid Mechanics*, 35(1):183–227, 2003. ISSN 0066-4189. doi:10.1146/annurev.fluid.35.101101.161125.

[Spu19] Spurk, J. and Aksel, N. *Strömungslehre: Einführung in die Theorie der Strömungen*. SpringerLink Bücher. Springer Berlin Heidelberg and Springer Vieweg, Berlin, Heidelberg, 9., aktual. aufl. 2019 edn., 2019. ISBN 3662587645. doi: 10.1007/978-3-662-58764-5.

[Sre15] Sreenivasan, K.R. and Oertel, H. *Instabilitäten und turbulente Strömungen*. In *Prandtl - Führer durch die Strömungslehre*, pp. 1–73. Springer Vieweg, Wiesbaden, ISBN 2015. doi:10.1007/978-3-658-08933-7{\textunderscore}7-1.

[Sti09] Stieß, M. *Fluidmechanische Grundlagen.* In *Mechanische Verfahrenstechnik - Partikeltechnologie 1*, pp. 105–160. Springer, Berlin, Heidelberg, ISBN 2009. doi: 10.1007/978-3-540-32552-9{\textunderscore}4.

[Sti20] Stine, J.M., Beardslee, L.A., Sathyam, R.M., Bentley, W.E. and Ghodssi, R. *Electrochemical Dissolved Oxygen Sensor-Integrated Platform for Wireless In Situ Bioprocess Monitoring. Sensors and Actuators B: Chemical*(320):128381, 2020. ISSN 0925-4005. doi:10.1016/j.snb.2020.128381.

[Sub23] Subramaniam, S. and Balachandar, S., editors. *Modeling approaches and computational methods for particle-laden turbulent flows.* Computation and analysis of turbulent flows. Academic Press, London, 2023. ISBN 978-0-323-90133-8.

[Tom23] Tom Hess. *Acrylglas tempern » Warum & wie macht man das? (2015)*, https://www.hausjournal.net/acrylglas-tempern(22.07.2023).

[van87] van Barneveld, J., Smit, W., Oosterhuis, N.M.G. and Pragt, H.J. *Measuring the liquid circulation time in a large gas-liquid contractor by means of a radio pill. Part 2. Circulation time distribution. Industrial & Engineering Chemistry Research*, 26(11):2192–2195, 1987. ISSN 0888-5885. doi: 10.1021/ie00071a004.

[Vrá00] Vrábel, P., van der Lans, R.G., Luyben, K.C., Boon, L. and Nienow, A.W. *Mixing in large-scale vessels stirred with multiple radial or radial and axial up-pumping impellers: modelling and measurements. Chemical Engineering Science*, 55(23):5881–5896, 2000. ISSN 00092509. doi: 10.1016/S0009-2509(00)00175-5.

[War85] Warmoeskerken, M. and Smith, J.M. *Flooding of disc turbines in gas-liquid dispersions: A new description of the*

phenomenon. Chemical Engineering Science, 40(11):2063–2071, 1985. ISSN 00092509. doi:10.1016/0009-2509(85)87023-8.

[Weh19] Wehrs, M., Gladden, J.M., Liu, Y., Platz, L., Prahl, J.P., Moon, J., Papa, G., Sundstrom, E., Geiselman, G.M., Tanjore, D., Keasling, J.D., Pray, T.R., Simmons, B.A. and Mukhopadhyay, A. *Sustainable bioproduction of the blue pigment indigoidine: Expanding the range of heterologous products in R. toruloides to include non-ribosomal peptides. Green Chemistry*, 21(12):3394–3406, 2019. ISSN 1463-9270. doi:10.1039/C9GC00920E.

[Wit19] Wittmann, F., Lambercy, O. and Gassert, R. *Magnetometer-Based Drift Correction During Rest inIMU Arm Motion Tracking. Sensors*, 19(6):1312, 2019. ISSN 1424-8220. doi:10.3390/s19061312.

[Wol10] Wollny, S. *Experimentelle und numerische Untersuchungen zur Partikelbeanspruchung in gerührten (Bio-)Reaktoren*, 2010. doi:10.14279/depositonce-2528.

[Yan99] Yang, W.C., editor. *Fluidization, solids handling, and processing: Industrial applications.* Particle technology series. Noyes Publ, Westwood, NJ, 1999. ISBN 978-0-8155-1427-5.

A Results

A.1 Probability of Presence

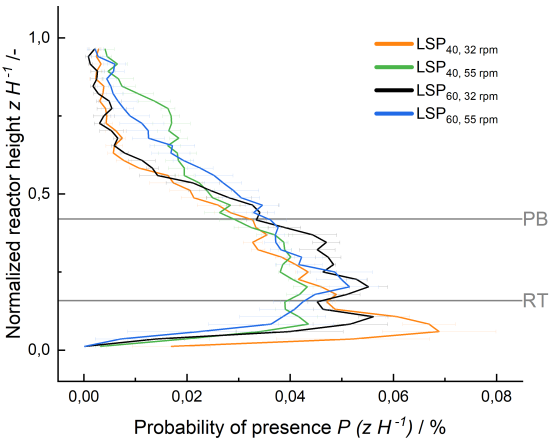

Figure A.1: Axial probability of presence of LSP_{40} and LSP_{60} over the normalized reactor height ($H = 4.2$ m) with a vertical bin size of 0.1 m calculated for each impeller frequency (32 rpm, 55 rpm), including the respective uncertainties. The horizontal lines represent the center of the RT and PB, respectively.

A.2 Velocity

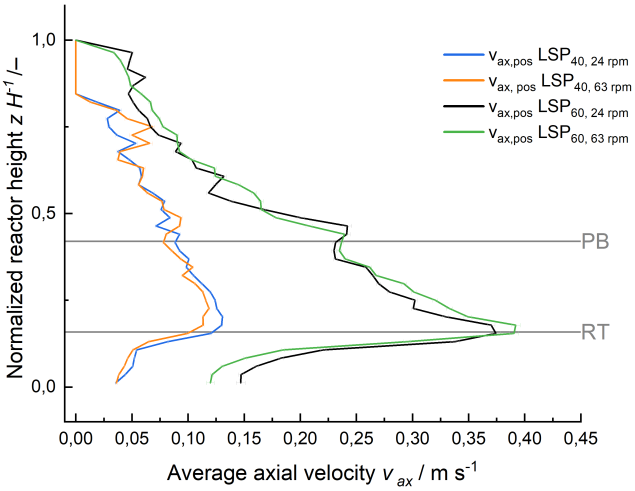

Figure A.2: Average axial velocities of LSP_{40} and LSP_{60} over the normalized reactor height (H= 4.2 m) with a vertical bin size of 0.1 m is calculated for the impeller frequency (24 rpm, 63 rpm), including the respective uncertainties. The horizontal lines represent the center of the RT and PB, respectively.

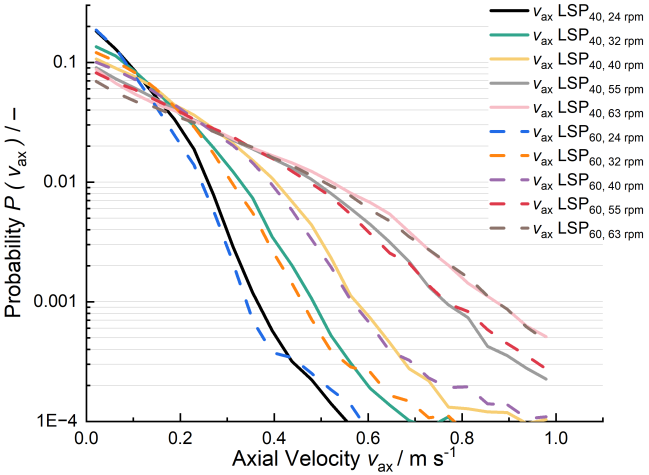

Figure A.3: Probability of the overall negative axial velocities $|v_{\mathrm{ax,neg}}|$ of the LSP_{40} and LSP_{60} calculated for each impeller frequency (24 rpm, 32 rpm, 40 rpm, 55 rpm, 63 rpm), using a class width of 0.04 s.

A.3 Average Circulation Time

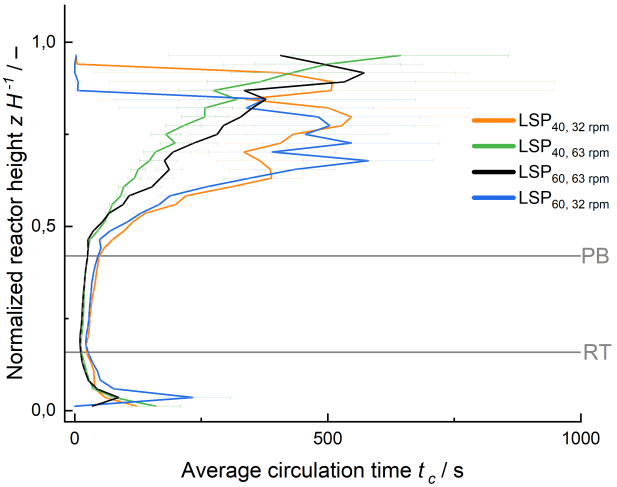

Figure A.4: Average circulation times $\bar{t}_c$ of LSP_{40} and LSP_{60} over the normalized reactor height ($H = 4.2$ m) with a vertical bin size of 0.1 m calculated for each impeller frequency (32 rpm, 63 rpm), including the respective uncertainties. The horizontal lines represent the center of the RT and PB, respectively.